Consistent, Essentially Conservative and Balanced-Force Phase-Field Method to Model Incompressible Two-Phase Flows

Ziyang Huang[1], Guang Lin[1,2], and Arezoo M. Ardekani[1]

[1] School of Mechanical Engineering, Purdue University, West Lafayette, IN 47907, USA
[2] Department of Mathematics, Purdue University, West Lafayette, IN 47907, USA
huan1020@purdue.edu, guanglin@purdue.edu, ardekani@purdue.edu

Abstract. In the present work, the Cahn-Hilliard Phase-Field model of incompressible two-phase flows is considered. Conditions needed for *consistency of reduction*, *consistency of mass and momentum transport*, and *consistency of mass conservation* are proposed. The mass flux in the Navier-Stokes equations is defined such that it satisfies the proposed consistency conditions. The analysis in both continuous and discrete levels shows that violation of the consistency conditions result in unphysical solutions and the inconsistent errors are proportional to the density contrast of the fluids. After considering the conservative form of the inertial term, a consistent and conservative scheme for momentum transport is developed. The balanced-force algorithm for the sharp interface model is extended to the surface force derived from the Cahn-Hilliard model. The proposed scheme is formally 2nd-order accurate in both time and space, satisfies the consistency conditions, conserves mass globally and momentum essentially, and is balanced-force, in the discrete level. Its convergence to the sharp interface solution is systematically discussed in cases including large density and viscosity ratios, surface tension, and gravity. Various two-phase flow problems with large density ratios are performed to validate and verify the proposed scheme and excellent agreements with published numerical and/or experimental results are achieved. The proposed scheme is a practical and accurate tool to study two-phase flows, especially for those including large density ratios.

Keywords: Consistent scheme · Essentially conservative scheme · Balanced-Force scheme · Phase-Field · Two-phase flow · Large density ratio.

1 Introduction

Two-phase flow problems are ubiquitous, and have attracted much attention because of their complicated physical nature and wide-spread applications. In most scenarios of interest, the interface thickness is so small that the sharp interface model [36] is accurate, where the fluid motion inside the individual phase is governed by the Navier-Stokes equations and different phases are connected

by the boundary conditions at the interfaces. However, in numerical practice, explicitly imposing the boundary conditions at the interfaces, whose locations are unknown, is not a trivial task. The so-called "one-fluid formulation" [64,50] has gained great attention, where a single set of transport equations with variable density and viscosity is solved in the entire domain. The boundary conditions at the interfaces are implicitly imposed by using, e.g., the continuous surface force (CSF) [9] or the ghost fluid method (GFM) [23,35]. The location of the interface is tracked by using the Front-Tracking method [65], Level-Set [48,62], Conservative Level-Set [46,47,13], Volume-of-Fluid (VOF) [26,57] or the "THINC" method [67]. To overcome the numerical difficulty of approximating a discontinuous function, the interface has to be explicitly reconstructed, which can be very complicated, or artificial smoothing has to be performed close to the interface.

The Phase-Field model, or known as the diffuse interface model [4], is another widely used method for two-phase flow modeling, where the thickness of the interface is small but finite. This thickness is maintained by the intrinsic thermodynamical compression and diffusion of the Phase-Field model. Among different Phase-Field models, the Cahn-Hilliard Phase-Field model [11], which is the focus of the present study, is getting more popular for two-phase flow problems. The Cahn-Hilliard Phase-Field model has several advantages. It is globally mass conservative and is able to handle topological change without additional effort. It doesn't require any explicit interface reconstruction. The surface force calculation of the Phase-Field model doesn't require evaluation of geometrical quantities, e.g., the normal vector or curvature of the interface. In addition, it is very easy to include multiple physical effects by modifying its energy functional.

The Cahn-Hilliard model together with the Navier-Stokes equations was first used to model the matched density problems and this model is also called the Model H [27]. The numerical scheme for the Model H was developed by several researchers [30,5], and its asymptotic and convergence behavior was systematically analyzed and numerically validated by Jacqmin [30] and more recently by Magaletti et al. [42]. To model problems with small density ratios, the Boussinesq approximation can be used, e.g., [68]. For large-density-ratio problems, the so-called modified Model H is commonly used, where the constant density in the Navier-Stokes equations is replaced by the variable one. Kim [34] used the modified Model H and considered the rising bubble case with the density ratio of 1000, and Ding et al. [17] further discussed its capability of dealing with large density ratios. However, all the large-density-ratio comparisons in both of these studies are qualitative. A time-stepping scheme was developed by Dong and Shen [22] to improve the efficiency of solving the modified Model H for large-density-ratio problems. The quantitative comparisons of the Phase-Field solution to the sharp interface solution was provided in [22] and good agreement was obtained. Both the Model H and the modified Model H have been widely used to study various multiphase problems, e.g., jet pinching-off and drop formation [68], two-phase complex fluids [70], two-phase Newtonian and viscoelastic fluids [71], Nematic Liquid Crystals [78], two-phase ferrofluid flows [45], and moving contact lines

[31,51,76,60]. However, it has been noticed that the modified Model H is unable to recover the energy law. Multiple models and their corresponding numerical schemes have been developed to remedy this problem. One way to do that, proposed by Guermond and Quartapelle [25], is to replace the time derivative in the momentum conservation equation by an equivalent term derived from the mass conservation equation [25,58]. Liu et al. [41] included the kinetic energy of the fluids into the energy functional of the Phase-Field model and developed a decoupled energy stable schemes to solve the model derived from the new energy functional. Another model is developed by Abels et al. [1], where an additional convection term is included in the momentum conservation equation. Shen and Yang [59] developed a decoupled energy stable scheme for this model. The models, proposed by Guermond and Quartapelle [25], Liu et al. [41] and Abels et al. [1], guarantee that the total energy of the two-phase system, without external energy source, does not increase with time, which is thermodynamically correct. The model proposed by Abels et al. [1] was extended by Bai et al. [7] to study the deformation and breakup of ferrodroplet, and by Dong [19,20,21] and Yang and Dong [69] to N-phase flows.

In spite of many successful applications of the Model H and the modified Model H and ongoing efforts to improve the Phase-Field model for large-density-ratio problems, some important questions remained unanswered. Consistency and conservation of mass and momentum transport are specially important for large-density-ratio problems that need to be addressed. Consistent and conservative schemes have been developed by Rudman [55], Bussmann et al. [10], Chenadec and Pitsch [12], and Owkes and Desjardins [49] for the Volume-of-Fluid method, and by Raessi and Ritsch [52] for the Level-Set method. On the other hand, almost all numerical schemes for the Phase-Field model are based on the non-conservative form of the inertial term and are not discretely conservative. The significance of the consistency of mass and momentum transport has not yet been addressed for the Phase-Field model and none of the existing numerical schemes achieve consistency in the discrete level. In the present work, we perform both continuous and discrete analyses to show that the *consistency of reduction*, the *consistency of mass and momentum transport* and the *consistency of mass conservation* are of great importance to obtain physical solutions of large-density-ratio problems. The detailed definition of the *consistency* is given in the following section. Our numerical implementations validate our analysis. Following our analysis of consistency and considering the conservative form of the inertial term, the scheme we develop guarantees the consistency and conservation of momentum transport in the discrete level. Another important question is whether the numerical solution of the Phase-Field model converges to the sharp interface solution and how fast it converges, but this is rarely discussed for large-density-ratio problems. Except the work of [1], there is no asymptotic analysis showing that the exact solution of the Phase-Field models converges to the sharp interface solution in large-density-ratio problems, as the interface thickness decreases. Since the actual thickness of interface is so small that it is computationally unaffordable to resolve it, the interface thickness is nonphysi-

cally exaggerated almost in all numerical studies. Because of that, the asymptotic error of the Phase-Field model could be large, even if the model is asymptotically converging. Thus, it is not enough to tell whether the Phase-Field model, in numerical practice, is accurately approximating the sharp interface one by only proving its asymptotic convergence in the continuous level. It is also important to understand the convergence behavior of the numerical solution of the Phase-Field model to the sharp interface solution when both truncation error and asymptotic error appear. Quantitative numerical evidence of convergence of this kind is rarely provided in the literature, except in the works of Aland and Voigt [2] and of Huang et al. [28]. However, the numerical schemes in [2,28] are not consistent or conservative. Both of them only considered the case, where the interface thickness reduces as fast as the grid size, so it is difficult to conclude whether this is an optimal setup. We further extend the work of Aland and Voigt [2] by using the proposed consistent, essentially conservative, and balanced-force scheme, by considering different correlations between the interface thickness and the grid size, and by exploring the effect of the mobility of the Phase-Field model.

The outlines of this article is as follows. In Section 2, we summarize the governing equations, propose three consistency conditions, discuss the effect of the consistency conditions, and analyze how to achieve consistency in both continuous and discrete levels. In Section 3, detailed spatial and temporal discretization of the governing equations are described, followed by discussions about their accuracy, consistency, conservation and energy dissipation of the scheme. In Section 4, multiple cases are performed to validate and verify the proposed scheme. In Section 5, we conclude the present work by summarizing the property of the scheme and the numerical results, and by discussing the potential implementations of our analysis and scheme, and the future works.

2 Governing equations and analysis of consistency

The Phase-Field model for the incompressible two-phase flow, consisting of the Cahn-Hilliard equations and the Navier-Stokes equations, are considered. The coupling between the Cahn-Hilliard equations and the Navier-Stokes equations are through the constitutive equations for material properties and through the consistent mass flux. Three consistency conditions are proposed, which are important for a two-phase model to achieve physical results.

Cahn-Hilliard equations are given as

$$\frac{\partial \phi}{\partial t} + \nabla \cdot (\mathbf{u}\phi) = \nabla \cdot (M \nabla \xi) + S_\phi, \tag{1}$$

$$\xi = \lambda (F'(\phi) - \nabla^2 \phi), \tag{2}$$

$$F(\phi) = \frac{1}{4\eta^2}(1-\phi)^2(1+\phi)^2, \tag{3}$$

$$\lambda = \frac{3}{2\sqrt{2}}\sigma\eta, \tag{4}$$

where ϕ is the Phase-Field function ranging from -1 to 1, $\mathbf{u}$ is the velocity, M is the mobility, ξ is the chemical potential, S_ϕ is the Phase-Field source term, λ is the mixing energy density, $F(\phi)$ is the potential function in the bulk phase, η is the interface thickness in the Phase-Field model, and σ is the surface tension between the two fluids. Eq.(1) is the Phase-Field equation described by the Cahn-Hilliard dynamics. At the location where ϕ is equal to 1, it is occupied by Fluid 1 whose density and viscosity are ρ_1 and μ_1, respectively, and when ϕ is equal to -1, it represents Fluid 2 with density ρ_2 and viscosity μ_2. Eq.(2) defines the analytical chemical potential ξ. $F(\phi)$ in Eq.(3) is a double-well potential function which separates different phases, and $F'(\phi)$ in Eq.(2) is the derivative of $F(\phi)$ with respect to ϕ. Eq.(4) connects the surface tension σ to the Phase-Field parameters η and λ. Since all the two-phase flow cases we considered in the present work include immiscible fluids and have no phase change, the source term S_ϕ should be identically zero. We will skip this term in the following analysis.

Fluid properties can be calculated as

$$\rho(\phi) = \frac{\rho_1 + \rho_2}{2} + \frac{\rho_1 - \rho_2}{2}\phi, \tag{5}$$

$$\mu(\phi) = \frac{\mu_1 + \mu_2}{2} + \frac{\mu_1 - \mu_2}{2}\phi, \tag{6}$$

where $\rho(\phi)$ and $\mu(\phi)$ are the density and viscosity of the mixture of Fluids 1 and 2.

Navier-Stokes equations are written as

$$\frac{\partial \rho}{\partial t} + \nabla \cdot \mathbf{m} = S_m, \tag{7}$$

$$\nabla \cdot \mathbf{u} = 0, \tag{8}$$

$$\frac{\partial(\rho\mathbf{u})}{\partial t} + \nabla \cdot (\mathbf{m} \otimes \mathbf{u}) = -\nabla p + \nabla \cdot [\mu(\nabla\mathbf{u} + (\nabla\mathbf{u})^T)] + \rho\mathbf{g} + \xi\nabla\phi + \mathbf{S}_\mathbf{u}, \tag{9}$$

where $\mathbf{m}$ is the mass flux, S_m is the mass source, $\otimes$ represents tensor product, p is the pressure, $\mathbf{g}$ is the gravitational acceleration, and $\mathbf{S}_\mathbf{u}$ is the momentum source, or other external force. Eq.(7) represents mass conservation, Eq.(8) states incompressibility or volume conservation, and Eq.(9) is the momentum conservation equation. We have already assumed that both fluids are Newtonian and incompressible. The surface force $\xi\nabla\phi$, which is derived from the Cahn-Hilliard equations, models the surface tension effect at the interface. With appropriate initial and boundary conditions, Eq.(1)-Eq.(9) can be numerically solved.

2.1 Consistency in the continuous level

We are going to consider three consistency conditions for a two-phase flow model. Violation of any of them may lead to unphysical solution even in the continuous level. It should be noted that we have not yet explicitly given the definition of the mass flux $\mathbf{m}$ in Eq.(7) and Eq.(9). We are going to discuss the influence of the definition of the mass flux $\mathbf{m}$ on flow physics, and to determine a consistent mass flux, based on the consistency conditions of the Cahn-Hilliard Phase-Field model in the continuous level.

The consistency conditions are

- *Consistency of reduction*: The two-phase flow model Eq.(9) should be able to recover the single-phase one, i.e., $\mathbf{m} = \rho\mathbf{u}$ and $\nabla \cdot (\mu(\nabla\mathbf{u})^T) = 0$, when either $\rho_1 = \rho_2$ and $\mu_1 = \mu_2$ or $\phi \equiv 1(-1)$.
- *Consistency of mass and momentum transport*: The momentum flux in the momentum conservation equation, Eq.(9), should consistently be computed from the mass flux obtained from the mass conservation equation, Eq.(7).
- *Consistency of mass conservation*: The mass conservation equation, Eq.(7), should be consistent with the mass transport equation defined from the Phase-Field equation, Eq.(1), and Eq.(5). The mass flux $\mathbf{m}$ in the mass conservation equation, Eq.(7), should lead to a zero mass source, i.e., $S_m \equiv 0$.

The *consistency of reduction* guarantees that the single-phase dynamics can be physically reproduced by the two-phase model, when there exits a single phase. This is important for two-phase flow problems because away from the interface, the domain is occupied by only one of the fluids and the dynamics is governed by the single-phase model. It should be noted that either $\rho_1 = \rho_2$ and $\mu_1 = \mu_2$ or $\phi \equiv 1(-1)$ leads to constant density and viscosity.

The *consistency of mass and momentum transport* guarantees the physical coupling between the mass conservation equation Eq.(7) and the momentum conservation equation Eq.(9). The amount of the momentum flux should be correlated to the amount of the mass flux, and this has been guaranteed in the continuous level, by writing the inertia term in the form $\nabla \cdot (\mathbf{m} \otimes \mathbf{u})$.

The *consistency of mass conservation* guarantees that the mass transport $\nabla \cdot \mathbf{m}$ follows the actual mass evolution, implicitly defined by Eq.(1) and Eq.(5). In practice, the mass conservation equation, Eq.(7), is not directly solved. The density is updated from the density equation Eq.(5) after updating the Phase-Field function ϕ from the Phase-Field equation Eq.(1). If we simply define $\mathbf{m} = \rho\mathbf{u}$, Eq.(9) recovers the unmodified Navier-Stokes equations. Although such a definition of $\mathbf{m}$ satisfies the *consistency of reduction* and the *consistency of mass and momentum transport*, it fails to satisfy the *consistency of mass conservation*, and can lead to unphysical results as shown later in this section.

When μ is constant, $\nabla \cdot (\mu(\nabla\mathbf{u})^T)$ is zero by considering the divergence-free condition of the velocity Eq.(8) and the identity

$$\nabla \cdot (\mu(\nabla\mathbf{u})^T) = \mu\nabla(\nabla \cdot \mathbf{u}). \tag{10}$$

The *consistency of reduction* of the viscous term is guaranteed by Eq.(10) in the continuous level. In the remaining of this section, we will focus on defining a consistent mass flux $\mathbf{m}$ and discuss its significance on capturing flow physics.

Hereafter, when we mention the mass conservation equation Eq.(7), we refer to the one that is already consistent with Eq.(1) and Eq.(5), and the mass source S_m in Eq.(7) is uniquely defined after the mass flux $\mathbf{m}$ is specified. We denote the inconsistent mass flux as

$$\mathbf{m}^{IC} \equiv \rho\mathbf{u}, \tag{11}$$

and use $\mathbf{m}^{CC}$ to represent the consistent mass flux in the continuous level.

We first consider the general case of $\mathbf{m}$. We can rewrite the mass conservation equation Eq.(7), the left-hand side of the momentum conservation equation Eq.(9), and the dot product between the left-hand side of Eq.(9) and the velocity $\mathbf{u}$ as

$$S_m = \frac{\partial \rho}{\partial t} + \nabla \cdot \mathbf{m}, \tag{12}$$

$$\frac{\partial(\rho\mathbf{u})}{\partial t} + \nabla \cdot (\mathbf{m} \otimes \mathbf{u}) = \big(\rho\frac{\partial \mathbf{u}}{\partial t} + \mathbf{m} \cdot \nabla\mathbf{u}\big) + \mathbf{u}S_m, \tag{13}$$

$$\begin{aligned}\big[\frac{\partial(\rho\mathbf{u})}{\partial t} + \nabla \cdot (\mathbf{m} \otimes \mathbf{u})\big] \cdot \mathbf{u} &= \big(\rho\frac{\partial}{\partial t}\frac{\mathbf{u}\cdot\mathbf{u}}{2} + \mathbf{m} \cdot \nabla\frac{\mathbf{u}\cdot\mathbf{u}}{2}\big) + \mathbf{u}\cdot\mathbf{u}S_m \\ &= \frac{\partial}{\partial t}\big(\rho\frac{\mathbf{u}\cdot\mathbf{u}}{2}\big) + \nabla\cdot\big(\mathbf{m}\frac{\mathbf{u}\cdot\mathbf{u}}{2}\big) + \frac{\mathbf{u}\cdot\mathbf{u}}{2}S_m.\end{aligned} \tag{14}$$

Eq.(12) shows that the source term in the mass conservation equation depends on the definition of the mass flux, Eq.(13) represents the momentum transport, and Eq.(14) indicates the transport of the kinetic energy. Consider a simple case where all the fluid particles inside the domain of interest are moving with a constant velocity and no body force is present, i.e., the right-hand side of Eq.(9) is zero. The velocity and kinetic energy should remain uniform. When we input a constant velocity into Eq.(13) and Eq.(14), a non-zero mass source term S_m results in non-zero momentum and kinetic energy sources, i.e., $\mathbf{u}S_m$ and $\mathbf{u}\cdot\mathbf{u}S_m$. These sources interfer with the transport of the momentum and kinetic energy, and finally generate unphysical results. Since the left-hand side of Eq.(13) is in the conservative form, the conservation of momentum transport is achievable, although unphysical results may be obtained. However, when we rewrite the kinetic energy transport into a conservative form, a non-conservative term $\frac{\mathbf{u}\cdot\mathbf{u}}{2}S_m$ appears with a non-zero S_m, leading to failure of conservation of kinetic energy even in the continuous level no matter whether the fluids are inviscid or not. If we take $\mathbf{m} = \mathbf{m}^{IC}$, from Eq.(1) and Eq.(5), we can derive the corresponding mass source $S_m^{IC} = \frac{\rho_1-\rho_2}{2}\nabla\cdot(M\nabla\xi)$, which is in general non-zero. In other words, unphysical results can be obtained by choosing the inconsistent mass flux, because of violating the *consistency of mass conservation*.

Based on the analysis above, in order to obtain a physical solution, it is crucial to define a consistent mass flux $\mathbf{m}^{CC}$ that satisfies the *consistency of*

mass conservation, by requiring $S_m^{CC} \equiv 0$. From Eq.(1), Eq.(5) and Eq.(7), we have

$$\nabla \cdot \mathbf{m}^{CC} = -\frac{\partial \rho}{\partial t} = -\frac{\rho_1 - \rho_2}{2}\frac{\partial \phi}{\partial t} = \frac{\rho_1 - \rho_2}{2}[\nabla \cdot (\mathbf{u}\phi) - \nabla \cdot (M\nabla \xi)]. \tag{15}$$

If we directly take $\mathbf{m}^{CC} = \frac{\rho_1 - \rho_2}{2}(\mathbf{u}\phi - M\nabla\xi)$, we failed to satisfy the *consistency of reduction*, such that $\mathbf{m}^{CC}$ is always zero, instead of $\rho\mathbf{u}$, when both fluids have matched densities, i.e., $\rho_1 = \rho_2 = \rho$. To remedy this, a divergence-free term has to be added in order to maintain Eq.(15), and to ensure the *consistency of reduction*. As the velocity is divergence-free Eq.(8), a convenient choice of the added term is $\frac{\rho_1+\rho_2}{2}\mathbf{u}$, as $\nabla \cdot (\frac{\rho_1+\rho_2}{2}\mathbf{u}) = \frac{\rho_1+\rho_2}{2}\nabla \cdot \mathbf{u} = 0$. We can define the consistent mass flux in the continuous level as

$$\mathbf{m}^{CC} = \frac{\rho_1 + \rho_2}{2}\mathbf{u} + \frac{\rho_1 - \rho_2}{2}(\mathbf{u}\phi - M\nabla\xi). \tag{16}$$

When $\phi \equiv 1(-1)$, the chemical potential ξ, from Eq.(2) and Eq.(3), is zero, and $\mathbf{m}^{CC} = \rho\mathbf{u}$, where ρ is $\rho_1(\rho_2)$, from Eq.(16). Finally, Eq(16) satisfies all the consistency conditions, and from the analysis above, we can obtain, by using the consistent mass flux $\mathbf{m}^{CC}$, the physically correct momentum and kinetic energy transport and, simultaneously, their conservation in the continuous level.

We can relate $\mathbf{m}^{CC}$ with $\mathbf{m}^{IC}$ by using Eq.(5), i.e.,

$$\mathbf{m}^{CC} = \mathbf{m}^{IC} - \frac{\rho_1 - \rho_2}{2}M\nabla\xi. \tag{17}$$

It is obvious that, different from $\mathbf{m}^{IC}$, where only the mass transported by the flow is considered, the consistent mass flux $\mathbf{m}^{CC}$ of the Phase-Field model have an additional term representing the mass diffusion between different phases, which is allowable in the Cahn-Hilliard dynamics, and this term becomes more significant when the density contrast of the two fluids increases.

When we input $\mathbf{m}^{CC}$ into Eq.(13), we can obtain

$$\frac{\partial(\rho\mathbf{u})}{\partial t} + \nabla \cdot (\mathbf{m}^{CC} \otimes \mathbf{u}) = \rho\big(\frac{\partial \mathbf{u}}{\partial t} + \mathbf{u} \cdot \nabla\mathbf{u}\big) + \big(-\frac{\rho_1 - \rho_2}{2}M\nabla\xi\big) \cdot \nabla\mathbf{u}. \tag{18}$$

In the modified Model H [34,17,22], the first term on the right-hand side of Eq.(18) is remained while the second term is neglected. This leads to the failure of conserving momentum even in the continuous level. We notice that the right-hand side of Eq.(18) is the same as the model proposed by Abels et al. [1], implying that the Phase-Field model considered in the present work with $\mathbf{m} = \mathbf{m}^{CC}$ should share the following properties of the model in [1]. The total energy of this two-phase Phase-Field model does not increase with time. This Phase-Field model is frame indifferent, and it converges to the sharp interface model as the interface thickness η goes to zero. Some recent progress has included the second term on the right-hand side of Eq.(18) [7,19,20,21,69]. However, those schemes are focusing on the non-conservative form, i.e., using the right-hand side instead of the left-hand side of Eq.(18) when computing the momentum equation, which

does not conserve the momentum transport in the discrete level. Even though the consistency in the continuous level is achieved, it can be violated in the discrete level, which will be discussed in Section 2.2.

Before we move to Section 2.2, we further consider the influence of neglecting the second term on the right-hand side of Eq.(18) on kinetic energy transport

$$\big(\rho\frac{\partial \mathbf{u}}{\partial t}+\mathbf{m}^{IC}\cdot\nabla\mathbf{u}\big)\cdot\mathbf{u}=\frac{\partial}{\partial t}\big(\rho\frac{\mathbf{u}\cdot\mathbf{u}}{2}\big)+\nabla\cdot\big(\mathbf{m}^{IC}\frac{\mathbf{u}\cdot\mathbf{u}}{2}\big)-\frac{\mathbf{u}\cdot\mathbf{u}}{2}S_m^{IC}. \tag{19}$$

Eq.(19) is the same as the right-hand side of Eq.(14) when $\mathbf{m}=\mathbf{m}^{IC}$ and $S_m=S_m^{IC}$ in Eq.(12), except that the sign of the last term is opposite. Neglecting the second term on the right-hand side of Eq.(18) does not conserve kinetic energy in the continuous level.

2.2 Consistency in the discrete level

In this section, implementation of the three consistency conditions, proposed in Section 2.1, in the discrete level will be discussed. We first introduce the notation and the grid arrangement. Any operator with $\sim$ denotes the discrete operator, e.g., $\tilde{\nabla}$ is the discrete gradient operator. Any variable with $\sim$, e.g., $\tilde{f}$, denotes a numerical approximation from nodal values f. We use, e.g., $\tilde{f}^{(1)}$ and $\tilde{f}^{(2)}$ to distinguish different numerical schemes used to obtain $\tilde{f}$ if necessary. At this stage, details of numerical schemes are not important for the following analysis. The definitions of the numerical schemes used in the present work are in Section 3.1. The grid that are considered in the present work is the collocated grid arrangement where the discrete Phase-Field function ϕ, cell-center velocity $\mathbf{u}$, and pressure p are all stored at the center of the computational cells. In addition, the cell-face velocity, which is the velocity component normal to the cell faces, is also computed and saved. The two-dimensional schematic of the collocated grid arrangement is shown in Fig. 1 and its extension to three dimension is straightforward.

We require the cell-face velocity to satisfy the discrete divergence-free condition, i.e.,

$$\tilde{\nabla}\cdot\mathbf{u}=0. \tag{20}$$

Since the discrete divergence-free condition Eq.(20) is held, the *consistency of reduction* of the viscous term requires that Eq (10) is satisfied in the discrete level, when μ is constant, e.g.,

$$[\tilde{\nabla}\cdot(\tilde{\mu}(\tilde{\nabla}\tilde{\mathbf{u}})^T)]_{i,j}=\big\{\mu[\tilde{\partial}^x(\tilde{\nabla}\cdot\mathbf{u})]_{i,j},\mu[\tilde{\partial}^y(\tilde{\nabla}\cdot\mathbf{u})]_{i,j}\big\}, \tag{21}$$

where $\tilde{\partial}^q$ is a numerical operator approximating the partial derivative with respect to the q axis. Eq.(21) is the discrete counterpart of Eq.(10). It is not trivial to satisfy Eq.(21), which requires delicate design of the numerical scheme. Another way to achieve the *consistency of reduction* is to use the identity in the continuous level, i.e.,

$$\nabla\cdot(\mu(\nabla\mathbf{u})^T)=\nabla\mu\cdot(\nabla\mathbf{u})^T+\mu\nabla(\nabla\cdot\mathbf{u})=\nabla\mu\cdot(\nabla\mathbf{u})^T. \tag{22}$$

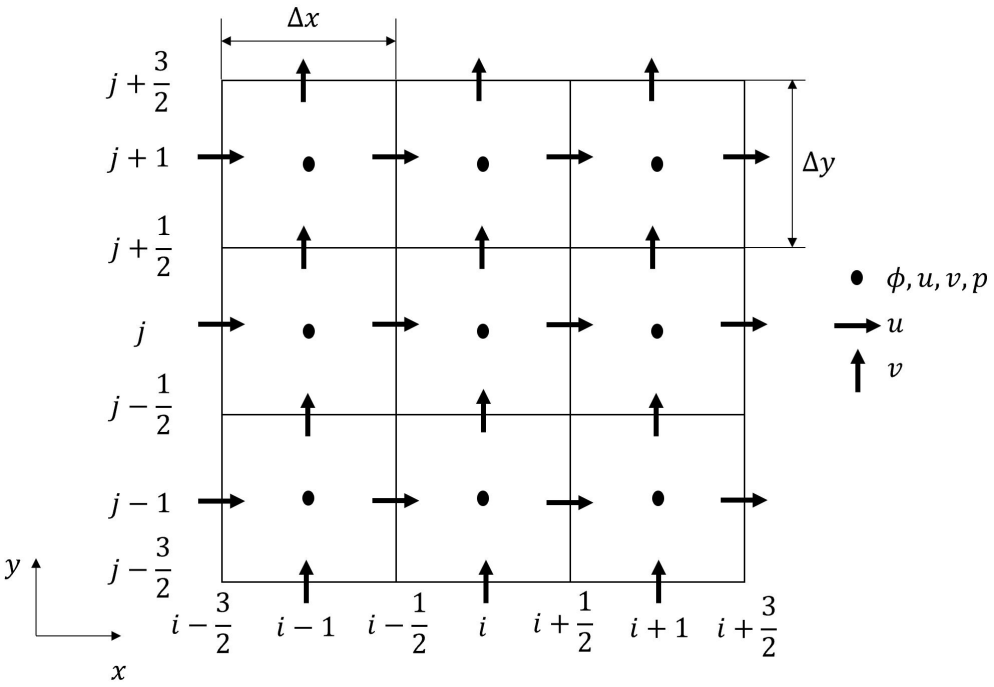

Fig. 1: Two-dimensional schematic of the collocated grid arrangement.

Instead of approximating $\nabla \cdot (\mu(\nabla \mathbf{u})^T)$, $\nabla\mu \cdot (\nabla \mathbf{u})^T$ is discretized [56]. Although $\nabla\mu \cdot (\nabla \mathbf{u})^T$ satisfies the *consistency of reduction*, it is written in a non-conservative form and in general fails to achieve the conservation of momentum in the discrete level.

In order to achieve not only the *consistency of reduction* but also the conservation of the viscous term in the discrete level, we stick to the conservative form $\nabla \cdot (\mu(\nabla \mathbf{u})^T)$. A numerical scheme for $\nabla \cdot (\mu(\nabla \mathbf{u})^T)$ is developed, which is conservative and satisfies Eq.(21) for all the interior and boundary cells. Details of the scheme and the proof are in Section 3.1. We continue this section by focusing on achieving the discrete consistency of the mass flux $\tilde{\mathbf{m}}$.

Three discrete mass fluxes are going to be discussed. The first one is the discrete inconsistent mass flux

$$\tilde{\mathbf{m}}^{IC} = \tilde{\rho}\mathbf{u}. \tag{23}$$

The second one is the direct discretization of Eq.(16) the consistent mass flux in the continuous level

$$\tilde{\mathbf{m}}^{CC} = \frac{\rho_1 + \rho_2}{2}\mathbf{u} + \frac{\rho_1 - \rho_2}{2}(\mathbf{u}\tilde{\phi} - M\tilde{\nabla}\xi). \tag{24}$$

The last one is called the consistent mass flux in the discrete level $\tilde{\mathbf{m}}^{DC}$, which achieves the *consistency of mass conservation*, i.e., the consistency between the semi-discrete mass conservation equation with $S_m = 0$

$$\frac{\partial \rho}{\partial t} + \tilde{\nabla} \cdot \tilde{\mathbf{m}}^{DC} = 0, \tag{25}$$

and the one implicitly defined by the density equation Eq.(5) and the semi-discrete Phase-Field equation

$$\frac{\partial \phi}{\partial t} + \tilde{\nabla} \cdot (\mathbf{u}\tilde{\phi}) = \tilde{\nabla} \cdot (M\tilde{\nabla}\xi^*), \tag{26}$$

where ξ^* is the numerical chemical potential. Sometimes, a numerical chemical potential is defined to make the computation simpler and more efficient, so we keep this possibility and use the notation ξ^* to distinguish the numerical chemical potential from the analytical one Eq.(2). From Eq.(5) and the discrete divergence-free condition Eq.(20), we can obtain

$$\tilde{\mathbf{m}}^{DC} = \frac{\rho_1 + \rho_2}{2}\mathbf{u} + \frac{\rho_1 - \rho_2}{2}(\mathbf{u}\tilde{\phi} - M\tilde{\nabla}\xi^*). \tag{27}$$

In order to achieve the *consistency of reduction*, ξ^* should be zero when $\phi \equiv 1(-1)$. It should be noted that all the numerical schemes used in Eq.(27) are identical to those used in Eq.(26). However, different numerical schemes can be used in Eq.(24) and Eq.(26). In addition, Eq.(24) uses the analytical chemical potential Eq.(2) instead of the numerical one. As we will show in the following, Eq.(24) fails to achieve consistency in the discrete level, although its continuous counterpart achieves consistency in the continuous level.

In order to illustrate how to achieve the consistency conditions in the discrete level, a simple one-dimensional advection case is analyzed. In this case, an interface is moving along the x direction. Following the analysis in the continuous level given in Section 2.1, all the forces are neglected. The physical and the only admissible solution that satisfies the divergence-free condition is that $u \equiv u_0$, where u_0 is a constant. As we will show, without delicate consideration of consistency in the discrete level, the numerical solution fails to reproduce the physical one even in such a simple problem.

Without loss of generality, we consider the time discretization scheme for any variable f as

$$\frac{\partial f}{\partial t} \approx \frac{\tilde{\partial} f}{\tilde{\partial} t} = \frac{\gamma_t f^{n+1} - \hat{f}}{\Delta t}, \tag{28}$$

where γ_t is a scheme dependent constant, e.g., $\gamma_t = 1$ for the Euler scheme, $\hat{f}$ is a linear combination of f^n, f^{n-1}, f^{n-2} etc., e.g., $\hat{f} = f^n$ for the Euler scheme, and Δt is the time step size. It should be noted that the time discretization scheme should satisfy $\gamma_t f = \hat{f}$ when f is an arbitrary constant. Similarly, we will use $\gamma_t^{(l)}$ and $\hat{f}^{(l)}$ to distinguish different time discretization scheme if necessary. We further simplify the problem such that all the cell-center and cell-face velocities in previous time steps are equal to the exact value u_0.

The fully discretized Phase-Field and momentum conservation equations for cell i are

$$\frac{\gamma_t^{(1)}\phi_i^{n+1} - \hat{\phi}_i^{(1)}}{\Delta t} + u_0\frac{\tilde{\phi}_{i+1/2}^{(1)} - \tilde{\phi}_{i-1/2}^{(1)}}{\Delta x} = \frac{(M\tilde{\nabla}^{x,(1)}\xi^*)_{i+1/2} - (M\tilde{\nabla}^{x,(1)}\xi^*)_{i-1/2}}{\Delta x}, \tag{29}$$

$$\frac{\gamma_t^{(2)}\rho_i^{n+1}u_i^{n+1}-u_0\hat{\rho}_i^{(2)}}{\Delta t}+u_0\frac{\tilde{m}_{i+1/2}^x-\tilde{m}_{i-1/2}^x}{\Delta x}=0. \tag{30}$$

The right-hand side of Eq.(30) is zero because of the force-free condition. We can obtain the solutions of the Phase-Field function and cell-center velocity at the new time step from Eq.(5), Eq.(29) and Eq.(30) as

$$\phi_i^{n+1}=\frac{\hat{\phi}_i^{(1)}}{\gamma_t^{(1)}}-\frac{\Delta t}{\gamma_t^{(1)}}\big[u_0\frac{\tilde{\phi}_{i+1/2}^{(1)}-\tilde{\phi}_{i-1/2}^{(1)}}{\Delta x}-\frac{(M\tilde{\nabla}^{x,(1)}\xi^*)_{i+1/2}-(M\tilde{\nabla}^{x,(1)}\xi^*)_{i-1/2}}{\Delta x}\big], \tag{31}$$

$$\begin{aligned}\rho_i^{n+1}=\frac{\rho_1+\rho_2}{2}+\frac{\rho_1-\rho_2}{2}\big\{\frac{\hat{\phi}_i^{(1)}}{\gamma_t^{(1)}}-\frac{\Delta t}{\gamma_t^{(1)}}\big[u_0\frac{\tilde{\phi}_{i+1/2}^{(1)}-\tilde{\phi}_{i-1/2}^{(1)}}{\Delta x}\\ -\frac{(M\tilde{\nabla}^{x,(1)}\xi^*)_{i+1/2}-(M\tilde{\nabla}^{x,(1)}\xi^*)_{i-1/2}}{\Delta x}\big]\big\},\end{aligned} \tag{32}$$

$$u_i^{n+1}=\frac{\rho_i^*}{\rho_i^{n+1}}u_0, \tag{33}$$

where

$$\rho_i^*=\frac{\rho_1+\rho_2}{2}+\frac{\rho_1-\rho_2}{2}\frac{\hat{\phi}_i^{(2)}}{\gamma_t^{(2)}}-\frac{\Delta t}{\gamma_t^{(2)}}\frac{\tilde{m}_{i+1/2}^x-\tilde{m}_{i-1/2}^x}{\Delta x}. \tag{34}$$

Obviously, if $\rho_i^*=\rho_i^{n+1}$, the exact solution $u_i^{n+1}=u_0$ is obtained. However, ρ_i^* depends on the discrete mass flux $\tilde{m}^x$.

We consider the discrete inconsistent mass flux $\tilde{m}^{IC,x}=\tilde{\rho}^{(2)}u_0$ Eq.(23), the discrete consistent mass flux in the continuous level $\tilde{m}^{CC,x}=\frac{\rho_1+\rho_2}{2}u_0+\frac{\rho_1-\rho_2}{2}(u_0\tilde{\phi}^{(3)}-M\tilde{\nabla}^{x,(3)}\xi)$ Eq.(24), and the consistent mass flux in the discrete level $\tilde{m}^{DC,x}=\frac{\rho_1+\rho_2}{2}u_0+\frac{\rho_1-\rho_2}{2}(u_0\tilde{\phi}^{(1)}-M\tilde{\nabla}^{x,(1)}\xi^*)$ Eq.(27). The superscripts represent different numerical schemes. For example, $\tilde{\phi}^{(1)}$ represents the linear interpolation while $\tilde{\phi}^{(2)}$ represents the quadratic interpolation. The difference between the corresponding ρ_i^* and ρ_i^{n+1} are

$$\begin{aligned}\rho_i^{*,IC}-\rho_i^{n+1}=\frac{\rho_1-\rho_2}{2}\big(\frac{\hat{\phi}_i^{(2)}}{\gamma_t^{(2)}}-\frac{\hat{\phi}_i^{(1)}}{\gamma_t^{(1)}}\big)\\ -\frac{u_0\Delta t}{\Delta x}\big(\frac{\tilde{\rho}_{i+1/2}^{(2)}-\tilde{\rho}_{i-1/2}^{(2)}}{\gamma_t^{(2)}}-\frac{\rho(\tilde{\phi}_{i+1/2}^{(1)})-\rho(\tilde{\phi}_{i-1/2}^{(1)})}{\gamma_t^{(1)}}\big)\\ -\frac{\rho_1-\rho_2}{2}\frac{\Delta t}{\gamma_t^{(1)}}\frac{(M\tilde{\nabla}^{x,(1)}\xi^*)_{i+1/2}-(M\tilde{\nabla}^{x,(1)}\xi^*)_{i-1/2}}{\Delta x},\end{aligned} \tag{35}$$

$$
\begin{aligned}
\rho_i^{*,CC} - \rho_i^{n+1} &= \frac{\rho_1 - \rho_2}{2}\big(\frac{\hat{\phi}_i^{(2)}}{\gamma_t^{(2)}} - \frac{\hat{\phi}_i^{(1)}}{\gamma_t^{(1)}}\big) \\
-\frac{\rho_1 - \rho_2}{2}\frac{u_0 \Delta t}{\Delta x}\big(&\frac{\tilde{\phi}_{i+1/2}^{(3)} - \tilde{\phi}_{i-1/2}^{(3)}}{\gamma_t^{(2)}} - \frac{\tilde{\phi}_{i+1/2}^{(1)} - \tilde{\phi}_{i-1/2}^{(1)}}{\gamma_t^{(1)}}\big) \\
+\frac{\rho_1 - \rho_2}{2}\frac{\Delta t}{\Delta x}\big[&\frac{(M\tilde{\nabla}^{x,(3)}\xi)_{i+1/2} - (M\tilde{\nabla}^{x,(3)}\xi)_{i-1/2}}{\gamma_t^{(2)}} \\
&- \frac{(M\tilde{\nabla}^{x,(1)}\xi^*)_{i+1/2} - (M\tilde{\nabla}^{x,(1)}\xi^*)_{i-1/2}}{\gamma_t^{(1)}}\big],
\end{aligned} \tag{36}
$$

$$
\begin{aligned}
\rho_i^{*,DC} - \rho_i^{n+1} &= \frac{\rho_1 - \rho_2}{2}\big(\frac{\hat{\phi}_i^{(2)}}{\gamma_t^{(2)}} - \frac{\hat{\phi}_i^{(1)}}{\gamma_t^{(1)}}\big) \\
-\frac{\rho_1 - \rho_2}{2}\Delta t\big(\frac{1}{\gamma_t^{(2)}} - \frac{1}{\gamma_t^{(1)}}\big)\big(&u_0 \frac{\tilde{\phi}_{i+1/2}^{(1)} - \tilde{\phi}_{i-1/2}^{(1)}}{\Delta x} \\
&- \frac{(M\tilde{\nabla}^{x,(1)}\xi^*)_{i+1/2} - (M\tilde{\nabla}^{x,(1)}\xi^*)_{i-1/2}}{\Delta x}\big).
\end{aligned} \tag{37}
$$

From Eq.(35)-Eq.(37), none of the discrete mass fluxes unconditionally satisfy the consistency conditions in the discrete level. The inconsistency can be categorized into four parts. The first part comes from using different time discretization scheme in the Phase-Field and momentum equations. This is the first term in the right-hand side of Eq.(35)-Eq.(37). If the same time discretization scheme is used, i.e. $\gamma_t^{(1)} = \gamma_t^{(2)}$ and $\hat{\phi}^{(1)} = \hat{\phi}^{(2)}$, this inconsistency can be resolved. Under this circumstance, the second term on the right-hand side of Eq.(37) also becomes zero because the factor $\big(\frac{1}{\gamma_t^{(1)}} - \frac{1}{\gamma_t^{(2)}}\big)$ equals to zero. The second part is introduced by the mismatch of the numerical schemes used to discretize the Phase-Field equation and the mass flux in space. The second term on the right-hand side of Eq.(35) and Eq.(36) belongs to this category. It is easy to resolve this inconsistency in Eq.(36) by requiring $\tilde{\phi}^{(3)} = \tilde{\phi}^{(1)}$ and $\tilde{\nabla}^{(3)} = \tilde{\nabla}^{(1)}$. However, it becomes more complicated in Eq.(35) when a nonlinear scheme is used, since $\tilde{\rho}^{(2)}$ is not necessarily equal to $\rho(\tilde{\phi}^{(2)})$ in general. In other words, $\tilde{\phi}^{(2)} = \tilde{\phi}^{(1)}$ doesn't guarantee to resolve the inconsistency in Eq.(35). The only guaranteed way is to compute $\tilde{\rho}$ by $\rho(\tilde{\phi}^{(1)})$. The third part results from using the analytical chemical potential Eq.(2) instead of the numerical one. The third term on the right-hand side of Eq.(36) is the case. Even if we remove the first and the second source of inconsistency, this term still remains because $\xi - \xi^*$ is in general non-zero. The last part is due to violating the *consistency of mass conservation*, which is the last term in Eq.(35).

Our analysis shows that the physical solution of such a simple case is only obtained when using the consistent mass flux in the discrete level $\tilde{\mathbf{m}}^{DC}$ and

using the same time discretization scheme for the Phase-Field and momentum conservation equations. Another observation is that all the inconsistent errors are proportional to the density difference between the two fluids, i.e., $\rho_1 - \rho_2$, implying that these errors could be more significant as the density ratio of the fluids increases.

The consistency in the discrete level is more involved because, unlike in the continuous level, the *consistency of mass and momentum transport* is not necessarily guaranteed. We have shown that, although $\mathbf{m}^{CC}$ satisfies all the consistency conditions in the continuous level, careless discretization of $\mathbf{m}^{CC}$ can violate the *consistency of mass and momentum transport*, and consequently leads to inconsistency in the discrete level. Here, we summarize the key points to achieve consistency in the discrete level.

Remarks: To achieve consistency in the discrete level

1. Determine the consistent mass flux in the continuous level m^{CC}, which satisfies the consistency conditions proposed in Section 2.1.
2. To achieve the *consistency of mass and momentum transport* in the discrete level,
   - the time discretization scheme of the momentum conservation equation should be identical to the one of the Phase-Field equation, and
   - the numerical scheme used to discretize m^{CC} should be identical to those used to solve the Phase-Field equation.
3. To achieve the *consistency of mass conservation* in the discrete level,
   - the numerical chemical potential, if there is any, should replace the analytical one in m^{CC}.
4. To achieve the *consistency of reduction* in the discrete level,
   - the numerical chemical potential, if there is any, should be zero when $\phi \equiv 1(-1)$, and
   - the discretization of $\nabla \cdot (\mu(\nabla \mathbf{u})^T)$ should be zero when μ is constant.

3 Discretization

3.1 Spatial Discretization

In this section, all the discrete operators are to be defined in detail. For simplicity, we provide the definitions in two dimensions, while their extension to three dimensional problems is straightforward. We use (x_i, y_j) to denote the cell center, and $(x_{i+1/2}, y_j)$ and $(x_i, y_{j+1/2})$ to denote the cell face. A scalar function defined at the cell center (x_i, y_j) is denoted by $f_{i,j}$. A vector function $\mathbf{f}$ is defined at the cell face, when its x-component f^x is defined at $(x_{i+1/2}, y_j)$, i.e., $f^x_{i+1/2,j}$, while its y component f^y is defined at $(x_i, y_{j+1/2})$, i.e., $f^y_{i,j+1/2}$. We use Δx and Δy to denote the cell size, or grid size, along the x and y axis, respectively.

Close to the domain boundary, we assign the ghost points outside the computational domain so that we don't need to modify the discrete operators. The ghost-point values are determined, based on the boundary conditions. For the periodic boundary condition, we assign the ghost-point values by copying their

corresponding ones inside the computational domain. For the other boundary conditions, we use the linear extrapolation or the 2nd-order central difference, unless otherwise specified.

The discrete operators defined below are formally 2nd-order accurate, either discretely conservative or balanced-force, and easy to be implemented. Most of them have compact stencil. We would like to emphasis that the proposed method can be used for higher order schemes as long as they are consistent and conservative in the discrete level.

Lagrangian interpolation The Lagrangian interpolation is denoted as

$$[\bar{f}]_{i,j}^{x,p,q} = \overline{(f_{i-p,j}, f_{i-p+1,j}, ..., f_{i+q,j})}, \tag{38}$$

where f is a scalar function defined at $(x_{i-p+k}, y_j)_{k=0}^{p+q}$. Eq(38) denotes the Lagrangian interpolation along the x axis at point (x_i, y_j) with a p-left-bias and q-right-bias stencil. We denote the frequently-used linear interpolation with $p = q = \frac{1}{2}$ at point (x_i, y_j) as

$$[\bar{f}]_{i,j}^{x} \equiv [\bar{f}]_{i,j}^{x,1/2,1/2} = \overline{(f_{i-1/2,j}, f_{i+1/2,j})}. \tag{39}$$

The interpolation along the other axis can be defined in the same manner.

Discrete divergence operator The discrete divergence operator is defined as

$$\begin{aligned}[\tilde{\nabla} \cdot (\mathbf{f}_1 \tilde{f}_2)]_{i,j} = &\frac{f_{1,i+1/2,j}^{x} \tilde{f}_{2,i+1/2,j} - f_{1,i-1/2,j}^{x} \tilde{f}_{2,i-1/2,j}}{\Delta x} \\ &+ \frac{f_{1,i,j+1/2}^{y} \tilde{f}_{2,i,j+1/2} - f_{1,i,j-1/2}^{y} \tilde{f}_{2,i,j-1/2}}{\Delta y},\end{aligned} \tag{40}$$

where $\mathbf{f}_1$ is a vector function defined at the cell face while f_2 is a scalar function defined at the cell center. In this case, we directly use the nodal values of $\mathbf{f}_1$ while numerical evaluation has to be performed to specify $\tilde{f}_2$ from its nodal values f_2. Here we use the 5th-order WENO scheme [32], which is very robust and provides accurate results. It should be noted that the discrete divergence operator should be formally 2nd-order accurate even when a high-order numerical scheme is implemented to evaluate $\tilde{f}_2$. However, the error would be smaller when a high-order scheme is used [40]. To achieve higher order of accuracy, a more sophisticated interpolation has to be performed on $f_{1,i\pm1/2,j}^{x}$ and $f_{1,i,j\pm1/2}^{y}$, and readers can refer to [40,44,15].

Discrete gradient operator Two discrete gradient operators are defined, one is at the cell face

$$[\tilde{f}_2 \tilde{\nabla}^x f_1]_{i+1/2,j} = \tilde{f}_{2,i+1/2,j} \frac{f_{1,i+1,j} - f_{1,i,j}}{\Delta x}, \tag{41}$$

and the other is at the cell center

$$[\overline{\tilde{f}_2\tilde{\nabla}^x f_1}]^x_{i,j} = \overline{([\tilde{f}_2\tilde{\nabla}^x f_1]_{i-1/2,j}, [\tilde{f}_2\tilde{\nabla}^x f_1]_{i+1/2,j})}, \tag{42}$$

where f_1 and f_2 are both scaler functions defined at the cell center. $\tilde{f}_{2,i+1/2,j}$ has to be numerically evaluated from the nodal values of f_2. Unless otherwise specified, we use linear interpolation, i.e., $\tilde{f}_{2,i+1/2,j} = [\overline{f_2}]^x_{i+1/2,j}$. The discrete gradient operator along the other axis can be similarly defined. These discrete gradient operators are formally 2nd-order accurate due to the linear interpolation and the 2nd-order central difference in Eq.(41) and Eq.(42).

Discrete Laplace operator The discrete Laplace operator successively uses the discrete divergence operator Eq.(40) and the discrete gradient operator Eq.(41), which results in

$$\begin{aligned}[\tilde{\nabla}\cdot(\tilde{f}_2\tilde{\nabla}f_1)]_{i,j} = &\frac{1}{\Delta x}\big(\tilde{f}_{2,i+1/2,j}\frac{f_{1,i+1,j}-f_{1,i,j}}{\Delta x}\\ &-\tilde{f}_{2,i-1/2,j}\frac{f_{1,i,j}-f_{1,i-1,j}}{\Delta x}\big)\\ &+\frac{1}{\Delta y}\big(\tilde{f}_{2,i,j+1/2}\frac{f_{1,i,j+1}-f_{1,i,j}}{\Delta y}\\ &-\tilde{f}_{2,i,j-1/2}\frac{f_{1,i,j}-f_{1,i,j-1}}{\Delta y}\big),\end{aligned} \tag{43}$$

where both f_1 and f_2 are scalar functions defined at the cell center. Unless otherwise specified, $\tilde{f}_2$ is evaluated by the linear interpolation and this discrete operator should be formally 2nd-order accurate. Special attention should be paid to the Dirichlet boundary condition, where an $O(1)$ error will appear when linear extrapolation is used to specify the ghost-point values outside the domain. This can be easily shown by Taylor expansion. To resolve this error while maintaining a compact stencil, a parabolic extrapolation, whose stencil consists of the boundary and the two cells nearest to the boundary, is used to specify the ghost point value.

Discrete Divergence-Gradient-Transpose operator We name the operator $\nabla\cdot(f_2(\nabla\mathbf{f_1})^T)$, which appears in the viscous term in the momentum equation Eq.(9) with $f_2 = \mu$ and $\mathbf{f_1} = \mathbf{u}$, the Divergence-Gradient-Transpose operator. This discrete operator is related to the *consistency of reduction* of the viscous term, as mentioned in Section 2.2.

We use the same discrete divergence Eq.(40) and gradient Eq.(41) operators, and obtain the discrete Divergence-Gradient-Transpose operator

$$\begin{aligned}[\tilde{\nabla}\cdot(\tilde{f}_2(\tilde{\nabla}\tilde{\mathbf{f}}_1)^T)]^x_{i,j} = \frac{1}{\Delta x}\big(&\tilde{f}_{2,i+1/2,j}\frac{\tilde{f}^x_{1,i+1,j}-\tilde{f}^x_{1,i,j}}{\Delta x}\\ &-\tilde{f}_{2,i-1/2,j}\frac{\tilde{f}^x_{1,i,j}-\tilde{f}^x_{1,i-1,j}}{\Delta x}\big)\\ +\frac{1}{\Delta y}\big(&\tilde{f}_{2,i,j+1/2}\frac{\tilde{f}^y_{1,i+1/2,j+1/2}-\tilde{f}^y_{1,i-1/2,j+1/2}}{\Delta x}\\ &-\tilde{f}_{2,i,j-1/2}\frac{\tilde{f}^y_{1,i+1/2,j-1/2}-\tilde{f}^y_{1,i-1/2,j-1/2}}{\Delta x}\big),\end{aligned} \tag{44}$$

where $\mathbf{f}_1$ is a vector function defined at the cell face, f_2 is a scalar function defined at the cell center, and $\tilde{f}_2$, unless otherwise specified, is evaluated by the linear interpolation. Eq.(44) is formally 2nd-order accurate. $[\tilde{\nabla}\cdot(\tilde{f}_2(\tilde{\nabla}\tilde{\mathbf{f}}_1)^T)]^y_{i,j}$ can be similarly defined. Using an appropriate definition of $\tilde{f}_1$, Eq.(44) satisfies the discrete chain rule as in Eq.(21). Terms $\tilde{f}^x_{1,i,j}$ and $\tilde{f}^y_{1,i+1/2,j+1/2}$ in Eq.(44) are computed by

$$\tilde{f}^x_{1,i,j} = [\overline{f^x_1}]^x_{i,j} = \frac{1}{2}(f^x_{1,i+1/2,j} + f^x_{1,i-1/2,j}), \tag{45}$$

and

$$\tilde{f}^y_{1,i+1/2,j+1/2} = [\overline{f^y_1}]^x_{i+1/2,j+1/2} = \frac{1}{2}(f^y_{1,i,j+1/2} + f^y_{1,i+1,j+1/2}). \tag{46}$$

When f_2 doesn't change around (x_i, y_j), from Eq.(44), Eq.(45) and Eq.(46), we can obtain

$$\begin{aligned}[\tilde{\nabla}\cdot(\tilde{f}_2(\tilde{\nabla}\tilde{\mathbf{f}}_1)^T)]^x_{i,j} &= \frac{1}{2}\frac{1}{\Delta x}f_2\big(\frac{f^x_{1,i+3/2,j}-f^x_{1,i+1/2,j}}{\Delta x}\\ &\quad+\frac{f^y_{1,i+1,j+1/2}-f^y_{1,i+1,j-1/2}}{\Delta y}\\ &\quad-\frac{f^x_{1,i-1/2,j}-f^x_{1,i-3/2,j}}{\Delta x}\\ &\quad-\frac{f^y_{1,i-1,j+1/2}-f^y_{1,i-1,j-1/2}}{\Delta y}\big)\\ &= f_2\frac{[\tilde{\nabla}\cdot\mathbf{f}_1]_{i+1,j}-[\tilde{\nabla}\cdot\mathbf{f}_1]_{i-1,j}}{2\Delta x}\\ &= f_2[\tilde{\partial}^{x,CD}(\tilde{\nabla}\cdot\mathbf{f_1})]_{i,j},\end{aligned} \tag{47}$$

where $\tilde{\partial}^{q,CD}$ is the central difference operator along the q axis. Eq.(47) shows the discrete chain rule, i.e., the discrete counterpart of Eq.(10) and works for all the interior cells.

Special care has to be paid to the cells close to the boundary so that the discrete chain rule in Eq.(21) is maintained. Consider the boundary cell where

$f^x_{1,i-3/2,j}$ and $f^y_{1,i-1,j\pm1/2}$ in Eq.(44) are outside of the domain and are replaced by the ghost-point values $\tilde{f}^x_{1,i-3/2,j}$ and $\tilde{f}^y_{1,i-1,j\pm1/2}$. These ghost-point values are defined carefully to achieve the discrete chain rule at the boundary cells. By defining

$$\tilde{f}^x_{1,i-3/2,j} = [\overline{f^x_1}]^{x,-1,3}_{i-3/2,j} = 3f^x_{1,i-1/2,j} - 3f^x_{1,i+1/2,j} + f^x_{1,i+3/2,j}, \tag{48}$$

and

$$\tilde{f}^y_{1,i-1,j\pm1/2} = [\overline{f^y_1}]^{x,-1,2}_{i-1,j\pm1/2} = 2f^y_{1,i,j\pm1/2} - f^y_{1,i+1,j\pm1/2}, \tag{49}$$

we use Eq.(48) and Eq.(49) to replace $f^x_{1,i-3/2,j}$ and $f^y_{1,i-1,j\pm1/2}$ in Eq.(44) while the other terms in Eq.(44) are computed following Eq.(45) and Eq.(46). After doing that, we can obtain

$$[\tilde{\nabla}\cdot(\tilde{f}_2(\tilde{\nabla}\tilde{\mathbf{f}}_1)^T)]^x_{i,j} = f_2\frac{1}{\Delta x}\big([\tilde{\nabla}\cdot\mathbf{f}_1]_{i+1,j} - [\tilde{\nabla}\cdot\mathbf{f}_1]_{i,j}\big) = f_2[\tilde{\partial}^{x,FD}(\tilde{\nabla}\cdot\mathbf{f}_1)]_{i,j}, \tag{50}$$

where $\tilde{\partial}^{q,FD}$ represents the forward differencing along the q axis and f_2 is constant around (x_i, y_j). The same result can be obtained at the other side of the boundary except that $\tilde{\partial}^{x,FD}$ is replaced by $\tilde{\partial}^{x,BD}$, where $\tilde{\partial}^{q,BD}$ is the backward differencing along the q axis. Extension to other axis and to three dimension is straightforward and not repeated here.

3.2 Balanced-Force algorithm

When there is no flow, i.e., $\mathbf{u} = \mathbf{0}$, the momentum equation Eq.(9) reduces to

$$\mathbf{0} = -\frac{1}{\rho}\nabla p + \mathbf{g} + \frac{1}{\rho}\xi\nabla\phi + \frac{1}{\rho}\mathbf{S}_\mathbf{u}, \tag{51}$$

which represents the force balance between the pressure, gravity, surface tension, and other external forces. The residual from the discrete force imbalance nonphysically drives the flow to move, and generates the so-called spurious current. The balanced-force algorithm is developed by [24] for both the continuous surface force [9] and the ghost fluid method [23]. Here we follow this idea and apply it to the surface force from the Phase-Field model.

The x-component of Eq.(51) is first discretized at $(x_{i+1/2}, y_j)$ as

$$G^x_{s,i+1/2,j} = g^x + \frac{1}{\tilde{\rho}_{i+1/2,j}}[\tilde{\xi}\tilde{\nabla}^x\phi]_{i+1/2,j} + \frac{1}{\tilde{\rho}_{i+1/2,j}}S^x_{\mathbf{u},i+1/2,j}, \tag{52}$$

and

$$G^x_{i+1/2,j} = -\frac{1}{\tilde{\rho}_{i+1/2,j}}[\tilde{\nabla}^x p]_{i+1/2,j} + G^x_{s,i+1/2,j}, \tag{53}$$

where, unless otherwise specified, $\tilde{\rho}$ is evaluated by the linear interpolation. It should be noted that the discrete gradient operators for p and ϕ are defined identically as Eq.(41). The y-component is similarly discretized at $(x_i, y_{j+1/2})$. The cell-center $\overline{\mathbf{G}}$ at (x_i, y_j) is linearly interpolated from $G^x_{i+1/2,j}$ and $G^y_{i,j+1/2}$, i.e.,

$$[\overline{\mathbf{G}}]_{i,j} = \Big\{[\overline{G^x}]^x_{i,j}, [\overline{G^y}]^y_{i,j}\Big\}. \tag{54}$$

3.3 Temporal Discretization

In this section, the temporal discretization for the Cahn-Hilliard equations Eq.(1)-Eq.(4) and the Navier-Stokes equations Eq.(8)-Eq.(9) are described. Suppose the Phase-Field function ϕ, the cell-center velocity $\mathbf{u}$, and the pressure p, which are defined at the cell center (x_i, y_j), and the cell-face velocity $\mathbf{u}$, which is defined at the cell face $(x_{i+1/2}, y_j)$ and $(x_i, y_{j+1/2})$, in time levels n and all the previous time level, i.e., $(n-1), (n-2), ...$, are known. We define $f^{*,n+1}$ as an explicit evaluation of f^{n+1} from previous time level of f, where f is the variable of interest.

Cahn-Hilliard equations We follow the temporal discretization scheme in [22] to split the original 4th-order Phase-Field equation Eq.(1) into two 2nd-order Helmholtz equations that can be solved sequentially. The first step is to solve the auxiliary variable ψ^* from

$$\tilde{\nabla}\cdot(\tilde{\nabla}\psi^*) - \big(\alpha + \frac{S}{\eta^2}\big)\psi^* = \frac{1}{\lambda M}\big[\frac{\hat{\phi}}{\Delta t} - \tilde{\nabla}\cdot(\mathbf{u}^{*,n+1}\tilde{\phi}^{*,n+1}) + S_\phi^{n+1}\big] \\ +\tilde{\nabla}\cdot(\tilde{\nabla}F'(\phi^{*,n+1})) - \frac{S}{\eta^2}\tilde{\nabla}\cdot(\tilde{\nabla}\phi^{*,n+1}), \tag{55}$$

with boundary condition

$$\mathbf{n}\cdot\tilde{\nabla}\psi^* = \mathbf{n}\cdot\tilde{\nabla}\left[F'(\phi^{*,n+1}) - \frac{S}{\eta^2}\phi^{*,n+1}\right] + (\alpha + \frac{S}{\eta^2})(\mathbf{n}\cdot\tilde{\nabla}\phi^{n+1}), \tag{56}$$

which is equivalent to $\mathbf{n}\cdot\tilde{\nabla}\xi^* = 0$ at boundary with ξ^* defined in Eq.(61). This boundary condition ensures global conservation of the Phase-Field function ϕ in the discrete level. The second step is to solve the Phase-Field function at new time step ϕ^{n+1} from

$$\tilde{\nabla}\cdot(\tilde{\nabla}\phi^{n+1}) + \alpha\phi^{n+1} = \psi^*, \tag{57}$$

with boundary condition

$$\mathbf{n}\cdot\tilde{\nabla}\phi^{n+1} = \frac{1}{2}\frac{\sigma}{\lambda}\cos(\theta_s)\big[\frac{\pi}{2}\cos\big(\frac{\pi}{2}\phi^{*,n+1}\big)\big]. \tag{58}$$

This boundary condition is from [31] and includes the steady contact angle θ_s. The effectiveness of this contact angle boundary condition is validated by the case named equilibrium drop in the Appendix. We refer interested readers to [31,51,73], for understanding this kind of contact angle boundary condition, to [18,21,6] for more detailed numerical implementations and validations, and to [16,38] for other possible options of imposing the contact angle boundary condition. Unless otherwise specified, the boundary conditions Eq.(56) and Eq.(58) are used with $\theta_s = 90^0$ when we solve the Phase-Field equation. The α and S in Eq.(55)-Eq.(58) are defined as

$$\alpha = -\frac{S}{2\eta^2}\big[1 + \sqrt{1 - \frac{4\gamma_t}{\lambda M \Delta t}\frac{\eta^4}{S^2}}\big], \tag{59}$$

$$\frac{S}{\eta^2} \geq \sqrt{\frac{4\gamma_t}{\lambda M \Delta t}}. \tag{60}$$

This scheme leads to a numerical chemical potential defined as

$$\xi^* = \lambda\big(F'(\phi^{*,n+1}) - \tilde{\nabla}\cdot(\tilde{\nabla}\phi^{n+1})\big) + \frac{\lambda S}{\eta^2}(\phi^{n+1} - \phi^{*,n+1}). \tag{61}$$

Navier-Stokes equations We construct a projection scheme to decouple the pressure and velocity. After solving ϕ^{n+1}, we can obtain the density ρ^{n+1} and viscosity μ^{n+1} of the fluid mixture from Eq.(5) and Eq.(6), respectively. The first two step is to evaluate $\mathbf{u}^*$ and $\mathbf{u}^{**}$ at the cell center (x_i, y_j) from

$$\begin{aligned}\frac{\gamma_t\rho^{n+1}\mathbf{u}^* - \rho\hat{\mathbf{u}}}{\Delta t} + \tilde{\nabla}\cdot(\tilde{\mathbf{m}}\otimes\tilde{\mathbf{u}}^{*,n+1}) = \rho^{n+1}\overline{\mathbf{G}^n} + \tilde{\nabla}\cdot(\tilde{\mu}^{n+1}\tilde{\nabla}\mathbf{u}^*) \\ +\tilde{\nabla}\cdot(\tilde{\mu}^{n+1}(\tilde{\nabla}\tilde{\mathbf{u}}^{*,n+1})^T),\end{aligned} \tag{62}$$

and

$$\frac{\gamma_t\mathbf{u}^{**} - \gamma_t\mathbf{u}^*}{\Delta t} = -\overline{\mathbf{G}^n}. \tag{63}$$

$\mathbf{u}^{**}$ is linearly interpolated from the cell center (x_i, y_j) to the cell face $(x_{i+1/2}, y_j)$ and $(x_i, y_{j+1/2})$. We obtain $\mathbf{u}^*$ at the cell face, as proposed by Rhie and Chow[53], from

$$\frac{\gamma_t\mathbf{u}^* - \gamma_t\overline{\mathbf{u}^{**}}}{\Delta t} = -\frac{1}{\tilde{\rho}^{n+1}}\tilde{\nabla}p^n + \mathbf{G}_s^{n+1}. \tag{64}$$

Here, we do the linear interpolation on ρ instead of $(1/\rho)$ and this works for the following equations including $\tilde{\rho}$ in this section. The cell face $\mathbf{u}^*$ is corrected by the pressure correction p' from

$$\frac{\gamma_t\mathbf{u}^{n+1} - \gamma_t\mathbf{u}^*}{\Delta t} = -\frac{1}{\tilde{\rho}^{n+1}}\tilde{\nabla}p', \tag{65}$$

such that the cell face $\mathbf{u}^{n+1}$ is discrete divergence-free, i.e.,

$$\tilde{\nabla}\cdot\mathbf{u}^{n+1} = 0, \tag{66}$$

at the cell center (x_i, y_j). By combining Eq.(65) and Eq.(66), we can obtain the discrete Laplace equation for the pressure correction p' at the cell center (x_i, y_j) as

$$\frac{\gamma_t}{\Delta t}\tilde{\nabla}\cdot\mathbf{u}^* = \tilde{\nabla}\cdot\big(\frac{1}{\tilde{\rho}^{n+1}}\tilde{\nabla}p'\big). \tag{67}$$

After solving Eq.(67), we can obtain the cell face $\mathbf{u}^{n+1}$ from Eq.(65) and the pressure p^{n+1} at the cell center (x_i, y_j) from

$$p^{n+1} = p^n + p'. \tag{68}$$

Finally, the velocity $\mathbf{u}^{n+1}$ at the cell center (x_i, y_j) is obtained from

$$\frac{\gamma_t\mathbf{u}^{n+1} - \gamma_t\mathbf{u}^{**}}{\Delta t} = \overline{\mathbf{G}^{n+1}}. \tag{69}$$

3.4 Accuracy, consistency, conservation and energy dissipation

As stated in Section 3.1, the formal order of accuracy of each discrete operator is 2nd-order. We focus on estimating the formal temporal order of accuracy, followed by the discussions of consistency, conservation, and energy dissipation in the discrete level, in this section.

The fully-discretized Phase-Field and momentum conservation equations are recovered from the equations in Section 3.3 as

$$\frac{\gamma_t \phi^{n+1} - \hat{\phi}}{\Delta t} + \tilde{\nabla} \cdot (\mathbf{u}^{*,n+1} \tilde{\phi}^{*,n+1}) = M \tilde{\nabla} \cdot (\tilde{\nabla} \xi^*) + S_\phi^{n+1}, \tag{70}$$

$$\frac{\gamma_t \rho^{n+1} \mathbf{u}^{n+1} - \rho \hat{\mathbf{u}}}{\Delta t} + \tilde{\nabla} \cdot (\tilde{\mathbf{m}} \otimes \tilde{\mathbf{u}}^{*,n+1}) = \rho^{n+1} \overline{\mathbf{G}^{n+1}} + \tilde{\nabla} \cdot (\tilde{\mu}^{n+1} \tilde{\nabla} \mathbf{u}^*) + \tilde{\nabla} \cdot (\tilde{\mu}^{n+1} (\tilde{\nabla} \tilde{\mathbf{u}}^{*,n+1})^T). \tag{71}$$

To discuss the formal order of accuracy, we have assumed that the solutions are smooth enough in time such that their Taylor expansions in time exist. There are two sources of temporal error. The first one comes from the time discretization scheme that approximates the time derivative, i.e., $\partial f / \partial t$ where f is either ϕ or $\rho \mathbf{u}$. Unless otherwise specified, we choose the 2nd-order backward differencing with $\gamma_t = 1.5$ and $\hat{f} = 2f^n - 0.5 f^{n-1}$. Formally 2nd-order accuracy is obtained if the other terms are evaluated at the time level $(n+1)$. However, this makes the nonlinear two-phase model fully coupled, and is difficult and costly to solve. Decoupling is designed to remedy the problems, i.e., the original 4th-order Cahn-Hilliard equation is decoupled with two 2nd-order Helmholtz equations, and the pressure and velocity are decoupled by the projection scheme. However, the decoupling introduces the second source of temporal error, i.e., the splitting error, which is going to be discussed.

We use, unless otherwise specified, the 2nd-order Adams-Bashforth scheme, i.e., $f^{*,n+1} = 2f^n - f^{n-1}$, so that $(\phi^{*,n+1} - \phi^{n+1}) \sim O(\Delta t^2)$ and $(\mathbf{u}^{*,n+1} - \mathbf{u}^{n+1}) \sim O(\Delta t^2)$ are true. From Eq.(2) and Eq.(61), we can obtain $(\xi^* - \xi^{n+1}) \sim O(\Delta t^2)$. From Eq.(68) we have $p' \sim O(\Delta t)$, resulting in, at the cell face, $(\mathbf{u}^* - \mathbf{u}^{n+1}) \sim O(\Delta t^2)$ from Eq.(65). By combining Eq.(63), Eq.(69), and $p' \sim O(\Delta t)$, we have $(\mathbf{u}^* - \mathbf{u}^{n+1}) \sim O(\Delta t^2)$ at the cell center. Finally, all the terms in Eq.(70) and Eq.(71) that are not evaluated at $(n+1)$ time level are different from their corresponding ones evaluating at $(n+1)$ time level by $O(\Delta t^2)$. This suggests formally 2nd-order accuracy for the splitting procedure. Combined with the 2nd-order backward differencing for time discretization, the overall temporal accuracy is 2nd-order.

The consistency in the discrete level can be achieved by following the remarks in Section 2.2. We have implemented the same time discretization scheme to the Phase-Field and momentum conservation equations, and we specify $\tilde{\mathbf{m}}$, unless otherwise specified, as $\tilde{\mathbf{m}}^{DC}$, which is discretized identically to the corresponding terms in the fully-discretized Phase-Field equation Eq.(70) and uses the

numerical chemical potential ξ^* Eq.(61). Since $\mathbf{u}^{*,n+1}$ is a linear combination of $\mathbf{u}^n$ and $\mathbf{u}^{n-1}$, which are discretely divergence-free, $\mathbf{u}^{*,n+1}$ satisfies the discrete divergence-free condition, as well. When $\phi^n, \phi^{n-1} \equiv 1(-1)$, $\phi^{*,n+1} \equiv 1(-1)$, and from Eq.(70) and Eq.(61), it can be shown that $\phi^{n+1} \equiv 1(-1)$, resulting in $\xi^* \equiv 0$. As shown in Section 3.1, by using the discrete Divergence-Gradient-Transpose operator, $\tilde{\nabla}\cdot(\tilde{\mu}^{n+1}(\tilde{\nabla}\tilde{\mathbf{u}}^{*,n+1})^T)$ is zero when μ^{n+1} is constant, because of $\tilde{\nabla}\cdot\mathbf{u}^{*,n+1}=0$. Finally, the *consistency of reduction* is satisfied in the discrete level. In summary, the proposed scheme achieves all the consistency conditions in the discrete level.

The conservations of mass and momentum in the discrete level require that all the terms in the Phase-Field equation Eq.(1) and the momentum conservation equation Eq.(9) are written in their conservative forms and are discretized such that a single-valued numerical flux is defined at each cell face. The same amount of numerical flux moving out from one cell will go to its neighbor. Specifically, if we consider a periodic boundary condition and ignore the source term S_ϕ in Eq. (70), multiply Eq. (70) in cell (i,j) with its volume $[\Delta Vol]_{i,j}$, and then do the summation over all the cells, after some algebraic manipulations, it can be shown that the terms $\sum_{i,j}[\tilde{\nabla}\cdot(\mathbf{u}^{*,n+1}\tilde{\phi}^{*,n+1})]_{i,j}[\Delta Vol]_{i,j}$ and $\sum_{i,j}[M\tilde{\nabla}\cdot(\tilde{\nabla}\xi^*)]_{i,j}[\Delta Vol]_{i,j}$ in Eq. (70) are both zero, based on the definitions of the numerical operators in Section 3.1. As a result, we can obtain $\sum_{i,j}[\frac{\gamma_t\phi^{n+1}-\hat{\phi}}{\Delta t}]_{i,j}[\Delta Vol]_{i,j}=\sum_{i,j}[\frac{\tilde{\partial}\phi}{\tilde{\partial}t}]_{i,j}[\Delta Vol]_{i,j}=0$, i.e., $\sum_{i,j}\phi^{n+1}_{i,j}[\Delta Vol]_{i,j}=\sum_{i,j}\phi^{n}_{i,j}[\Delta Vol]_{i,j}=\cdots=\sum_{i,j}\phi^{0}_{i,j}[\Delta Vol]_{i,j}$, which implies global conservation of the Phase-Field function. Further considering Eq. (5), we can obtain $\sum_{i,j}\rho^{n+1}_{i,j}[\Delta Vol]_{i,j}=\sum_{i,j}\rho^{0}_{i,j}[\Delta Vol]_{i,j}$, which implies global mass conservation. In other words, the global conservations of the Phase-Field function and of the mass are equivalent. The same procedure can be performed on Eq. (71) and again we can obtain that $\sum_{i,j}[\tilde{\nabla}\cdot(\tilde{\mathbf{m}}\otimes\mathbf{u}^{*,n+1})]_{i,j}[\Delta Vol]_{i,j}$, $\sum_{i,j}[\tilde{\nabla}\cdot(\mu^{n+1}\tilde{\nabla}\mathbf{u}^*)]_{i,j}[\Delta Vol]_{i,j}$ and $\sum_{i,j}[\tilde{\nabla}\cdot(\mu^{n+1}(\tilde{\nabla}\mathbf{u}^{*,n+1})^T)]_{i,j}[\Delta Vol]_{i,j}$ are all zero, no matter whether the density and viscosity are constants or not. Consequently, the momentum transport is conserved in the discrete level, i.e., $\sum_{i,j}[\rho^{n+1}\mathbf{u}^{n+1}]_{i,j}[\Delta Vol]_{i,j}=\sum_{i,j}[\rho^{0}\mathbf{u}^{0}]_{i,j}[\Delta Vol]_{i,j}$ if $\frac{\gamma_t\rho^{n+1}\mathbf{u}^{n+1}-\rho\hat{\mathbf{u}}}{\Delta t}+\tilde{\nabla}\cdot(\tilde{\mathbf{m}}\otimes\tilde{\mathbf{u}}^{*,n+1})=0$. The only troublesome term remaining is $\overline{\mathbf{G}^{n+1}}$, which is balanced-force while non-conservative in general. The term $\sum_{i,j}[\rho^{n+1}\overline{\mathbf{G}^{n+1}}]_{i,j}[\Delta Vol]_{i,j}$ is not necessarily zero, even when the surface force and other external momentum sources are ignored. However, it should be noted that, away from the interface, the surface force becomes zero, the density is constant, and $\rho^{n+1}\overline{\mathbf{G}^{n+1}}$ recovers the 2nd-order central difference for the pressure gradient, i.e., $[\rho^{n+1}\overline{\mathbf{G}^{x,n+1}}]_{i,j}=-\frac{\tilde{p}^{n+1}_{i+1/2,j}-\tilde{p}^{n+1}_{i-1/2,j}}{\Delta x_i}$ with $\tilde{p}^{n+1}_{i+1/2,j}=\frac{p^{n+1}_{i+1}+p^{n+1}_{i}}{2}$, which is discretely conservative. As a result, the momentum $[\rho\mathbf{u}]_{i,j}$ is locally conserved in the discrete level in most of the domain except for the location close to the interface, implying that global conservation, i.e., $\sum_{i,j}[\rho^{n+1}\mathbf{u}^{n+1}]_{i,j}[\Delta Vol]_{i,j}=\sum_{i,j}[\rho^{0}\mathbf{u}^{0}]_{i,j}[\Delta Vol]_{i,j}$, can not be guaranteed. However, our numerical experiments in Section 4.1 show that such a non-conservative error is very small even including variable density and surface force.

Another property of the scheme worth discussing is its property of secondary conservation, e.g., kinetic energy conservation, and we restrict our discussion to inviscid cases without surface tension and other momentum sources. We first begin our discussion in the semi-discrete level in the sense that the variables are discrete in space while continuous in time. It can be shown that with the discrete operators defined in Section 3.1 and with the linear interpolation to evaluate $\tilde{\mathbf{u}}$ in $\tilde{\nabla}\cdot(\tilde{\mathbf{m}}\otimes\tilde{\mathbf{u}})$, the identity, $\mathbf{u}\cdot\tilde{\nabla}(\tilde{\mathbf{m}}\otimes\tilde{\mathbf{u}}) = \tilde{\nabla}\cdot(\tilde{\mathbf{m}}\frac{1}{2}\widetilde{\mathbf{u}\cdot\mathbf{u}}) + \frac{1}{2}\mathbf{u}\cdot\mathbf{u}\tilde{\nabla}\cdot\tilde{\mathbf{m}}$, holds, where $[\widetilde{\mathbf{u}\cdot\mathbf{u}}]_{i+1/2,j}$ and $[\widetilde{\mathbf{u}\cdot\mathbf{u}}]_{i,j+1/2}$ are equal to $\mathbf{u}_{i,j}\cdot\mathbf{u}_{i+1,j}$ and $\mathbf{u}_{i,j}\cdot\mathbf{u}_{i,j+1}$, respectively. Using the identities $\mathbf{u}\cdot\frac{\partial(\rho\mathbf{u})}{\partial t} = \frac{\partial(\rho\frac{1}{2}\mathbf{u}\cdot\mathbf{u})}{\partial t} + \frac{1}{2}\mathbf{u}\cdot\mathbf{u}\frac{\partial\rho}{\partial t}$ and $\frac{\partial\rho}{\partial t} + \tilde{\nabla}\cdot\tilde{\mathbf{m}} = 0$, i.e., Eq. (25), we can obtain $\mathbf{u}\cdot[\frac{\partial(\rho\mathbf{u})}{\partial t} + \tilde{\nabla}\cdot(\tilde{\mathbf{m}}\otimes\tilde{\mathbf{u}})] = \frac{\partial(\rho\frac{1}{2}\mathbf{u}\cdot\mathbf{u})}{\partial t} + \tilde{\nabla}\cdot(\tilde{\mathbf{m}}\frac{1}{2}\widetilde{\mathbf{u}\cdot\mathbf{u}})$. This is the semi-discrete counterpart of Eq. (14), where $S_m = 0$. The zero S_m results from achieving consistency in the discrete level of the present scheme. In other words, the discritization of the inertia term in Eq.(71) doesn't introduce any non-conservation error on the kinetic energy in the semi-discrete level if a linear scheme for $\tilde{\mathbf{u}}$ is used. However, even when we ignore the surface force and other momentum sources in $\mathbf{G}$, we are unable to show that the identity, $\rho\mathbf{u}\cdot\overline{\mathbf{G}} = -\rho\mathbf{u}\cdot\overline{[\frac{1}{\rho}\tilde{\nabla}p]} = -\tilde{\nabla}\cdot(\widetilde{\mathbf{u}p})$, holds, where $(\widetilde{\mathbf{u}p})$ means a certain numerical operator applied to $\mathbf{u}$ and p. Numerical experiments have been performed in [44], where a single-phase collocated scheme was analyzed and tested, and the authors discovered that the term $-\mathbf{u}\cdot\overline{[\tilde{\nabla}p]}$ dissipates the kinetic energy. In a two-phase flow problem, the prefactor ρ is not constant any more, which makes the analysis more involved. However, since the prefactor ρ is always positive, it should not change the dissipative property of $-\mathbf{u}\cdot\overline{[\tilde{\nabla}p]}$, and it is reasonable to infer that $-\rho\mathbf{u}\cdot\overline{[\frac{1}{\rho}\tilde{\nabla}p]}$ also dissipates the kinetic energy. Our numerical experiments in Section 4.1 confirmed this point. It is challenging to achieve kinetic energy conservation in the discrete level, especially in multi-phase flow problems. First, all the time and space discretization schemes should be central type so that no numerical dissipation is added. Second, the time discretization scheme should hold the identity $\mathbf{u}\cdot\frac{\partial(\rho\mathbf{u})}{\partial t} = \frac{\partial(\rho\frac{1}{2}\mathbf{u}\cdot\mathbf{u})}{\partial t} + \frac{1}{2}\mathbf{u}\cdot\mathbf{u}\frac{\partial\rho}{\partial t}$ for variable density, which is non-trivial. Third, the inertia term $\tilde{\nabla}\cdot(\tilde{\mathbf{m}}\otimes\tilde{\mathbf{u}})$ may have to be evaluated implicitly, which increases the computational cost. In our case, our scheme in general does not guarantee kinetic energy conservation in the inviscid limit and in the absence of surface force or external momentum sources. In the following numerical implementations, we mainly use the 2nd-order backward difference scheme for time discretization and the WENO scheme for the inertia term, and these two schemes are numerically dissipative. Besides, numerical dissipation is also introduced by the pressure gradient term , based on the numerical tests performed in [44]. We, thus, expect the kinetic energy $\sum_{i,j}\frac{1}{2}\mathbf{u}_{i,j}\cdot\mathbf{u}_{i,j}[\Delta Vol]_{i,j}$ to be numerically dissipated. When the surface forces are present, in addition to the kinetic energy, the free energy of the Phase-Field function has to be incorporated. In the continuous level, the work done by the surface force transfers the free energy to the kinetic energy and as a result, an important property of a Phase-Field model is obtained that the total energy,

including the kinetic energy and the free energy, does not increase with time, even for the inviscid limit [1]. The analysis of the total energy dissipation in the discrete level is non-trivial and we discuss this point using numerical experiments in Section 4.1.

4 Numerical results and discussions

4.1 Validation tests

Five cases are presented to validate the proposed scheme. The first one is the manufactured solution, where the artificially constructed solution is infinitely differentiable. This case is performed to validate that the scheme is formally 2nd-order accurate in both space and time. The second one is the large-density-ratio advection problem, where the significance of achieving consistency in the discrete level is shown. The third one is the horizontal shear layer, where the properties of the scheme on mass and momentum conservations and energy dissipation are validated. The fourth one is the steady drop case, where the performance of the Balanced-Force algorithm is tested by measuring the strength of the spurious current. The fifth case is the rising bubble with large density and viscosity ratios, where the convergence behavior of the Phase-Field model to the sharp interface model is carefully and systematically discussed. Two more cases, which are the reversed single vortex problem [54] and the Zalesak's disk problem [74], are supplemented in the Appendix to validate the Cahn-Hilliard Phase-Field model as an interface capturing method.

In this section, we consider the L_2 error of f to be the root mean square of the pointwise $(f - f_{ref})$ and the L_∞ error of f to be the maximum of the pointwise $|f - f_{ref}|$, where f is the quantity of interest and f_{ref} denotes the reference value of f, unless otherwise specified. We denote the cell size or, equivalently, grid size by h and have $\Delta x = \Delta y = h$.

Manufactured solution We assume that the exact solution of the governing equations has the form

$$\phi_E = \cos(x)\cos(y)\sin(t), \tag{72}$$

$$u_E = \sin(x)\cos(y)\cos(t), \tag{73}$$

$$v_E = -\cos(x)\sin(y)\cos(t), \tag{74}$$

$$p_E = \cos(x)\cos(y)\sin(t). \tag{75}$$

The assumed exact solution is infinitely differentiable with respect to space and time, so it is suitable for the validation of formal order of accuracy. In addition, u_E and v_E satisfy the divergence-free condition. Based on the solution,

we can derive the source term in both the Phase-Field equation Eq.(1) and the momentum equation Eq.(9), i.e.,

$$S_\phi = \frac{\partial \phi_E}{\partial t} + \nabla \cdot (\mathbf{u}_E \phi_E) - \nabla \cdot (M \nabla \xi_E), \tag{76}$$

$$\begin{aligned} \mathbf{S}_\mathbf{u} = \frac{\partial (\rho_E \mathbf{u}_E)}{\partial t} + \nabla \cdot (\mathbf{m}_E \otimes \mathbf{u}_E) + \nabla p_E \\ -\nabla \cdot [\mu_E (\nabla \mathbf{u}_E + (\nabla \mathbf{u}_E)^T)] - \rho_E \mathbf{g} - \xi_E \nabla \phi_E, \end{aligned} \tag{77}$$

where ξ_E, ρ_E, and μ_E are computed from Eq.(2), Eq.(5), and Eq.(6), respectively, with ϕ_E in Eq.(72). We compute $\mathbf{m}_E$ from Eq.(16), the consistent mass flux in the continuous level $\mathbf{m}^{CC}$, with $\mathbf{u}_E$, ϕ_E, and ξ_E.

The parameters in this test are $\rho_1 = 3$, $\rho_2 = 1$, $\mu_1 = 0.02$, $\mu_2 = 0.01$, $\mathbf{g} = \{1, -2\}$, $\lambda = 10^{-3}$, $M = 10^{-3}$, and $\eta = 0.1$. The computational domain is $[-\pi, \pi] \times [-\pi, \pi]$. The free-slip boundary condition is applied to all the boundaries, which is consistent with the exact solution. We use the consistent mass flux in the discrete level $\tilde{\mathbf{m}}^{DC}$ Eq.(27). The initial condition is given based on the exact solution by setting $t = 0$. All the tests are stopped at $t = 1$.

We first test the formal order of accuracy in space by fixing the time step size to be $\Delta t = 10^{-3}$, and by refining the cell size h from $2\pi/8$ to $2\pi/128$ along each axis. The L_2 and L_∞ errors of ϕ, u, v, and p, and their order of convergence are listed in Table 1. The exact solution is used as the reference when we compute the L_2 and L_∞ errors. We observe 2nd-order convergence for both the L_2 and L_∞ errors as expected. In addition, the discrete divergence of velocity $\tilde{\nabla} \cdot \mathbf{u}$ and the discrete Divergence-Gradient-Transpose of velocity $\tilde{\nabla} \cdot (\tilde{\nabla} \tilde{\mathbf{u}})^T$ are listed in Table 2. The discrete divergence-free condition is satisfied to machine precision and because of this, $\tilde{\nabla} \cdot (\tilde{\nabla} \tilde{\mathbf{u}})^T$ reaches the machine zero, as expected. This ensures the *consistency of reduction* of the viscous term in the discrete level.

We next test the temporal convergence by reducing the time step size as fast as the cell size, i.e., $\Delta t = h/(2\pi)$, and by again refining the cell size from $2\pi/8$ to $2\pi/128$ along each axis. The results are listed in Table 3. Since we have validated the 2nd-order accuracy in space, and we have set $\Delta t \sim h$, the overall 2nd-order convergence observed in Table 3 implies 2nd-order convergence of the temporal error, which matches our error estimate in Section 3.4.

We have repeated the above procedures but computing $\mathbf{m}_E$ from the inconsistent mass flux $\mathbf{m}^{IC}$, Eq.(11). Accordingly, the source term $\mathbf{S}_\mathbf{u}$ is derived from Eq.(77), and the discrete inconsistent mass flux $\tilde{\mathbf{m}}^{IC}$, Eq.(23), is used with $\tilde{\rho}$ evaluated by the linear interpolation. We again observe 2nd-order convergence (not shown here). This ensures that all the differences of the results shown in the Large-Density-Ratio advection Section 4.1 are from whether the scheme is consistent.

Large-Density-Ratio advection We first numerically reproduce the analysis in Section 2.2 of one-dimensional advection, which is under the force-free condition. Based on this condition, the governing equations to be solved are simplified,

Table 1: Results of manufactured solution with grid refinement and $\Delta t = 10^{-3}$

Grid	ϕ				u				v				p			
	L_2	L_2 order	L_∞	L_∞ order	L_2	L_2 order	L_∞	L_∞ order	L_2	L_2 order	L_∞	L_∞ order	L_2	L_2 order	L_∞	L_∞ order
8	3.73E-02	1.92	6.33E-02	1.63	2.50E-02	2.04	5.87E-02	1.56	2.65E-02	1.99	6.51E-02	1.54	7.52E-02	0.80	1.59E-01	1.11
16	9.89E-03	1.98	2.05E-02	1.93	6.07E-03	2.01	1.99E-02	1.85	6.67E-03	2.00	2.23E-02	1.84	4.33E-02	1.97	7.36E-02	1.99
32	2.50E-03	1.99	5.37E-03	1.97	1.50E-03	2.01	5.52E-03	1.99	1.67E-03	2.00	6.22E-03	1.95	1.10E-02	2.09	1.86E-02	2.08
64	6.28E-04	2.00	1.37E-03	1.99	3.75E-04	2.00	1.39E-03	2.01	4.16E-04	2.00	1.60E-03	1.99	2.59E-03	2.05	4.41E-03	2.04
128	1.58E-04		3.44E-04		9.34E-05		3.46E-04		1.04E-04		4.05E-04		6.24E-04		1.07E-03	

Table 2: Results of $\tilde{\nabla} \cdot \mathbf{u}$ and $\tilde{\nabla} \cdot (\tilde{\nabla}\tilde{\mathbf{u}})^T$ in manufactured solution

Grid	$\tilde{\nabla} \cdot \boldsymbol{u}$		$\left[\tilde{\nabla} \cdot (\tilde{\nabla}\tilde{\boldsymbol{u}})^T\right]_x$		$\left[\tilde{\nabla} \cdot (\tilde{\nabla}\tilde{\boldsymbol{u}})^T\right]_y$	
	L_2	L_∞	L_2	L_∞	L_2	L_∞
8	4.25E-17	1.67E-16	8.61E-17	2.22E-16	1.07E-16	3.89E-16
16	7.56E-17	5.55E-16	3.48E-16	1.41E-15	3.23E-16	1.72E-15
32	1.28E-16	5.00E-16	1.21E-15	5.88E-15	1.20E-15	5.22E-15
64	2.59E-16	1.11E-15	4.52E-15	2.49E-14	4.52E-15	2.45E-14
128	5.12E-16	2.22E-15	1.85E-14	1.51E-13	1.82E-14	1.26E-13

and will be explained in detail in the upcoming paragraph. Next, we consider the two-dimensional advection, where the force-free condition is removed. Thus, the governing equations without any simplifications are solved, and the surface tension is included. We only consider the consistent mass flux in the discrete level $\tilde{\mathbf{m}}^{DC}$ Eq.(27) and the discrete inconsistent mass flux $\tilde{\mathbf{m}}^{IC}$ Eq.(23) in the following discussions. Whenever $\tilde{\mathbf{m}}^{IC}$ is computed, the linear interpolation is performed to evaluate $\tilde{\rho}$. We consider the density ratio to be 1, 10^3, 10^6, and 10^9.

Following the analysis in Section 2.2, we consider a pure advection case where all the forces on the right-hand side of Eq.(9) are set to zero. The physical solution is that the velocity maintains its initial value u_0 all the time. However, our analysis shows that, numerically, only the consistent mass flux in the discrete

Table 3: Results of manufactured solution with grid refinement and $\Delta t = h/(2\pi)$

Grid	ϕ				u				v				p			
	L_2	L_2 order	L_∞	L_∞ order	L_2	L_2 order	L_∞	L_∞ order	L_2	L_2 order	L_∞	L_∞ order	L_2	L_2 order	L_∞	L_∞ order
8	4.90E-02	1.99	8.29E-02	1.71	2.44E-02	2.29	6.90E-02	1.64	2.62E-02	2.04	6.56E-02	1.51	1.17E-01	1.34	3.15E-01	2.05
16	1.23E-02	2.03	2.54E-02	1.98	4.98E-03	2.01	2.22E-02	1.92	6.36E-03	2.01	2.30E-02	1.81	4.65E-02	1.87	7.59E-02	1.95
32	3.03E-03	2.02	6.42E-03	2.01	1.24E-03	1.98	5.87E-03	1.99	1.58E-03	1.99	6.55E-03	1.94	1.27E-02	2.09	1.96E-02	2.08
64	7.49E-04	2.01	1.59E-03	2.01	3.13E-04	1.98	1.47E-03	2.01	3.97E-04	1.99	1.70E-03	1.98	2.98E-03	2.07	4.64E-03	2.05
128	1.86E-04		3.96E-04		7.92E-05		3.65E-04		9.99E-05		4.32E-04		7.11E-04		1.12E-03	

level $\tilde{\mathbf{m}}^{DC}$ leads to the physical solution. The computational domain is $[0, 1]$ with a periodic boundary condition. A one-dimensional drop is initially located at the center of the domain with diameter $D = 0.5$. Fluid 1, which is inside the drop, is denser than Fluid 2, which is outside the drop. Both the cell-center and cell-face velocities are initially equal to u_0, where u_0 is unity. The cell-face velocity is given to be u_0 instead of being computed during the computation, and we only analyze the error of the cell-center velocity, i.e., $(u - u_0)$. By doing so, the actual equations needed to be solved numerically are Eq.(55) and Eq.(57) for ϕ, and Eq.(62) with zero right-hand side for u, and we let u^* in Eq.(62) to be u^{n+1}. The other parameters are $\eta = 1/32$, $M = 10^{-7}$ and $CFL = u_0\Delta t/h = 0.2$. The computations are stopped at $t = 2$, when the drop returns to its initial location for the second time. The number of cells is in the range 64 to 512. We measure the L_2 and L_∞ errors of u with u_0 as the reference.

The L_2 and L_∞ errors of the cell-center velocity obtained from $\tilde{\mathbf{m}}^{DC}$, labeled as "C", and $\tilde{\mathbf{m}}^{IC}$, labeled as "I", are shown in Fig. 2. The number following "C" or "I" represents the density ratio. The cases of C-1 and I-1 are identical, and their errors are zero so they cannot be seen in the log-log plot.

As expected, the cases using $\tilde{\mathbf{m}}^{DC}$ reproduce the physical results accurately. Both the L_2 and L_∞ errors are below 10^{-6} no matter what the cell size and density ratio are. The errors do not reach the machine zero because of the round-off error of the computer, which will be further explained in the two-dimensional advection problem. In spite of the simplicity of the problem and the idealized numerical implementation, large error is introduced by the inconsistent mass transport when $\tilde{\mathbf{m}}^{IC}$ is used. In addition, the error increases as the density ratio increases. Although the error is reduced as a result of the grid refinement, it is still larger than 10^{-2} for the finest grid. It should be noted that there are about 256 cells across the drop in the finest grid, which is seldom achievable in practical

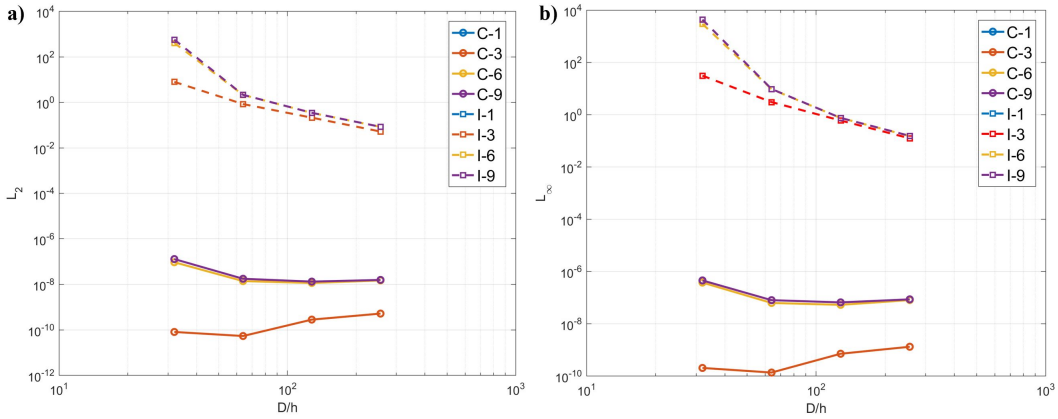

Fig. 2: Results of one-dimensional advection of a drop. a) The L_2 error, and b) the L_∞ error of u.

computations of bubbly flows. These numerical tests not only match the analysis in Section 2.2, but also emphasis the significance of achieving consistency in the discrete level to obtain physical solution in practical computations.

Since only the simplified equations are solved and the cell-face velocity is given in the one-dimensional advection case, the error of the cell-center velocity has no chance to contaminate the cell-face velocity to consequently create unphysical interface distortion and pressure fluctuations. To validate this statement, we perform the two-dimensional advection problem, where the governing equations without any simplifications are solved numerically, following the scheme in Section 3. We consider a circular drop of diameter $D = 0.2$ initially at the center of the domain $[1 \times 1]$, advected by a homogeneous two-dimensional flow, i.e., $u = u_0$ and $v = v_0$. The doubly periodic boundary condition is applied. Both of the fluids are inviscid and the surface tension σ between them is either 10^{-12} or 1. The physical solution is that the velocity field maintains its initial configuration independent of density ratio and surface tension, pressure maintains its reference value, which is zero, everywhere if surface tension is neglected, while it has a jump across the interface in presence of surface tension. The shape of the drop should remain circular without any deformation. The domain is discretized by 128×128 cells. The other parameters are $\eta = 3h$, $M = 10^{-7}$, $u_0 = 1$, $v_0 = 1$, $CFL = u_0 \Delta t/h = 0.1$. All the computations are stopped at $t = 1$, when the drop returns to its initial location for the first time, or before the computation becomes unstable.

Fig. 3 shows the initial drop shape and the streamline. The solution at $t = 1$ should be identical to the initial configuration. Fig. 4 shows the cases without surface tension at $t = 1$ by using either $\tilde{\mathbf{m}}^{DC}$ or $\tilde{\mathbf{m}}^{IC}$. We can obtain stable solution for density ratio 10^9 when using $\tilde{\mathbf{m}}^{DC}$, and the physical solution is well reproduced. The streamlines are parallel to each other along the 45^0 line. The shape of the interface remains a circle and the location of it lays on its initial one. However, 10^3 is the highest density ratio to have stable results when using $\tilde{\mathbf{m}}^{IC}$. Even in that case, although the solution is stable, it is incorrect. The streamlines

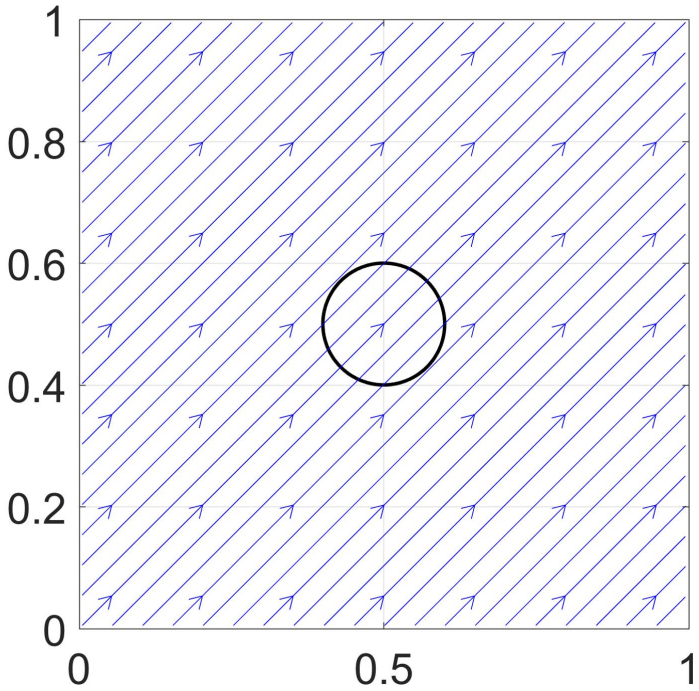

Fig. 3: Initial configuration of two-dimensional advection of a circular drop. Solid black line: Interface at $t = 0$; Blue arrow line: Streamlines at $t = 0$.

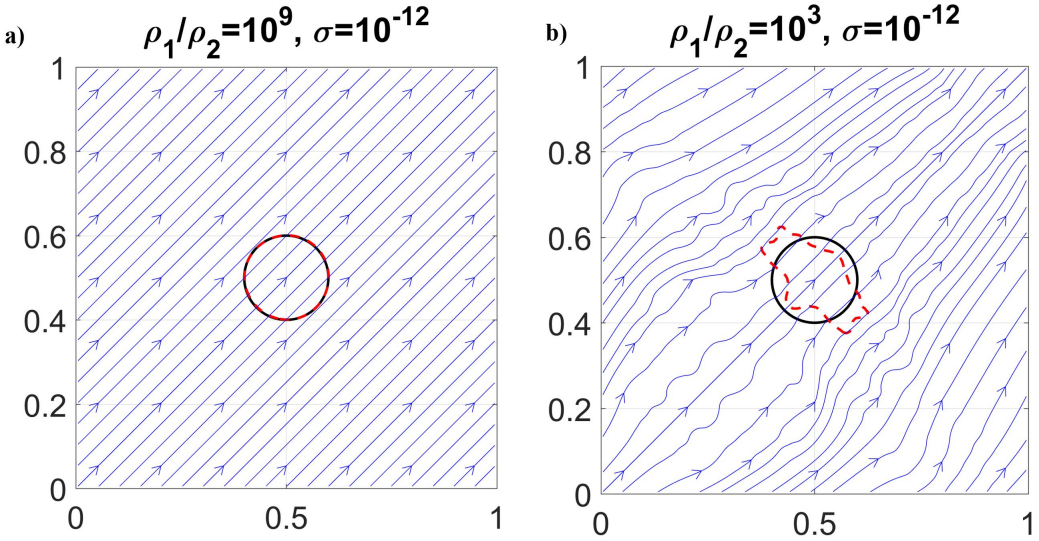

Fig. 4: Results of two-dimensional advection of a circular drop without surface tension. Solid black line: Interface at $t = 0$; Red dash line: Interface at $t = 1$; Blue arrow line: Streamlines at $t = 1$. a) $\tilde{\mathbf{m}} = \tilde{\mathbf{m}}^{DC}$, and b) $\tilde{\mathbf{m}} = \tilde{\mathbf{m}}^{IC}$.

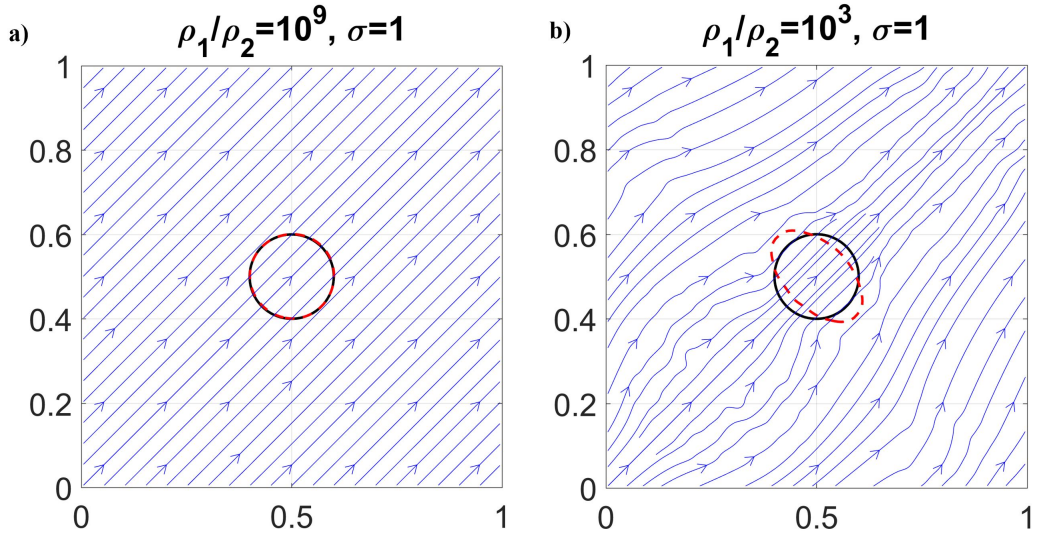

Fig. 5: Results of two-dimensional advection of a circular drop with surface tension. Solid black line: Interface at $t = 0$; Red dash line: Interface at $t = 1$; Blue arrow line: Streamlines at $t = 1$. a) $\tilde{\mathbf{m}} = \tilde{\mathbf{m}}^{DC}$, and b) $\tilde{\mathbf{m}} = \tilde{\mathbf{m}}^{IC}$.

are oscillatory and the shape of the interface is highly deformed by the perturbed velocity, which is unphysical. Fig. 5 shows the results including surface tension. Again, we obtain physical results for density ratio 10^9 by using $\tilde{\mathbf{m}}^{DC}$. Unphysical velocity perturbation and interface deformation is again observed in the case of density ratio 10^3 using $\tilde{\mathbf{m}}^{IC}$. Because of the surface tension, the interface deformation is restricted and it looks like an ellipse.

We measure the L_2 and L_∞ errors of u and v, whose reference values are u_0, and v_0, respectively, to quantify the importance of achieving consistency in the discrete level. In addition, for the cases without surface tension, the L_2 and L_∞ errors of p are measured with its reference value being zero. We define $\overline{\Delta p} = \int_\Omega p d\Omega / \int_\Omega 0.5(1+\phi) d\Omega$ and $(\Delta p)_{\max} = p_{\max} - p_{\min}$ to quantify the pressure jump when there is a surface tension. The label with * represents the result before the computation becomes unstable. Table 4 lists the results without surface tension. We observe that the errors from the cases using $\tilde{\mathbf{m}}^{DC}$ are very small, while it seems proportional to the density ratio. This can be understood by considering that the round-off error introduces an additional inconsistent error. Following the analysis in sections 2.1 and 2.2, we can estimate that its magnitude is on the order of $(\rho_1 - \rho_2)/2$ times the round-off error. When the density ratio is large, the factor $(\rho_1 - \rho_2)/2$ is close to be proportional to the density ratio. We can see that the errors obtained in Table 4 behave similar to our estimation. The errors from the cases using $\tilde{\mathbf{m}}^{IC}$ are very large, compared to those obtained from $\tilde{\mathbf{m}}^{DC}$. The pressure error grows dramatically as the density ratio increases and finally triggers numerical instability. The largest pressure is in front of the interface, where the inconsistent error is most significant. This large pressure value hinders the movement of the interface and results in unphysical interface

Table 4: Results of two-dimensional advection of a circular drop without surface tension

Variable	Density ratio	1		3		6		9	
	Scheme	C	I	C	I	C	I*	C	I*
u	L_2	7.91E-13	7.91E-13	4.84E-11	3.76E-01	2.47E-08	1.51E-01	1.18E-05	2.34E-01
	L_∞	1.21E-11	1.21E-11	1.13E-10	1.77E+00	8.36E-08	4.77E-01	4.92E-05	4.80E-01
v	L_2	7.91E-13	7.91E-13	4.84E-11	3.76E-01	2.47E-08	1.51E-01	1.18E-05	2.34E-01
	L_∞	1.21E-11	1.21E-11	1.12E-10	1.77E+00	8.28E-08	4.77E-01	4.94E-05	4.80E-01
p	L_2	1.60E-12	1.60E-12	7.73E-12	6.24E+00	1.37E-08	7.54E+02	1.64E-05	7.54E+05
	L_∞	1.05E-11	1.05E-11	3.32E-11	1.31E+02	4.60E-08	8.86E+03	5.13E-05	8.86E+06

deformation such that the interface is compressed along its advection direction. Table 5 lists the results including surface tension. The errors of different density ratios for the cases using $\tilde{\mathbf{m}}^{DC}$ slightly change, while they are larger than their correspondence without surface tension. These errors are majorly introduced by the numerical imbalance of the surface tension and the pressure, i.e., the spurious current, instead of the round-off error. The spurious current will be discussed in the steady drop Section 4.1. Both $\overline{\Delta p}$ and $(\Delta p)_{\max}$ have the values close to the pressure jump from the Young−Laplace equation, i.e., $2\sigma/D = 10$ in this case. The errors for the cases using $\tilde{\mathbf{m}}^{IC}$, on the other hand, is majorly introduced by inconsistency instead of numerical imbalance, and they behave similarly to their corresponding ones without surface tension.

Horizontal shear layer The horizontal shear layer in [8,28] and its variations of including variable density, variable viscosity, and surface force are performed to validate the conservations of mass and momentum, and energy dissipation, discussed in Section 3.4. A doubly periodic domain is considered with an initially horizontal shear layer defined as

$$u|_{t=0} = \begin{cases} \tanh(\frac{y-y_1}{\delta_1}), y \leq y_0 \\ \tanh(\frac{y_2-y}{\delta_1}), y > y_0 \end{cases} \tag{78}$$

and a vertical perturbation reads

$$v|_{t=0} = \delta_2 \sin(kx). \tag{79}$$

The initial Phase-Field function $\phi|_{t=0}$ is the same as $u|_{t=0}$ Eq. (78), implying that Fluid 1 is initially at the center of the domain with unperturbed velocity 1, Fluid 2 has -1 velocity next to Fluid 1, and η is $\delta_1/\sqrt{2}$.

Table 5: Results of two-dimensional advection of a circular drop with surface tension

Variable	Density ratio	1		3		6		9	
	Scheme	C	I	C	I	C	I*	C	I*
u	L_2	1.55E-03	1.55E-03	1.08E-03	3.99E-01	1.55E-03	1.50E-01	1.49E-03	2.32E-01
	L_∞	2.00E-02	2.00E-02	1.31E-02	3.52E+00	2.00E-02	4.68E-01	2.17E-02	4.71E-01
v	L_2	1.55E-03	1.55E-03	1.08E-03	3.99E-01	1.55E-03	1.50E-01	1.49E-03	2.32E-01
	L_∞	2.00E-02	2.00E-02	1.31E-02	3.52E+00	2.00E-02	4.68E-01	2.17E-02	4.71E-01
Δp	$\overline{\Delta p}$	9.13E+00	9.13E+00	9.14E+00	-1.64E+01	9.13E+00	2.50E+02	9.25E+00	2.47E+05
	$(\Delta p)_{max}$	1.03E+01	1.03E+01	1.08E+01	7.27E+01	1.03E+01	1.46E+04	1.15E+01	1.46E+07

Table 6: Material properties in different cases of the horizontal shear layer problem

Case ID	ρ_1	ρ_2	μ_1	μ_2	σ
Case 1	1	1	0	0	10^{-12}
Case 2	10	1	0	0	10^{-12}
Case 3	1	1	0.01	0.001	10^{-12}
Case 4	10	1	0.01	0.001	10^{-12}
Case 5	1	1	0	0	0.1
Case 6	10	1	0	0	0.1

The domain has a size of $[1\times1]$ and is discretized by 128 cells in each direction. The parameters in the initial conditions Eqs. (78, 79) are the same as those in [8,28], such that δ_1 is 1/30, δ_2 equals to 0.05 and k takes the value of 2π, and y_0, y_1 and y_2 are 0.5, 0.25 and 0.75, respectively. Six cases are presented and Table 6 lists the material properties of each case.

The first two cases are inviscid and without a surface force. The third and fourth cases are viscous while without a surface force. The last two cases are inviscid but include a surface force. The cases with odd IDs have matched density while the other cases have a density ratio 10. Whenever viscous effects are included, the viscosity ratio is 10. Based on the discussions in Section 3.4, mass is globally conserved in the discrete level, i.e., $\sum_{i,j}\rho_{i,j}(t)[\Delta Vol]_{i,j} = \sum_{i,j}\rho_{i,j}(t=0)[\Delta Vol]_{i,j}$ no matter whether viscous or surface forces are present. With matched density, while without a surface force, e.g., Cases 1 and 3, momentum is globally conserved in the discrete level, i.e., $\sum_{i,j}[\rho\mathbf{u}]_{i,j}(t)[\Delta Vol]_{i,j} = \sum_{i,j}[\rho\mathbf{u}]_{i,j}(t=0)[\Delta Vol]_{i,j}$. However, this is not necessarily true for the rest of the cases. Kinetic energy, in the continuous level, is conserved in Cases 1 and 2. However, because of numerical dissipation, kinetic energy in the discrete level, $E_K(t) = \sum_{i,j}\frac{1}{2}[\mathbf{u}\cdot\mathbf{u}]_{i,j}(t)[\Delta Vol]_{i,j}$, should be decreased, i.e., $E_K(t) \leq E_K(t=0)$. In the presence of a surface force, e.g., Cases 5 and 6, there is energy transfer

between kinetic energy and free energy and the total energy, which is the sum of the kinetic energy and the free energy, does not increase in the continuous level even when the flow is inviscid [1]. The discrete form of energy should be able to reproduce this property, i.e., $E_K(t) + E_F(t) \leq E_K(t=0) + E_F(t=0)$, where $E_F(t)$ is defined as

$$E_F(t) = \sum_{i,j} \lambda \left[F(\phi_{i,j}) + \frac{1}{2} \left((\frac{\phi_{i+1,j} - \phi_{i,j}}{\Delta x})^2 + (\frac{\phi_{i,j+1} - \phi_{i,j}}{\Delta y})^2 \right) \right] (t) [\Delta Vol]_{i,j}.$$

As shown in Fig. 6, we first consider, the results of cases 1-4, where there is no surface force and the free energy is zero. Fig. 6 a) shows the change of mass in the domain. The cases 1-4 conserve mass in the discrete level, no matter whether viscous effects are considered. Fig. 6 c) and d) show the change of momentum in x and y directions, respectively. For matched density cases, i.e., cases 1 and 3, the momentum is conserved in the discrete level, while cases 2 and 4 with density ratio 10 are not conserved. Comparing to the initial value of the momentum in cases 2 and 4, which are 3.9 in the x direction and 0 in the y direction, the change of momentum in these two cases are on the order of 10^{-13} in the x and 10^{-15} in the y directions, which are extremely small. Fig. 6 b) shows the time history of the change of kinetic energy. Cases 1 and 2 don't include physical viscosity, and as a result the kinetic energies in these two cases are almost unchanged, compared to those in cases 3 and 4, where physical viscosity is included. The inset plot shows that the kinetic energies in cases 1 and 2 decay although these two cases are inviscid. To further confirm that the decay of kinetic energy is caused by numerical dissipation, we include finer-grid solutions of cases 2 and 4. Numerical dissipation should be reduced after grid refinement while physical dissipation should not be changed. As we use half the grid size, the change of kinetic energy in case 2 (inviscid case) is reduced from 0.1166% to 0.0223%. Opposite to that, there is no observable difference in case 4 (viscous case) after refining the grid, indicating that the kinetic energy is dissipated dominantly by physical viscosity in this case.

We next consider cases 1,2,5, and 6, where cases 5 and 6 include a surface force and cases 1 and 2 are without a surface force. Mass is again conserved in the discrete level, as shown in Fig. 7, a), even when the surface force is included. Fig. 7 c) and d) show the change of momentum. Case 6, where the densities are not matched and there is a surface force, has the most noticeable momentum reduction in the x direction. However, when compared to its initial momentum value in the x direction 3.9, the reduction is only 0.0058%, which is still insignificant. Since there is a surface force in this case, the free energy appears and Fig. 7 b) shows the time histories of kinetic energy, free energy and total energy of case 5. We observe that the decrease of kinetic energy corresponds to the increase of free energy. However, the total energy, which is the sum of them, decays, and this can be observed more clearly in the inset plot. The same behavior is obtained in case 6 (not shown). It should be noted that, although cases 5 and 6 are inviscid, the total energy decay doesn't result from numerical dissipation but is actually the property of the Phase-Field model [1]. To confirm this, results for the finer grid is included, which is almost on top of that of the default grid.

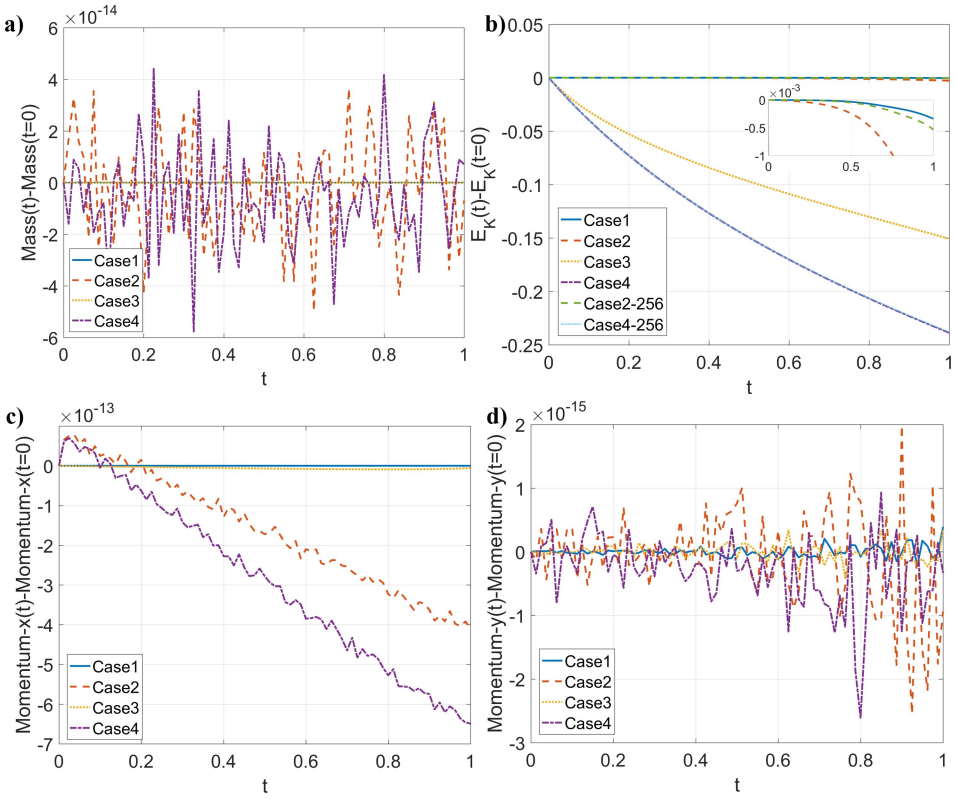

Fig. 6: Results of horizontal shear layer in Cases 1-4. **a)** Change of mass, **b)** change of kinetic energy, **c)** change of momentum-x, and **d)** change of momentum-y with respect to time.

The results shown in this section validate our analysis and discussion about mass and momentum conservations and energy dissipation in Section 3.4. The mass is globally conserved in the discrete level and this is independent of the presence of viscosity or surface forces. The momentum is globally conserved in the discrete level in the case with matched density and without surface forces. Although global conservation of momentum in the discrete level is not guaranteed in general because of the term $\rho^{n+1}\overline{\mathbf{G}^{n+1}}$ in Eq. (71), our numerical experiments show that the contribution of the non-conservative term is small and because of that, we claim that the proposed scheme is essentially conservative. The energy transfer between kinetic energy and free energy is well captured by the scheme and the total energy is dissipated either by the intrinsic physical dissipation of the Phase-Field model, or by numerical dissipation, which is usually very small compared to the physical one.

Steady drop A circular drop is initially at the center of the domain, and the velocity is zero everywhere. The physical solution is that the pressure gradient exactly balances the surface tension at the interface so the velocity remains zero

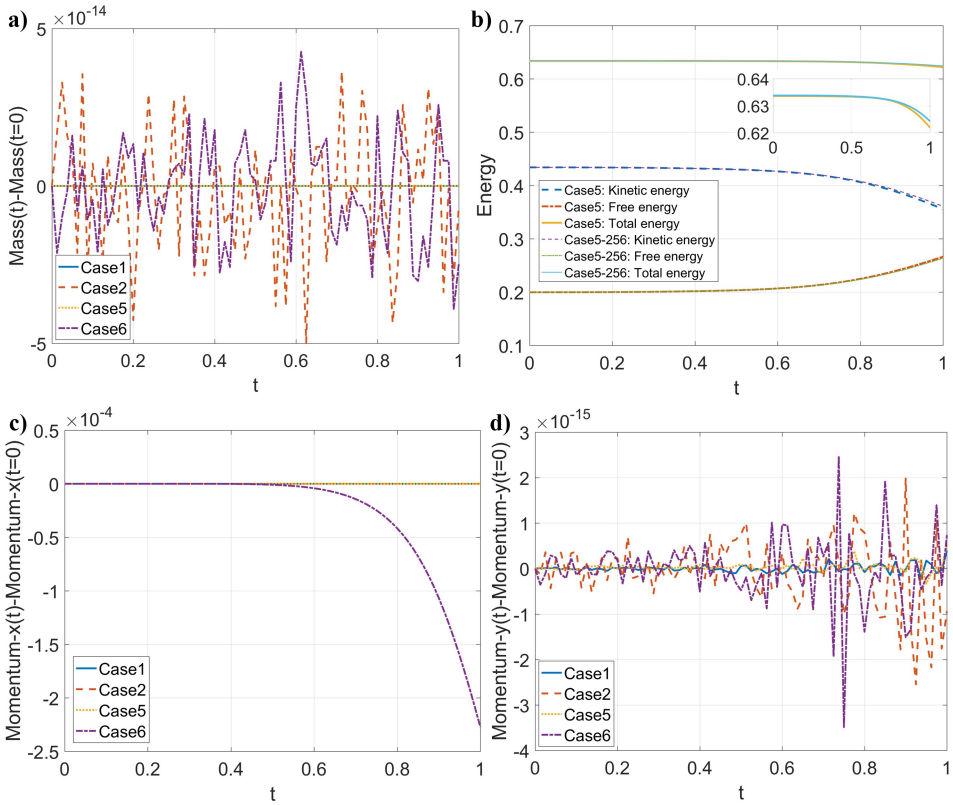

Fig. 7: Results of horizontal shear layer in Cases 1,2,5,6. **a)** Change of mass, **b)** energy, **c)** change of momentum-x, and **d)** change of momentum-y with respect to time.

forever and the interface neither moves or deforms. However, the exact balance in the physical configuration is numerically unachievable and this numerical imbalance drives the flow to move, generating the spurious current, which is unphysical. We will test the performance of the Balanced-Force algorithm in Section 3.2 and quantify the strength of the spurious current.

The domain size is $[1 \times 1]$ and is discretized by cells in the size range $1/16$ to $1/128$ along each axis. The diameter of the drop is $D = 0.4$. The free-slip boundary condition is applied to all the boundaries. The velocity and pressure are set to be initially zero. The time step size Δt is 10^{-3} and all the simulations are stopped at $t = 10$. We consider, in this case, $\eta = \eta_0(h/h_0)^{2/3}$ and $M = M_0(\eta/\eta_0)^{3/2}$, where both η_0 and h_0 are $1/32$, and M_0 is 10^{-7}. The detailed discussion about the effects of η and M on the convergence behavior is provided in Section 4.1. The fluid inside the drop is referred to as Fluid 1 with density ρ_1 and viscosity μ_1, while the one outside the drop is named Fluid 2 with density ρ_2 and viscosity μ_2. We consider the effects of density ratio, viscosity ratio and surface tension, and their convergence behavior under grid refinement. Six cases are considered, whose material properties are listed in Table 7. Case 0 is a

Table 7: Material properties in different cases of steady drop

Case ID	ρ_1	ρ_2	μ_1	μ_2	σ
Case 0	1000	1000	0	0	10^{-12}
Case 1	1000	1000	0	0	1
Case 2	1000	1000	0.1	0.1	1
Case 3	1000	1	0.1	0.1	1
Case 4	1000	1000	0.1	0.0001	1
Case 5	1000	1000	0.1	0.1	10

numerical check, such that we obtain zero when the input is zero. By comparing cases 3,4,5 to case 2 respectively, we quantify the effects of density ratio, viscosity ratio, and surface tension. By comparing case 1 to case 2 we quantify the effect of viscosity. We use the magnitude of the velocity, i.e., $V = \sqrt{u^2 + v^2}$, as the local strength of the spurious current and then we compute the L_2 and L_∞ of V with reference value zero, for all the cases. For clear presentation, the results of case 0 are not shown. Both the L_2 and L_∞ of V in case 0 are on the order of 10^{-14} for all the cell sizes considered.

The results of case 1 to 5 are shown in Fig.8. We can see that the spurious current decreases in all the cases as a result of grid refinement, with the convergent rate in between 1st and 2nd order. Case 5, which has the largest surface tension, produces the largest spurious current, while converges slower at the rate very close to 1st order. Case 1, which is the inviscid case, has the second largest spurious current, while converges faster at the rate close to 2nd order. This implies that the physical viscosity helps to suppress the spurious current. The large viscosity ratio (Case 4) slightly increases the strength of the spurious current, while the effect of large density ratio (Case 3) is very small. Interestingly, we obtain the smallest spurious current in Case 3, which includes a large density ratio. In general, our tests show that the strengths of the spurious current in cases 1 to 5 are on the same order of magnitude.

Rising bubble: convergence tests We consider the convergence behavior of the present scheme in a realistic two-phase flow problem, which includes large density and viscosity ratios, surface tension, and gravity. Since the Phase-Field model approximates the sharp interface model asymptotically with $O(\eta)$, due to grid refinement and by fixing η, the numerical solution converges to the exact solution with interface thickness $O(\eta)$, but not to the sharp interface solution. In order to converge to the sharp interface solution, which is desired, the parameter η must reduce with grid size. In practice, the convergence rate of the numerical solution from the Phase-Field model to the sharp interface solution with grid refinement is important. Such a discussion in the Phase-Field community focuses only on the matched density case, and we have not yet seen any careful and systematic discussions on the problem of large density and viscosity ratios,

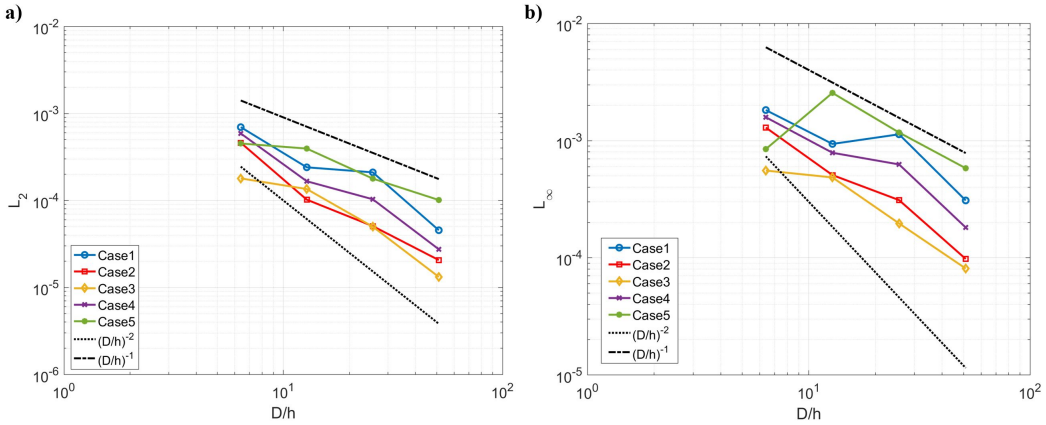

Fig. 8: Results of the steady drop. a) The L_2 error, and b) the L_∞ error of V.

although it is a common situation in two-phase flows. This section focuses on addressing this gap in the literature.

We consider the rising bubble case. The domain is $[1 \times 2]$ and is discretized by the cell sizes ranging from 1/16 to 1/256. The no-slip boundary condition is applied at the top and bottom walls while the free slip boundary condition is assigned at the left and right walls. A bubble of diameter 0.5 is initially at $(0.5, 0.5)$ and the velocity is zero. The density and viscosity of Fluid 1 inside the bubble are 1 and 0.1, respectively, while they are 1000 and 10 for Fluid 2 outside the bubble. These lead to a density ratio 1000 and viscosity ratio 100. The surface tension is 1.96 and gravitational acceleration is $\mathbf{g} = \{0, -0.98\}$. The time step size is $\Delta t = 0.128h$ and all the computations are stopped at $t = 1$. We use three benchmark quantities: the circularity ψ_c, the center of mass y_c and the rising velocity v_c to quantify our results, and their definitions are as follows:

$$\psi_c = \frac{P_a}{P_b} = \frac{2\sqrt{\int_{\phi>0} \pi d\Omega}}{P_b}, \tag{80}$$

$$y_c = \frac{\int_\Omega y \frac{1+\phi}{2} d\Omega}{\int_\Omega \frac{1+\phi}{2} d\Omega}, \tag{81}$$

$$v_c = \frac{\int_\Omega v \frac{1+\phi}{2} d\Omega}{\int_\Omega \frac{1+\phi}{2} d\Omega}, \tag{82}$$

where P_a is the perimeter of the circle whose area is identical to the bubble, and P_b is the perimeter of the bubble. The circularity ψ_c quantifies the shape of the bubble. It is 1 when the bubble is a circle, and less than 1 when the bubble deforms. The center of mass y_c and rising velocity v_c quantify the dynamics of the bubble. The sharp interface solution under the same set-up are available in [29], where either the Level-Set or Arbitrary-Lagrange-Euler method is used and excellent agreement is reached in the time zone considered. The same benchmark quantities are defined for the sharp interface method and they are considered as

the reference. If the benchmark quantities at time t are not directly available, the cubic spline interpolation is used to specify them.

We relate η to the cell size h as $\eta = \eta_0(h/h_0)^{\chi_\eta}$ and relate the mobility M to η as $M = M_0(\eta/\eta_0)^{\chi_M}$, where $\eta_0 = h_0 = 1/32$ and $M_0 = 10^{-7}$. The exponent χ_η should be less than or equal to 1 so that at least there are the same number of grid points across the interface during grid refinement. The exponent χ_M should be larger than or equal to 1 but smaller than 2, based on the analysis from Jacqmin [30]. We first consider the effect of χ_η on the convergence rate by fixing $\chi_M = 1$ and by choosing χ_η to be 0, 1/3, 1/2, 2/3, and 1. The results are shown in Fig.9-Fig.13. When $\chi_\eta = 0$, the interface thickness η doesn't change during grid refinement, we can see that the numerical solutions quickly converge to the exact solution of the Phase-Field model with parameters $\eta = \eta_0$ and $M = M_0$. Since the interface thickness η is not reduced, the numerical solutions are unable to converge to the sharp interface solution. When χ_η is larger than zero, we can see that all the numerical solutions converge to the sharp interface solution during grid refinement. However, the convergence rate is different for different χ_η. For example, the discrepancy between the numerical solution of $\chi_\eta = 1/3$ and the sharp interface solution is very obvious even with the finest grid ($h = 1/256$), while the numerical solution of $\chi_\eta = 1$ with the grid size ($h = 1/128$) is almost on top of the sharp interface solution. To quantify the convergence rate, we measure the L_2 error of the benchmark quantities, which are listed in Table 8. For the case where $\chi_\eta = 0$, since the numerical solution does not converge to the sharp interface solution, it does not make sense to use that as the reference to compute the L_2 error. As convergence can be observed, we use the finest-grid solution as the reference instead for this case. For the other cases where $\chi_\eta > 0$, we use the sharp interface solution in [29] as the reference solution when computing the L_2 error. However, it should be noted that the reference solution is still a numerical approximation of the exact sharp interface solution. The computed L_2 error includes the error of our Phase-Field solution and the error of the reference solution. The error of the reference solution is negligible, compared to the error of our Phase-Field solution, when the grid is coarse. However, it becomes more significant as our Phase-Field solution gets closer to the exact sharp interface solution during grid refinement, and, as a result, interferes the evaluation of the convergence rate. Consequently, we skip the finest-grid results when evaluating the convergence rate. We observe that the convergence rate is better than 2nd-order when η is fixed and is close to 0.6, 0.9, 1.2 and 1.5 when χ_η is 1/3, 1/2, 2/3, and 1, respectively. Next we consider the case where $\chi_\eta = 2/3$ and $\chi_M = 3/2$, which leads to $M \sim h$. The results are given in Fig. 14 and the convergence rates are listed in Table 8, as well. We observe the convergence to the sharp interface solution in Fig. 14 and both the errors and the convergence rates have little change, compared to the corresponding one with $\chi_M = 1$. This implies that the effect of χ_M on the numerical solution is small.

For all the cases that have been discussed, no matter how we choose χ_η, the magnitude of η is still on the same order of the grid size h, and our numerical

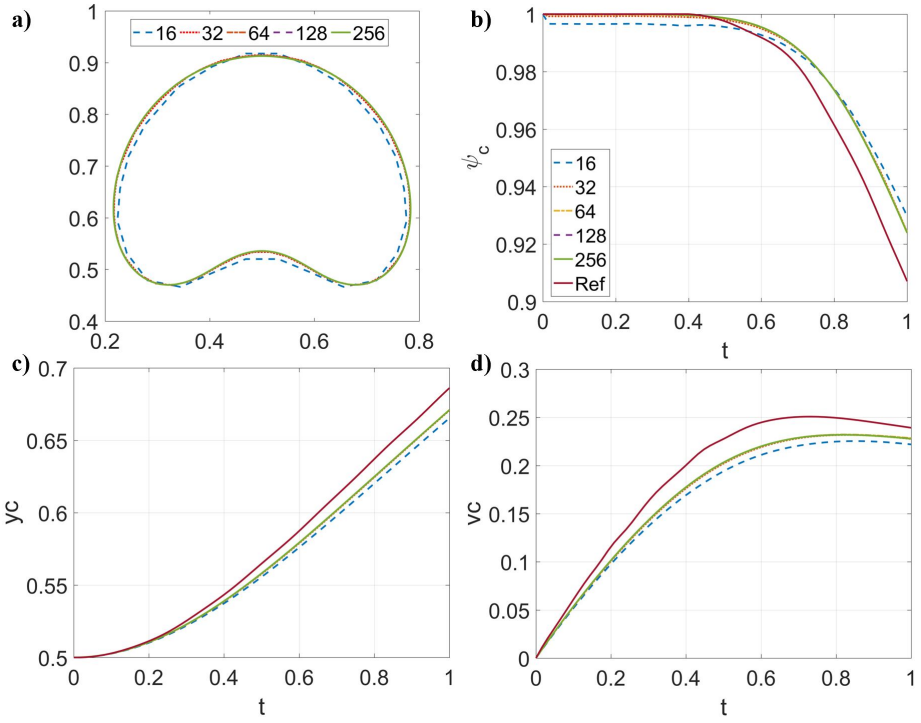

Fig. 9: Results of the rising bubble with $\chi_\eta = 0$ and $\chi_M = 1$. a) The shape of the bubble at $t = 1$, b) the circularity ψ_c vs. t, c) the center of mass y_c vs. t, and d) the rising velocity v_c vs. t.

Table 8: Results of rising bubble: convergence tests

	Grid	$\chi_\eta = 0, \chi_M = 1$		$\chi_\eta = \frac{1}{3}, \chi_M = 1$		$\chi_\eta = \frac{1}{2}, \chi_M = 1$		$\chi_\eta = \frac{2}{3}, \chi_M = 1$		$\chi_\eta = \frac{2}{3}, \chi_M = \frac{3}{2}$		$\chi_\eta = 1, \chi_M = 1$	
		L_2	Order	L_2	Order	L_2	Order	L_2	Order	L_2	Order	L_2	Order
ψ_c	16	3.09E-03	2.36	1.17E-02	0.61	1.34E-02	0.81	1.52E-02	1.00	1.52E-02	1.00	1.93E-02	1.34
	32	6.02E-04	2.06	7.65E-03	0.61	7.65E-03	0.92	7.65E-03	1.25	7.65E-03	1.25	7.65E-03	1.97
	64	1.45E-04	2.54	5.02E-03	0.62	4.04E-03	0.89	3.22E-03	1.11	3.22E-03	1.11	1.95E-03	1.73
	128	2.49E-05		3.28E-03		2.19E-03		1.49E-03		1.49E-03		5.87E-04	
		L_2	Order	L_2	Order	L_2	Order	L_2	Order	L_2	Order	L_2	Order
y_c	16	3.20E-03	3.27	1.53E-02	0.75	1.77E-02	0.96	2.07E-02	1.19	2.07E-02	1.19	2.84E-02	1.64
	32	3.30E-04	2.50	9.09E-03	0.63	9.09E-03	0.93	9.09E-03	1.23	9.09E-03	1.23	9.09E-03	1.82
	64	5.86E-05	2.26	5.86E-03	0.58	4.77E-03	0.85	3.88E-03	1.12	3.88E-03	1.12	2.58E-03	1.61
	128	1.22E-05		3.92E-03		2.64E-03		1.78E-03		1.79E-03		8.47E-04	
		L_2	Order	L_2	Order	L_2	Order	L_2	Order	L_2	Order	L_2	Order
v_c	16	6.77E-03	3.07	3.14E-02	0.71	3.59E-02	0.91	4.15E-02	1.11	4.15E-02	1.11	5.62E-02	1.55
	32	8.05E-04	1.77	1.91E-02	0.58	1.91E-02	0.83	1.91E-02	1.07	1.91E-02	1.07	1.91E-02	1.52
	64	2.37E-04	2.43	1.29E-02	0.48	1.08E-02	0.67	9.12E-03	0.84	9.12E-03	0.84	6.67E-03	1.11
	128	4.39E-05		9.23E-03		6.78E-03		5.09E-03		5.09E-03		3.08E-03	

practice shows this is a good choice for η. However, the magnitude of the mobility depends on M_0 while there is no clear guideline to specify that. To figure out the effect of M_0, we perform a series numerical experiments by fixing $\chi_\eta = 1$, $\chi_M = 1$, $h = 1/128$ and choosing M_0 from 10^{-4} to 10^{-9}. The results are shown in Fig. 15. We observe that there is little difference between the cases with different

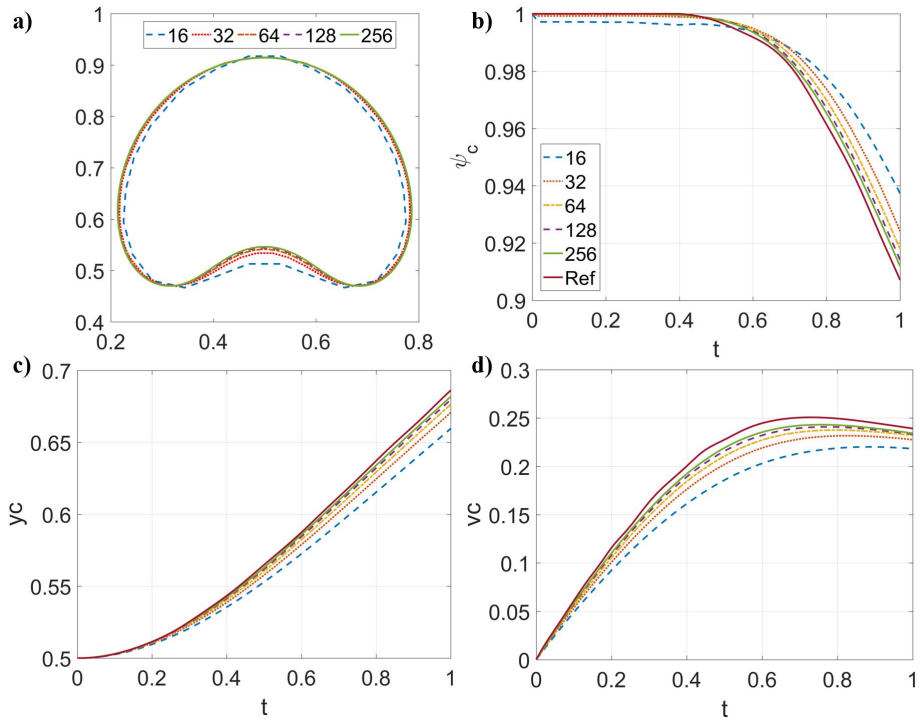

Fig. 10: Results of the rising bubble with $\chi_\eta = 1/3$ and $\chi_M = 1$. a) The shape of the bubble at $t = 1$, b) the circularity ψ_c vs. t, c) the center of mass y_c vs. t, and d) the rising velocity v_c vs. t.

M_0, and all the cases in Fig. 15 are almost on top of the sharp interface solution. This implies that the numerical solution is strongly tolerant to the magnitude of M. This also explain why the effect of χ_M on the numerical solution is small.

4.2 Verifications and applications

Three two-phase flow cases are presented to verify the proposed scheme and to show its capability and possible applications. The first one is the Rayleigh-Taylor instability, which includes complicated interface evolution. We first verify our results by comparing them to both the sharp interface and Phase-Field solutions of density ratio 3, i.e., the Atwood number $At = (\rho_h - \rho_l)/(\rho_h + \rho_l) = 0.5$, where ρ_h is the density of the heavier fluid and ρ_l is that of the lighter one. Next we show the cases with density ratio 30, 1000, and 3000. Finally, we present the long-time dynamics of the case with $At = 0.5$. The second one is the dam break case, which includes a large density ratio. We verify our scheme by comparing our result to the experimental data from the water-air interface, and next we show the result of density ratio 100,000. At the end of this case, we present the long-time dynamics of the water-air interface. The final one is the rising bubble with moving contact lines, which includes both large density ratio and

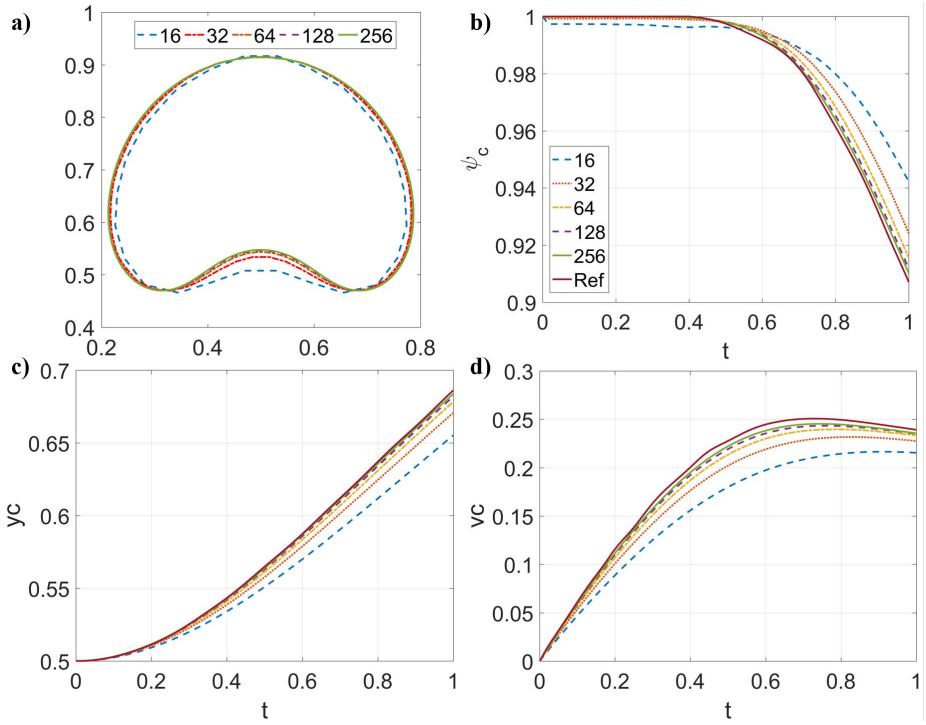

Fig. 11: Results of the rising bubble with $\chi_\eta = 1/2$ and $\chi_M = 1$. a) The shape of the bubble at $t = 1$, b) the circularity ψ_c vs. t, c) the center of mass y_c vs. t, and d) the rising velocity v_c vs. t.

the effect of steady contact angle. Unless otherwise specified, we use $\eta = 0.01$ and $(\lambda M) = 10^{-7}$ in all the cases in this section.

Rayleigh-Taylor instability The Rayleigh-Taylor instability is considered as a benchmark problem for two-phase flows. A heavier fluid (Fluid 1) is initially on the top of a lighter one (Fluid 2). These two fluids are separated by a horizontal interface. The interface is unconditionally unstable after it is perturbed. During the penetration of the fluids, complex interface dynamics is observed due to the appearance of small-scale flow patterns. The domain considered is $[1 \times 4]$ with the free-slip boundary condition at the top and bottom of the domain while the periodic boundary condition is imposed at the two lateral boundaries. The domain is discretized by 128×512 cells, and the time step size Δt is $5 \times 10^{-4}/\sqrt{At}$. The material properties are $\rho_1 = 3$, $\rho_2 = 1$, $\mu_1 = \mu_2 = 0.001$, $\sigma = 10^{-12}$, and $\lambda M = 10^{-15}$. The gravitational acceleration $\mathbf{g}$ points downwards and its magnitude is unity, i.e., $\mathbf{g} = \{0, -1\}$. The initial horizontal perturbation is modeled by a sinusoidal wave at $y = 2$, whose amplitude is 0.1 and wavelength is 2π, and the initial velocity is zero.

We compare our result to those by Ding et al. [17], Guermond and Quartapelle [25], and Tryggvason [63] for verification. The viscosities of the fluids are

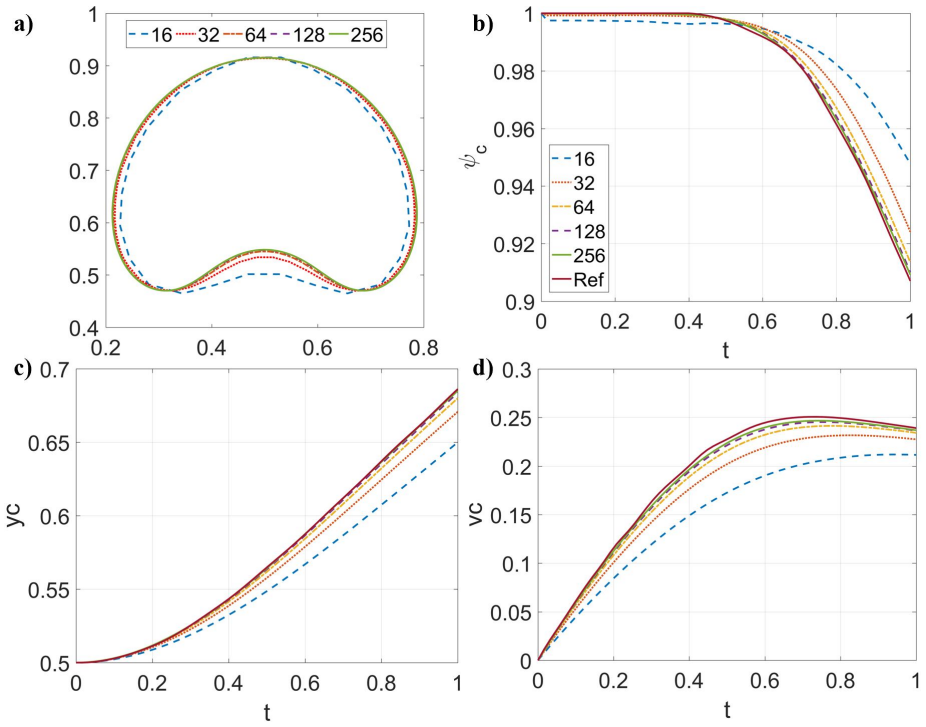

Fig. 12: Results of the rising bubble with $\chi_\eta = 2/3$ and $\chi_M = 1$. a) The shape of the bubble at $t = 1$, b) the circularity ψ_c vs. t, c) the center of mass y_c vs. t, and d) the rising velocity v_c vs. t.

identical to those in [17,25], while the flow considered in [63] is inviscid. Quantitative comparison can be achieved by measuring the transient locations of the interface at the center and at the lateral edge of the domain, as shown in Fig. 16. Our result is almost on top of the published one. The snapshots of the interface at different times are compared against those in [17] in Fig. 17. Both the interface structure and its temporal evolution agree very well with those in [17]. In addition, larger density ratios, i.e., 30,1000, and 3000, are explored, whose results are shown in Fig. 18. As density ratio increases, the interface moves faster while its evolution is simpler. In addition, the results of density ratio 1000 and 3000 are almost identical since the Atwood numbers in these two cases are very close to unity. The long-time dynamics of the Rayleigh-Taylor instability with $At = 0.5$ (density ratio 3) is shown in Fig. 19, where very complicated interface evolution can be observed. The mainstream in the middle of the domain is moving downward, transporting the heavier fluid from top to bottom. When the heavier fluid reaches the bottom wall, it spreads towards the lateral walls and then moves upward along them. The flow in the middle and in the side of the domain are in the opposite direction and it further triggers instability, and the expansion and contraction of the middle fluid column can be observed. As the instability grows, it interacts with other flow structures or generates small droplets and filaments, resulting in a sophisticated interface pattern. Despite the complicated interface

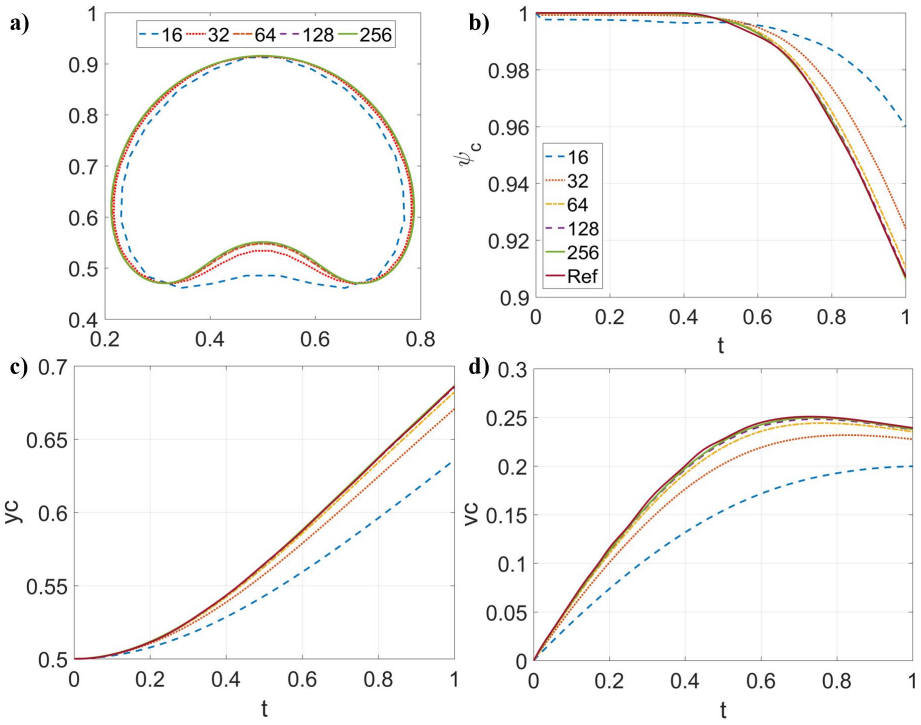

Fig. 13: Results of the rising bubble with $\chi_\eta = 1$ and $\chi_M = 1$. a) The shape of the bubble at $t = 1$, b) the circularity ψ_c vs. t, c) the center of mass y_c vs. t, and d) the rising velocity v_c vs. t.

evolution, the numerical solution maintains symmetry. Since the viscous effects, in this case, is small, the problem reaches equilibrium after a very long time which is outside our simulation time.

Dam break We perform the Dam break case to verify our scheme for a large-density-ratio problem, by comparing our numerical result to the experimental measurements by Martin and Moyce [43].

In the experiment, a water column, which is initially stationary, collapses due to gravity, after the holding is removed. Martin and Moyce [43] measured the locations of the front and the height of the water column at different instants, and scaled them with the initial width of the water column a. The scaled locations of the front and the height are denoted by Z and H, respectively. The computational domain is $[4a \times 2a]$ and is discretized by 256×128 cells. No-slip/penetration boundary condition is applied at all the boundaries. A square of water column initially is in $[0, a] \times [0, a]$ of the domain, with $a = 2.25$ inch, i.e., 5.715cm, and is surrounded by air.

The material properties of water and air are:

- Air: $\rho_{air} = 1.204$ kg/m^3, $\mu_{air} = 1.78 \times 10^{-5}$kg/(m $\cdot$ s)
- Water: $\rho_{water} = 998.207$kg/m^3, $\mu_{water} = 1.002 \times 10^{-3}$ kg/(m $\cdot$ s)

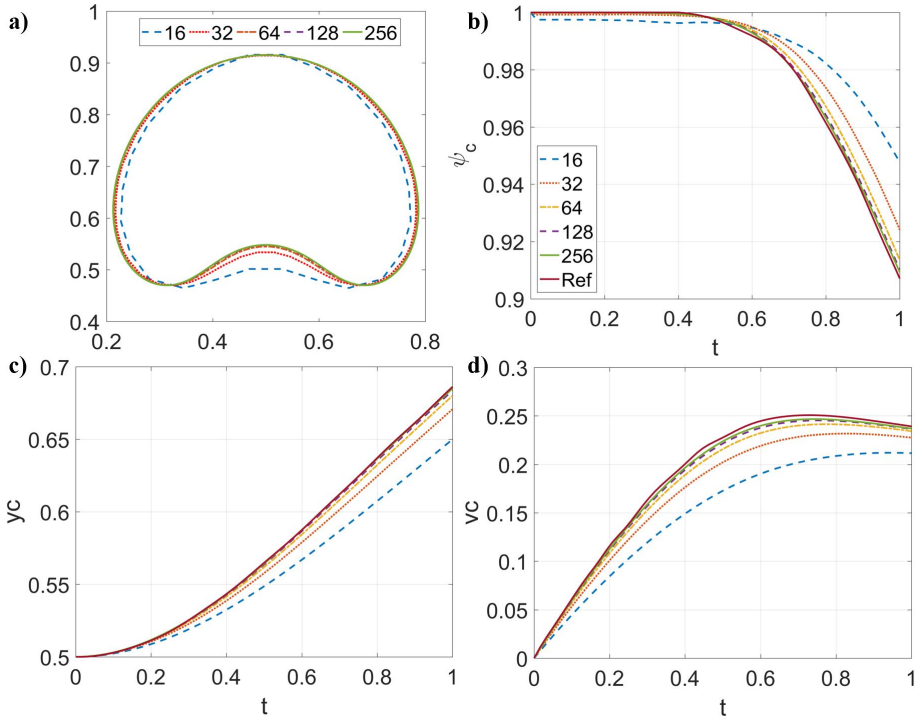

Fig. 14: Results of the rising bubble with $\chi_\eta = 2/3$ and $\chi_M = 3/2$. a) The shape of the bubble at $t = 1$, b) the circularity ψ_c vs. t, c) the center of mass y_c vs. t, and d) the rising velocity v_c vs. t.

- Surface tension: $\sigma = 7.28 \times 10^{-2}$ kg/s^2
- Gravitational acceleration: $g_x = 0$m/s^2, $g_y = -9.8$ m/s^2.

In this case, the water is labeled as Fluid 1 and the air is labeled as Fluid 2. The density ratio is about 830 while the viscosity ratio is about 56. We non-dimensionalize the equations by using the density scale ρ_{air}, the length scale a, and the time scale $\sqrt{a/|g_y|}$. We follow the same calibration in [43] that $Z = 1.44$ when $T = 0.8$ and $H = 1$ when $T = 0$, where T is the non-dimensionalized time. Quantitative comparisons of our numerical results to the experimental results in [43] are shown in Fig. 20. Both the evolutions of the front and the height of the interface obtained from our scheme agree with the measurements very well at all times. In addition, the case of density ratio 100,000 is performed for the same set up to test the capability of the represent scheme dealing with extremely large density ratios. The evolution of the front and the height from this case are also plotted in Fig. 20, from where we can see that the interface moves a little faster than the one for the water-air case. The snapshots of the interfaces for both cases are shown in Fig. 21. The long-time dynamics of the water-air case is included in Fig. 22 and we can observe the complicated interface evolution. The water is pushed to rise on the vertical wall at the right of the domain. Because of gravity, the rising motion on the wall is slowed down and the water on the

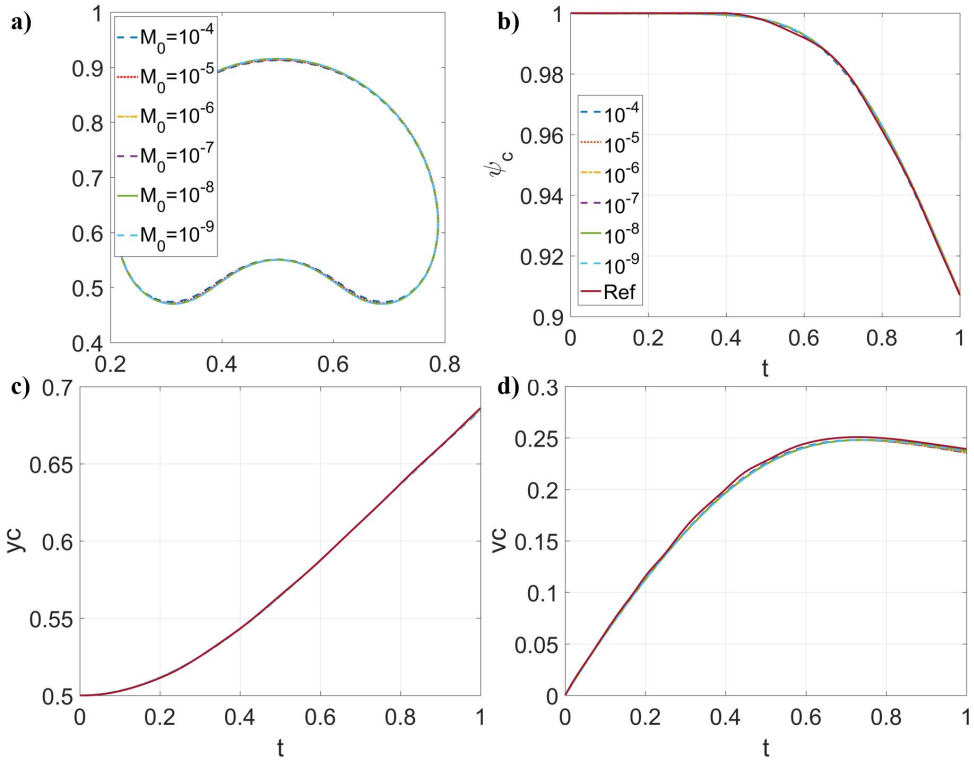

Fig. 15: Results of the rising bubble with different M_0. a) The shape of the bubble at $t = 1$, b) the circularity ψ_c vs. t, c) the center of mass y_c vs. t, and d) the rising velocity v_c vs. t.

vertical wall tends to move backward. However, the water at the bottom is still moving from left to right because of inertia, and as a result, a bump of water appears on the vertical wall. This bump grows, and finally collapse with the water at the bottom. After that, a hydraulic jump is generated, moving from right to left, along with small filaments and droplets. This hydraulic jump hits the left vertical wall and then the water is pushed to move again to the right.

Rising bubble with moving contact lines This final case includes a large density ratio, gravity, surface tension force, and moving contact lines, which is challenging in two-phase flows. An air bubble is released inside a closed water tank. Because of the buoyancy effect, the bubble moves upward and at the same time it deforms. A contact line between the water, air, and the top wall appears after the bubble touches the top wall. The contact line slides along the top wall with the oscillation of the bubble. As a result, the bubble may touch the lateral walls.

The material properties of water and air are identical to those in the Dam break case. We refer to air as Fluid 1 and water as Fluid 2. We non-dimensionalize the equations with the density scale ρ_{air}, length scale 0.01m, and the gravita-

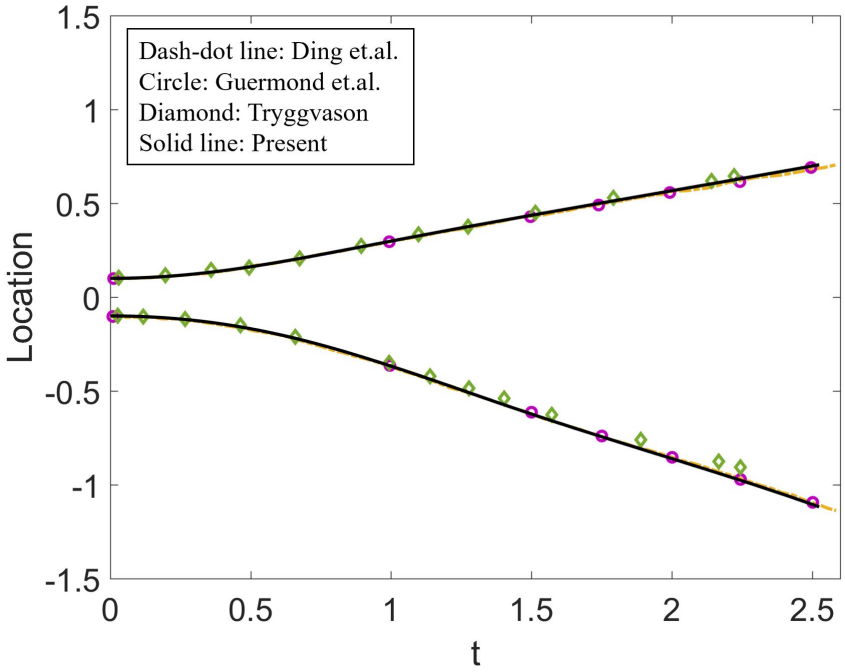

Fig. 16: Locations of the interface of the Rayleigh-Taylor instability with density ratio 3.

tional scale 1m/s^2. The bubble is initially at $(0, 0.5)$ with radius 0.25 and the velocity is zero. The computational domain is $[-0.5, 0.5] \times [0, 1.5]$ and is discretized using 100×150 cells. The no-slip/penetration boundary condition is applied at all the domain boundaries. Different steady contact angles are assigned at the right, left, and top walls. We name the cases by "R#L#T#", where"R","L", and "T" represent the right, left and top wall of the domain and the numbers following them denote the steady contact angles (in degree) at those walls, respectively. We consider 4 cases which are R90L90T90, R30L150T90, R150L120T90 and R30L60T120. The time step size is 2.5×10^{-5}.

The selected snapshots of the 4 cases are shown in Fig. 23-Fig. 26. Little difference is observed in the 4 cases before the bubble touches the top wall. This is reasonable since the contact angle should not interfere with the dynamics far away from the wall. It can be observed that the bubble begins to rise because of the buoyancy effect and deforms by horizontally spreading and vertically shrinking. A large curvature at the left and right of the bubble appears due to the deformation of the bubble. The surface energy is strong due to large curvatures. To prevent further increase in the surface energy, the bubble expands vertically while shrinks horizontally. In addition, a surface wave along the interface is formed. When the bubble touches the top wall, some amount of water is trapped by the bubble and the top wall. Multiple contact lines between the water, air and top wall begin to move from the center to the lateral walls, due to the inertia of the bubble.

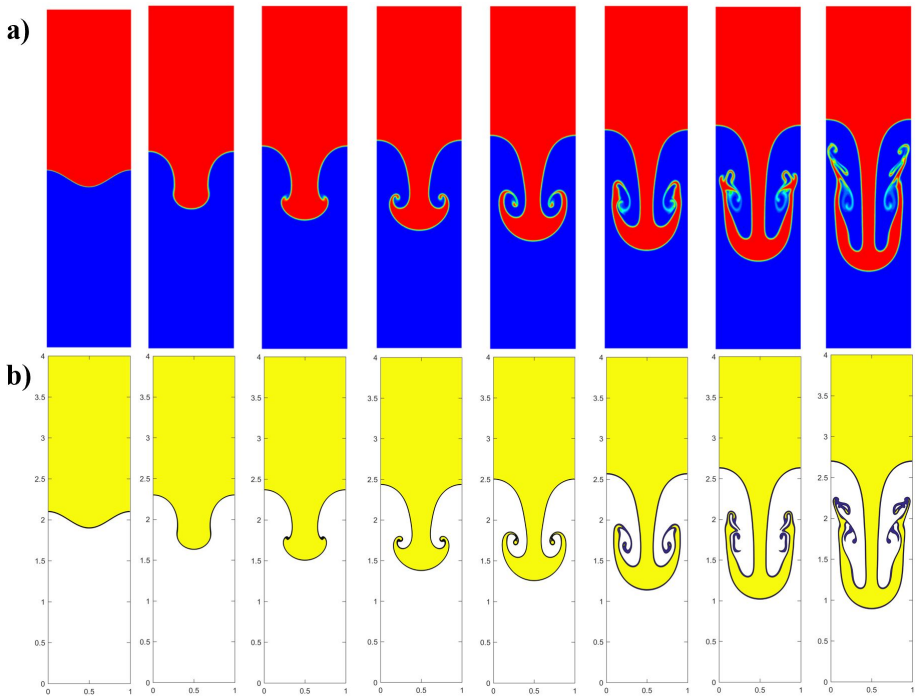

Fig. 17: Snapshots of the interface of the Rayleigh-Taylor instability with density ratio 3. From left to right, $t\sqrt{At} = 0, 1, 1.25, 1.5, 1.75, 2, 2.25, 2.5$. a) is from Ding, et al. [17], and b) is from the present scheme.

R90L90T90, R30L150T90, and R150L120T90 share the same dynamics before the contact lines reach the lateral walls. In R90L90T90 Fig. 23, the bubble touches both of the lateral walls because of the symmetric set up. A new surface wave propagates and reflects between the centerline of the domain and the lateral walls. However, the amplitude is attenuated by the viscous effect and the interface gradually becomes horizontal. Our result of R90L90T90 is comparable to those in [22,28], where only the 90^0 contact angle was considered and the same behavior was reported. Different from R90L90T90, the bubbles in R30L150T90 Fig. 24 and R150L120T90 Fig. 25 only touch the lateral wall that has a smaller steady contact angle. The bubble in R30L150T90 touches the right wall while the one in R150L120T90 touches the left wall. This is reasonable since, with a smaller steady contact angle, the attraction between the wall and the air is stronger. Because of the effect of steady contact angle, the bubbles have different equilibrate shapes and locations.

Again, different dynamics is observed when we change the steady contact angle of the top wall from 90^0 to 120^0, which corresponds to R150L120T90 case in Fig. 25. The bubble is unable to reach either of the lateral walls in this case so the steady contact angles of the lateral walls are not important. After the bubble reaches the top wall, it begins to spread and then shrink along the top wall until its energy is attenuated by the viscous effects.

5 Conclusions and future works

In the present work, the Cahn-Hilliard Phase-Field model for the incompressible two-phase flow is considered. Three consistency conditions, which are the *consistency of reduction*, *consistency of mass and momentum transport* and *consistency of mass conservation*, are proposed. The *consistency of reduction* guarantees that the single-phase dynamics can be physically reproduced by the two-phase model. The *consistency of mass and momentum transport* guarantees the physical coupling between the mass and momentum transport. The *consistency of mass conservation* guarantees that the mass flux follows the mass conservation equation, which is implicitly defined by the Phase-Field equations and the density equation. The Navier-Stokes equations are modified by replacing the mass flux $\mathbf{m} = \rho\mathbf{u}$ in the inertial term $\nabla \cdot (\mathbf{m} \otimes \mathbf{u})$ of the momentum conservation equation by the consistent mass flux in the continuous level $\mathbf{m} = \frac{\rho_1+\rho_2}{2}\mathbf{u} + \frac{\rho_1-\rho_2}{2}(\mathbf{u}\phi - M\nabla\xi)$, which is derived based on the consistency conditions. Our analysis shows that, in the continuous level, only when the consistent mass flux is used the physical momentum and kinetic energy transport can be reproduced and their conservation can be satisfied.

Achieving consistency in the discrete level is more involved and is not guaranteed by just using the consistent mass flux in the continuous level, without carefully considering the numerical details. Our analysis illustrates that the same time discretization schemes for the Phase-Field and the momentum conservation equations should be used, and the numerical schemes to compute the consistent mass flux in the continuous level should be identical to the corresponding ones used in the Phase-Field equation. In addition, the analytical chemical potential ξ in the consistent mass flux should be replaced by the numerical one ξ^* if there is any. Violations of any of the above mentioned requirements introduce the inconsistent error proportional to $\frac{\rho_1-\rho_2}{2}$. Thus, satisfying consistency conditions becomes more significant for large-density-ratio cases, which are very common in two-phase flows. The *consistency of reduction* further requires that the numerical chemical potential $\xi^* \equiv 0$ when $\phi \equiv 1(-1)$ and that the discretized $\nabla\cdot(\nabla\mathbf{u})^T$ to be zero.

The two-phase model, consisting of the Cahn-Hilliard equations and the Navier-Stokes equations, are discretized on the collocated grid, and a consistent, essentially conservative and balanced-force numerical scheme is developed. The consistency in the discrete level is achieved by following our analysis. The Cahn-Hilliard equations are solved with the help of a numerical chemical potential ξ^*, which satisfies the *consistency of reduction* from our analysis. A projection scheme is constructed to decouple the Navier-Stokes equations, whose formal order of accuracy is 2nd order. The Cahn-Hilliard equations, and the inertial term and the viscous term in the Navier-Stokes equations are all in their conservative forms. The corresponding discrete operators are designed to be discretely conservative. Specifically, the convective-type operator is discretized by the WENO scheme[32], while the diffusive-type operator is discretized by the central difference scheme. Consequently, the momentum transport is not only consistent with the mass transport, but also conserved in the discrete level by using the proposed

scheme. We proposed a numerical scheme for the term $\nabla \cdot (\mu(\nabla \mathbf{u})^T)$ such that it discretely reproduce the identity $\nabla \cdot (\nabla \mathbf{u})^T = \nabla(\nabla \cdot \mathbf{u})$, which guarantees both consistency and conservation in the discrete level. However, the pressure gradient and the surface force derived from the Phase-Field model are discretized by a balanced-force algorithm[24], which is non-conservative in general. It should be noted that, away from the interface, the surface force disappears, the density is constant, and the balanced-force algorithm reduces to the 2nd-order central difference for the pressure gradient, which is discretely conservative. We conclude that the Phase-Field function ϕ is conserved in the discrete level, implying the global mass conservation in the discrete level, while the momentum is conserved locally in the discrete level in most of the domain except for the location close to the interface. In addition, the total energy dissipation of the Phase-Field model in the continuous level can be reproduced by the proposed scheme in the discrete level.

Various numerical tests have been performed. The manufactured solution validates the formally 2nd-order accurate of the scheme in both space and time. The large-density-advection case illustrates the significance of achieving consistency in the discrete level. The interface suffers from unphysical deformation, the pressure fluctuates with large amplitude and the error of the velocity is huge, which eventually triggers numerical instability, if the inconsistent scheme is used. These unphysical effects will be magnified if the problem has larger density ratios. On the contrary, the consistent scheme reproduces the physical solution accurately even for extremely large density ratios, e.g., 10^9, while the inconsistent scheme can only handle density ratio 10^3, and its result is totally incorrect. The horizontal shear layer cases are performed to validate the property of the scheme on mass and momentum conservations and energy dissipation in the discrete level. From our results, the mass is globally conserved in the discrete level and this is independent of the appearance of viscosity or surface forces. The momentum is globally conserved in the discrete level in the case with matched density and without a surface force. Our numerical experiments show that the non-conservation is tiny even when there are a surface force and a density contrast. The energy transfer between kinetic energy and free energy is well captured by the scheme and the total energy is dissipated. The steady drop cases are considered to evaluate the performance of implementing the balanced-force algorithm[24] to the surface force derived from the Phase-Field model. Our results show that the strengths of the spurious current are small and insensitive to density ratio, viscosity ratio and surface tension, and it converges at the rate between 1st and 2nd order during grid refinement. Careful and systematic convergence tests are performed based on the rising bubble case including large density ratio (1000), large viscosity ratio (100), surface tension and gravity forces, which has not yet been done in the community of using the Phase-Field model for two-phase flows. We consider the parameters $\eta = \eta_0(h/h_0)^{\chi_\eta}$ and $M = M_0(\eta/\eta_0)^{\chi_M}$, where η controls the interface thickness, M is the mobility and h is the grid size. We observe that our numerical results converge to the sharp interface solution with the rate about 0.6, 0.9, 1.2 and 1.5 when $\chi_\eta = 1/3, 1/2, 2/3$ and 1, receptively. Our tests

also recommend the magnitude of η to be on the order of the grid size h, while it shows that the numerical results are insensitive to the magnitude of M. For verification, the Rayleigh-Taylor instability and dam break are performed and our results match the published numerical results and/or experimental data. We also explore the cases with density ratio 3000 in the Rayleigh-Taylor instability and with density ratio 100,000 in the dam break, which shows the robustness of the present scheme to deal with practical two-phase problems with large density ratio. The long-time dynamics of these two cases is also reported, where complicated interface evolution is observed. The final case considered is the rising bubble with moving contact lines, which includes a large density ratio and the effect of contact angle. Our results show that the set up of contact angle highly influences the dynamics of the bubble after the contact lines are formed. The equilibrium shape and location of the bubble can be very different under different set of contact angles.

Despite the popularity and wide-spread applications of the Cahn-Hilliard Phase-Field model, it should be noted that the intrinsic dynamics of the Cahn-Hilliard Phase-Field model is not exactly the same as the sharp interface one because of the unphysical exaggeration of the interface thickness in practice, and this has been realized, analyzed, and/or discussed in, e.g., [72,37,77] and the references therein. Fortunately, this difference will finally disappear as the interface thickness decreases towards zero, and the Cahn-Hilliard Phase-Field model converges to the sharp interface model. This has been analyzed in [72], shown through asymptotic analysis [1], [42], and quantitatively validated by our numerical practices in Section 4.1 and in the Appendix. However, a smaller interface thickness requires more computational resource so that the interface region is well-resolved. One attractive future direction is to extend the present scheme under an adaptive grid refinement and time stepping so that the problems including a wide range of scales can be accurately and effectively computed. Another interesting future direction is to apply the analysis and scheme in the present work to other Phase-Field models that are plausible for two-phase flow modeling. Some recent studies focus on improving the Cahn-Hilliard Phase-Field model, for example, Li et al.[39] added a profile correction flux into the Cahn-Hilliard Phase-Field model and Zhang and Ye [77] proposed a flux-corrected Phase-Field model, where the tangential diffusive flux is the same as the original Cahn-Hilliard Phase-Field model while the normal one is replaced by the profile correction flux in [39]. It should be noted that, although we focus on the Cahn-Hilliard Phase-Field model in the present work, our analysis doesn't require an explicit definition of the chemical potential ξ. In other words, our analysis works for any Phase-Field model in the conservative form. As a result, our analysis and proposed scheme are ready to incorporate to those improvements on the Cahn-Hilliard Phase-Field model, by simply modifying the definition of the chemical potential ξ and keeping everything the same. Another popular Phase-Field model is the Allen-Cahn Phase-Field model [3], which is non-conservative in its original form. Consequently, the model doesn't conserve mass globally and as a result, it is not suitable for two-phase flow modeling. However, some modifi-

cations has been proposed to fix the conservation issue and the modified models are called conservative Allen-Cahn model. One way to do that is to rewrite the non-conservative form of the Allen-Cahn Phase-Field model to a conservative form, e.g., in [14]. Because of the conservative form, it can be considered loosely as a Cahn-Hilliard model with a different definition of the chemical potential ξ, and our analysis in the present work is again valid in this case. Another way is to add a Lagrange multiplier, e.g., in [33], and a similar idea was applied to the Cahn-Hilliard model in [66]. In this case, although the analysis in the present work can not be directly applied, the three consistency conditions proposed in the present work should again be satisfied when these models are coupled to fluid flows. Among various Phase-Field models, which one performs the best for two-phase flow modeling is still an open question, and the answer to this question is outside the scope of the present work. Some comparisons were performed recently by Lee and Kim [37], Zhang and Ye [77] and Soligo et al. [61]. However, the comparisons in [37], [77] didn't couple the Phase-Field models with fluid flows. In [61], although the Phase-Field models are coupled with a flow solver, the consistency was not considered and the main focus was on matched-density cases. A valuable future work could focus on quantitative comparisons of various Phase-Field models for two-phase flows with significant contrasts of material properties while satisfying the consistency conditions in both continuous and discrete level. We believe these comparisons would be essential to clarify the pros and cons of different Phase-Field models and to shed light on how to appropriately select these models for two-phase flows.

In addition to the Phase-Field model, our analysis of consistency in both continuous and discrete level, and the proposed scheme in the present work can be potentially applied to the problems including different physical phenomena, e.g., the complex fluid [70] and the ferro-hydrodynamic [7], and to the sharp interface model, e.g., the algebraic Volume-of-Fluid method [75].

We conclude that the Phase-Field model considered and the numerical scheme developed are practical and accurate to study two-phase flows, especially for those including large density ratios.

Acknowledgments

A.M. Ardekani would like to acknowledge the financial support from National Science Foundation (CBET-1705371). G. Lin would like to acknowledge the support from National Science Foundation (DMS-1555072, DMS-1821233 and DMS-1736364).

Appendix

Three additional cases, which are the reversed single vortex problem [54], the Zalesak's disk problem [74] and the equilibrium drop [18], are included for completeness.

In the first two cases, the exact values of the velocity field are known. As a result, the Phase-Field equation is decoupled from the flow solver, and thus the consistency conditions, conservation of momentum transport and force balance are not relevant. These two cases evaluate the performance of the Cahn-Hilliard Phase-Field model as an interface capturing method.

The third case is performed to validate the effectiveness of the contact angle boundary condition Eq. (58). An initially semicircular drop moves towards its equilibrium state, having the assigned steady contact angle θ_s at the wall. Since the contact angle modeling is not the major concern in the present work, we again refer interested readers to [31,51,73], for understanding this kind of contact angle boundary condition, to [18,21,6] for more detailed numerical implementations and validations, and to [16,38] for other possible options of imposing the contact angle boundary condition.

Reversed single vortex

Following the case set up in [54], we have a domain of size $[1 \times 1]$ and there is a circle initially at $(x_r, y_r) = (0.5, 0.75)$ with a radius $r = 0.15$. The velocity is defined from the stream function

$$\psi_s = \frac{1}{\pi} \sin^2(\pi x) \sin^2(\pi y) \cos(\frac{\pi t}{T}), \tag{83}$$

where $T = 2$ as that in [54]. The circle stretches by the flow and reaches its maximum deformation at $t = \frac{T}{2}$. The flow begins to reverse after that and the circle should return to its initial location and shape at $t = T$. The cell size of each direction is successively decreased from $h = 1/25$ to $h = 1/200$, and $CFL = |u|_{max} \Delta t / h = 0.1$. η and M are defined identically as those in Section 4.1 with χ_η and χ_M equal to 1. To evaluate the performance of the Phase-Field model, an error is defined such that

$$Er = r - \sqrt{(x_s - x_r)^2 + (y_s - y_r)^2}, \tag{84}$$

where (x_s, y_s) are the points at the zero contour of the Phase-Field function, i.e., $\phi(x_s, y_s) = 0$, obtained by the 'contour' comment in MATLAB. A L_2 error is defined as the root mean square of Er defined in Eq.(84).

Fig. 27 shows the results of the reversed single vortex problem at $t = 0$, $t = \frac{T}{2}$ and $t = T$. It can be clearly observed that the quality of the numerical solution is improved and the solution converges to the exact solution, i.e., the zero contour of the Phase-Field function at $t = T$ is on top of that at $t = 0$, for cases with finer grid size. Table 9 shows the L_2 error of the problem and the convergence rate is around 1.5, which is consistent with those in the convergence tests Section 4.1.

Zalesak's disk

Following the case set up in [74], we have a domain of size $[1 \times 1]$ and there is a notched circle initially at $(x_r, y_r) = (0.5, 0.75)$ with a radius $r = 0.15$. The

Table 9: L_2 error of the reversed single vortex problem

Grid (h)	L_2	Order
1/25	0.013187	1.536231
1/50	0.004547	1.556466
1/100	0.001546	1.728181
1/200	0.000467	

Table 10: L_2 error of the Zalesak's disk problem

Grid (h)	L_2	Order
1/25	0.081624	1.367347
1/50	0.031638	1.872479
1/100	0.00864	2.861625
1/200	0.001189	

width of the notch and the distance from the top of the notch to the center of the circle are both 0.05. The velocity of rigid body rotation is defined from the stream function

$$\psi_s = \frac{1}{2}\Omega_0[(x-x_0)^2 + (y-y_0)^2], \tag{85}$$

where $\Omega_0 = 1$, and $x_0 = y_0 = 0.5$ as those in [54]. The notched circle is going to rotate around (x_0, y_0) without changing its shape. At $t = 2\pi$, the notched circle should return to its initial location without any deformation. The cell size h of each direction is successively decreased from $h = 1/25$ to $h = 1/200$, and $CFL = \Omega_0 \Delta t/h = 0.1$. η and M are defined identically as those in Section 4.1 with χ_η and χ_M equal to 1. To evaluate the performance of the Phase-Field model, an error is defined such that

$$Er = \sqrt{[x_I(s;t=2\pi) - x_I(s;t=0)]^2 + [y_I(s;t=2\pi) - y_I(s;t=0)]^2}, \tag{86}$$

where $x_I(s;t)$ and $y_I(s;t)$ are cubic spline interpolants at time t from points (x_s, y_s) at the zero contour of the Phase-Field function, i.e., $\phi(x_s, y_s) = 0$, obtained by the 'contour' comment in MATLAB, and s is the parameter of the cubic splines ranging from 0 to 1. When evaluating Eq. (86), s is discretized by 1000 points equally. A L_2 error is defined as the root mean square of Er defined in Eq.(86) and evaluated at the discrete points of s.

Fig. 28 shows the results of the Zalesak's disk problem at $t = 0$, $t = 2$, $t = 4$ and $t = 2\pi$. The convergence of the numerical solution to the exact solution can be obviously observed. The shape of the notched circle is maintained better with finer cells, and the zero contour of the Phase-Field function at $t = 2\pi$ is on top of that at $t = 0$, after reducing the cell size. Table 10 shows the L_2 error of the problem and the convergence rate is fast, attributing to the lack of deformation of the notched circle.

Equilibrium drop

Following the case set up in [18], we have a domain $[-3, 3] \times [0, 2]$ and there is a semicircular drop initially at $(x_r, y_r) = (0, 0)$ with a radius $r = 1$. The

velocity components are all zero at the beginning. The left and right boundaries of the domain are periodic, while the top and the bottom are considered as walls. The no-slip and no-penetration boundary condition for velocity is applied at the walls and a 90^0 contact angle is imposed at the top wall. Different steady contact angles θ_s, between the drop and the bottom wall, which are $45^0, 60^0, 90^0, 120^0$ and 135^0, are imposed through the contact angle boundary condition Eq. (58), although initially the contact angle between them is 90^0. The drop will spread or contract along the bottom wall because of the mismatch between the initial 90^0 contact angle and the imposed contact angle, and finally the drop should reach the equilibrium state, where the mismatch disappears.

Since the purpose of this case is to validate Eq. (58), we consider that the two fluids have the same density 1 and viscosity 1. When the drop is at its equilibrium state with a contact angle θ_s, the height of the drop H_d and the spreading length L_d, i.e., the length of the drop touching the bottom wall, have exact solutions [18]

$$H_d = R_d[1 - \cos(\theta_s)], \tag{87}$$

$$L_d = 2R_d \sin(\theta_s), \tag{88}$$

where

$$R_d = r\sqrt{\frac{\pi/2}{\theta_s - \sin(\theta_s)\cos(\theta_s)}}. \tag{89}$$

It should be noted that θ_s in Eqs.(87, 88, 89) is measured by radian. The surface tension between the fluids is 100, η is 0.02, and M is determined from the Peclet number 1.061×10^2 as that defined in [18]. The domain is discretized by 385×128 cells and the time step is $\Delta t = 5 \times 10^{-5}$. The computations are stopped at $t = 1$, which is long enough for the drop to reach its equilibrium state under different contact angels considered. The numerical height and length of the drop is measured based on the zero contour of the Phase-Field function, which is considered as the location of the interface.

Fig. 29 shows the initial and the equilibrium shapes of the drop under different contact angles θ_s. Fig. 30 compares the height and the half spreading length of the drop, obtained from the numerical result, to the exact solution Eqs. (87 and 88), and excellent agreements are achieved.

References

1. Abels, H., Garcke, H., Grun, G.: Thermodynamically consistent, frame indifferent diffuse interface models for incompressible two-phase flows with different densities. Mathematical Models and Methods in Applied Sciences **22**, 1150013 (2012)
2. Aland, S., Voigt, A.: Benchmark computations of diffuse interface models for two-dimensional bubble dynamics. Int. J. Numer. Methods. Fluids **69**, 747–761 (2012)
3. Allen, S., Cahn, J.: A microscopic theory for antiphase boundary motion and its application to antiphase domain coarsening. Acta Metallurgica **27**, 1085–1095 (1979)

4. Anderson, D., McFadden, G., Wheeler, A.: Diffuse-interface methods in fluid mechanics. Annu. Rev. Fluid Mech. **30**, 139–165 (1998)
5. Badalassi, V., Ceniceros, H., Banerjee, S.: Computation of multiphase systems with phase field models. J. Comput. Phys. **190**, 371–397 (2003)
6. Bai, F., He, X., Yang, X., Zhou, R., Wang, C.: Three dimensional phase-field investigation of droplet formation in microfluidic flow focusing devices with experimental validation. Int. J. Multiph. Flow **93**, 130–141 (2017)
7. Bai, F., Li, R., Yang, X., He, X., Wang, C.: A novel energy-based phase-field model for ferrodroplet deformation and breakup in a uniform magnetic field. arXiv:1704.00645 [physics.flu-dyn] (2017)
8. Bell, J., Colella, P.: A second-order projection method for the incompressible navier-stokes equations. J. Comput. Phys. **85**, 257–283 (1989)
9. Brackbill, J., Kothe, D., Zemach, C.: A continuum method for modeling surface tension. J. Comput. Phys. **100**, 335–354 (1992)
10. Bussmann, M., Kothe, D., Sicilian, J.: Modeling high density ratio incompressible interfacial flows. In: Proceedings of ADME Fluid Engineering Division Summer Meeting. p. 31125 (2002)
11. Cahn, J., Hilliard, J.: Free energy of a nonuniform system, i interfacial free energy. J. Chem. Phys. **28**, 258–267 (1958)
12. Chenadec, V., Pitsch, H.: A monotonicity preserving conservative sharp interface flow solver for high density ratio two-phase flows. J. Comput. Phys. **249**, 185–203 (2013)
13. Chiodi, R., Desjardins, O.: A reformulation of the conservative level set reinitialization equation for accurate and robust simulation of complex multiphase flows. J. Comput. Phys. **343**, 186–200 (2017)
14. Chui, P.H., Lin, Y.T.: A conservative phase-field method for solving incompressible two-phase flows. J. Comput. Phys. **230**, 185–204 (2011)
15. Desjardins, O., Blanquart, G., Balarac, G., Pitsch, H.: High order conservative finite difference scheme for variable density low mach number turbulent flows. J. Comput. Phys. **227**, 7125–7159 (2008)
16. Ding, H., Spelt, P.: Wetting condition in diffuse interface simulations of contact line motion. Phys. Rev. E **75**, 046708 (2007)
17. Ding, H., Spelt, P., Shu, C.: Diffuse interface model for incompressible two-phase flows with large density ratios. J. Comput. Phys. **226**, 2078–2095 (2007)
18. Dong, S.: On imposing dynamic contact-angle boundary conditions for wall-bounded liquid-gas flows. Comput. Methods Appl. Mech. Engrg. **247-248**, 179–200 (2012)
19. Dong, S.: An efficient algorithm for incompressible n-phase flows. J. Comput. Phys. **276**, 691–728 (2014)
20. Dong, S.: Physical formulation and numerical algorithm for simulating n immiscible incompressible fluids involving general order parameters. J. Comput. Phys. **836**, 98–128 (2015)
21. Dong, S.: Wall-bounded multiphase flows of nimmiscible incompressible fluids: Consistency and contact-angle boundary condition. J. Comput. Phys. **338**, 21–67 (2017)
22. Dong, S., Shen, J.: A time-stepping scheme involving constant coefficient matrices for phase-field simulations of two-phase incompressible flows with large density ratios. J. Comput. Phys. **231**, 5788–5804 (2012)
23. Fedkiw, R., Aslam, T., Merriman, B., Osher, S.: A non-oscillatory eulerian approach to interfaces in multimaterial flows (the ghost fluid method). J. Comput. Phys. **152**, 457–492 (1999)

24. Francois, M., Cummins, J., Dendy, E., Kothe, D., Sicilian, M., Williams, W.: A balanced-force algorithm for continuous and sharp interfacial surface tension models within a volume tracking framework. J. Comput. Phys. **213**, 141–173 (2006)
25. Guermond, J., Quartapelle, L.: A projection fem for variable density incompressible flows. J. Comput. Phys. **165**, 167–188 (2000)
26. Hirt, C., Nichols, B.: Volume of fluid (vof) method for the dynamics of free boundaries. J. Comput. Phys. **39**, 201–225 (1981)
27. Hohenberg, P., Halperin, B.: Theory of dynamic critical phenomena. Reviews of Modern Physics **49**, 435 – 479 (1977)
28. Huang, Z., Lin, G., Ardekani, A.: A mixed upwind/central weno scheme for incompressible two-phase flows. J. Comput. Phys. **387**, 455–480 (2019)
29. Hysing, S., Turek, S., Kuzmin, D., Parolini, N., Burman, E., Ganesan, S., Tobiska, L.: Quantitative benchmark computations of two-dimensional bubble dynamics. Int. J. Numer. Methods. Fluids **60**, 1259–1288 (2009)
30. Jacqmin, D.: Calculation of two-phase navier-stokes flows using phase-field modeling. J. Comput. Phys. **155**, 96–127 (1999)
31. Jacqmin, D.: Contact-line dynamics of a diffuse fluid interface. J. Fluid Mech. **402**, 57–88 (2000)
32. Jiang, G.S., Shu, C.W.: Efficient implementation of weighted eno schemes. J. Comput. Phys. **126**, 202–228 (1996)
33. Kim, J., Lee, S., Choi, Y.: A conservative allen–cahn equation with a space–time dependent lagrange multiplier. Int. J. Eng. Sci. **84**, 11–17 (2014)
34. Kim, S.: A continuous surface tension force formulation for diffuse-interface models. J. Comput. Phys. **204**, 784–804 (2005)
35. Lalanne, B., Villegas, L., Tanguy, S., Risso, F.: On the computation of viscous terms for incompressible two-phase flows with level set/ghost fluid method. J. Comput. Phys. **301**, 289–307 (2015)
36. Leal, L.: Advanced Transport Phenomena: Fluid Mechanics and Convective Transport Processes. Cambridge University Press (2007)
37. Lee, D., Kim, J.: Comparison study of the conservative allen–cahn and the cahn–hilliard equations. Math. Comput. Simulation **119**, 35–56 (2016)
38. Lee, H., Kim, J.: Accurate contact angle boundary conditions for the cahn–hilliard equations. Comput. Fluids **44**, 178–186 (2011)
39. Li, Y., Choi, J., Kim, J.: A phase-field fluid modeling and computation with interfacial profile correction term. Commun. Nonlinear Sci. Numer. Simulat. **30**, 84–100 (2016)
40. Lilek, Z., Peric, M.: A fourth-order finite volume method with colocated variable arrangement. Comput. Fluids **24**, 239–252 (1995)
41. Liu, C., Shen, J., Yang, X.: Decoupled energy stable schemes for a phase-field model of two-phase incompressible flows with variable density. J Sci Comput **62**, 601–622 (2015)
42. Magaletti, F., Picano, F., Chinappi, M., Marino, L., Casciola, C.: The sharp-interface limit of the cahn-hilliard/navier-stokes model for binary fluids. J. Fluid Mech. **714**, 95–126 (2013)
43. Martin, J., Moyce, W.: An experimental study of the collapse of liquid columns on a rigid horizontal plane. Philosophical Transactions of the Royal Society of London, Series A **244**, 312–324 (1952)
44. Morinishi, Y., Lund, T., Vasilyev, O., Moin, P.: Fully conservative higher order finite difference schemes for incompressible flow. J. Comput. Phys. **143**, 90–124 (1998)

45. Nochetto, R., Salgado, A., Tomas, I.: A diffuse interface model for two-phase ferrofluid flows. Comput. Methods Appl. Mech. Engrg. **309**, 497–531 (2016)
46. Olsson, E., Kreiss, G.: A conservative level set method for two phase flow. J. Comput. Phys. **210**, 225–246 (2005)
47. Olsson, E., Kreiss, G., Zahedi, S.: A conservative level set method for two phase flow ii. J. Comput. Phys. **225**, 785–807 (2007)
48. Osher, S., Sethian, A.: Fronts propagating with curvature-dependent speed: Algorithms based on hamilton-jacobi formulations. J. Comput. Phys. **79**, 12–49 (1988)
49. Owkes, M., Desjardins, O.: A mass and momentum conserving unsplit semi-lagrangian framework for simulating multiphase flows. J. Comput. Phys. **332**, 21–46 (2017)
50. Prosperetti, A., Tryggvason, G.: Computational Methods for Multiphase Flow. Cambridge University Press (2007)
51. Qian, T., Wang, X., Sheng, P.: A variational approach to moving contact line hydrodynamics. J. Fluid Mech. **564**, 333–360 (2006)
52. Raessi, M., Pitsch, H.: Consistent mass and momentum transport for simulating incompressible interfacial flows with large density ratios using the level set method. Comput. Fluids **63**, 70–81 (2012)
53. Rhie, C., Chow, W.: A numerical study of the turbulent flow past an isolated airfoil with trailing edge separation. In: AIAA/ASME 3rd Joint Thermophysics, Fluids, Plasma and Heat Transfer Conference. pp. AIAA–82–0998 (1982)
54. Rider, W., Kothe, D.: Reconstructing volume tracking. J. Comput. Phys. **141**, 112–152 (1998)
55. Rudman, M.: A volume-tracking method for incompressible multifluid flows with large density variations. Int. J. Numer. Methods. Fluids **28**, 357–378 (1998)
56. Rusche, H.: Computational Fluid Dynamics of Dispersed Two-Phase Flows at High Phase Fractions. Ph.D. thesis, Imperial College London, Exhibition Road, London SW7 2BX (2002)
57. Scardovelli, R., Zaleski, S.: Direct numerical simulation of free-surface and interfacial flow. Annu. Rev. Fluid Mech. **31**, 567–603 (1999)
58. Shen, J., Yang, X.: A phase-field model and its numerical approximation for two-phase incompressible flows with different densities and viscosities. SIAM J. SCI. COMPUT. **32**, 1159–1179 (2010)
59. Shen, J., Yang, X.: Decoupled, energy stable schemes for phase-field models of two-phase incompressible flows. SIAM J. NUMER. ANAL **53**, 279–296 (2015)
60. Shen, J., Yang, X., Yu, H.: Efficient energy stable numerical schemes for a phase field moving contact line model. J. Comput. Phys. **284**, 617–630 (2015)
61. Soligo, G., Roccon, A., Soldati, A.: Mass-conservation-improved phase field methods for turbulent multiphase flow simulation. Acta Mech **230**, 683–696 (2019)
62. Sussman, M., Smereka, P., Osher, S.: A level set approach for computing solutions to incompressible two-phase flow. J. Comput. Phys. **114**, 146–159 (1994)
63. Tryggvason, G.: Numerical simulations of the rayleigh-taylor instability. J. Comput. Phys. **75**, 253–282 (1988)
64. Tryggvason, G., Scardovelli, R., Zaleski, S.: Direct Numerical Simulations of Gas-Liquid Multiphase Flows. Cambridge University Press (2011)
65. Unverdi, S., Tryggvason, G.: A front-tracking method for viscous, incompressible, multi-fluid flows. J. Comput. Phys. **100**, 25–37 (1992)
66. Wang, Y., Shu, C., Shao, J., Wu, J., Niu, X.: A mass-conserved diffuse interface method and its application for incompressible multiphase flows with large density ratio. J. Comput. Phys. **290**, 336–351 (2015)

67. Xie, B., Xiao, F.: Toward efficient and accurate interface capturing on arbitrary hybrid unstructured grids: The thinc method with quadratic surface representation and gaussian quadrature. J. Comput. Phys. **349**, 415–440 (2017)
68. Yang, X., Feng, J., Liu, C., Shen, J.: Numerical simulations of jet pinching-off and drop formation using an energetic variational phase-field method. J. Comput. Phys. **218**, 417–428 (2006)
69. Yang, Z., Dong, S.: Multiphase flows of nimmiscible incompressible fluids: Anoutflow/open boundary condition and algorithm. J. Comput. Phys. **366**, 33–70 (2018)
70. Yue, P., Feng, J., Liu, C., Shen, J.: A diffuse-interface method for simulating two-phase flows of complex fluids. J. Fluid Mech. **515**, 293–317 (2004)
71. Yue, P., Zhou, C., Feng, J.: A computational study of the coalescence between a drop and an interface in newtonian and viscoelastic fluids. Physics of Fluids **18**, 102102 (2006)
72. Yue, P., Zhou, C., Feng, J.: Spontaneous shrinkage of drops and mass conservation in phase-field simulations. J. Comput. Phys. **223**, 1–9 (2007)
73. Yue, P., Zhou, C., Feng, J.: Sharp-interface limit of the cahn–hilliard model for moving contact lines. J. Fluid Mech. **645**, 279–294 (2010)
74. Zalesak, S.: Fully multidimensional flux-corrected transport algorithms for fluids. J. Comput. Phys. **31**, 335–362 (1979)
75. Zhang, D., Jiang, C., Liang, D., Chen, Z., Yang, Y., Shi, Y.: A refined volume-of-fluid algorithm for capturing sharp fluid interfaces on arbitrary meshes. J. Comput. Phys. **274**, 709–736 (2014)
76. Zhang, Q., Wang, X.: Phase field modeling and simulation of three-phase flow on solid surfaces. J. Comput. Phys. **319**, 79–107 (2016)
77. Zhang, Y., Ye, W.: A flux-corrected phase-field method for surface diffusion. Commun. Comput. Phys. **22**, 422–440 (2017)
78. Zhou, C., Yue, P., Feng, J.: Dynamic simulation of droplet interaction and self-assembly in a nematic liquid crystal. Langmuir **24**, 3099–3110 (2008)

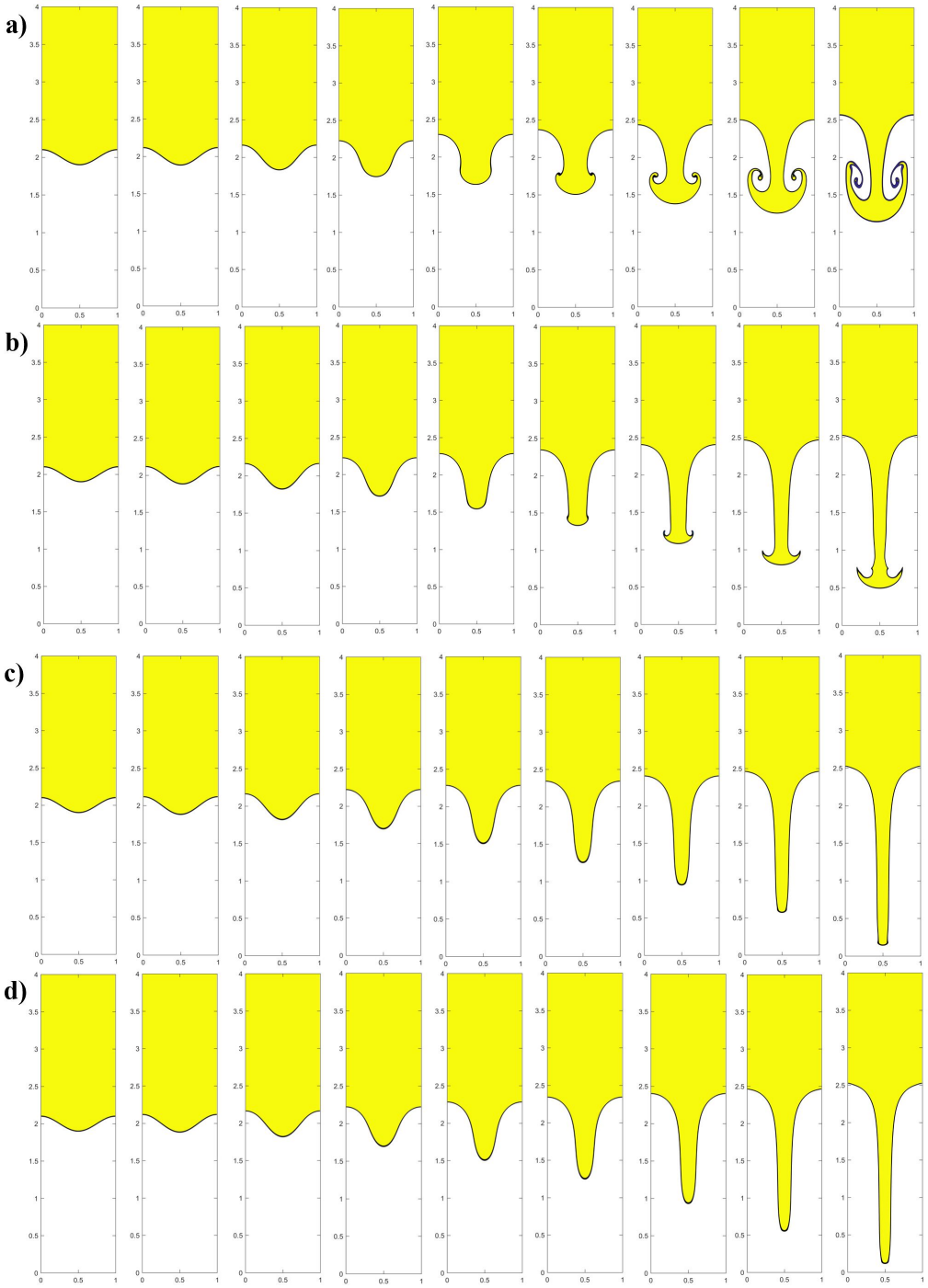

Fig. 18: Snapshots of the interface of the Rayleigh-Taylor instability with density ratio a)3, b)30, c)1000, and d)3000. From left to right, $t\sqrt{At} = 0, 0.25, 0.5, 0.75, 1, 1.25, 1.5, 1.75, 2$.

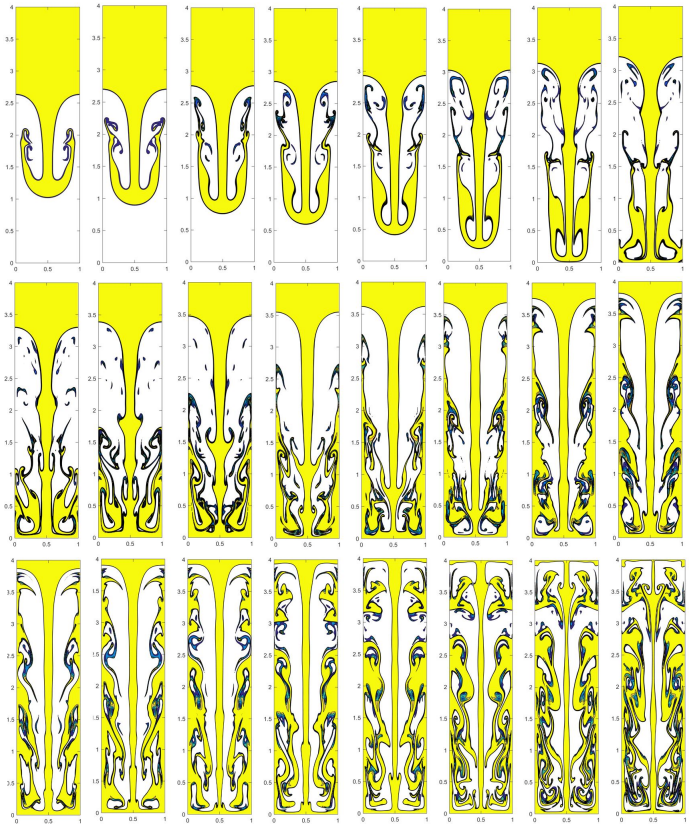

Fig. 19: Snapshots of the interface of the Rayleigh-Taylor instability with density ratio 3. From left to right, top to bottom, $t\sqrt{At}$ is from 2.25 to 8 with 0.25 increment (results of $t\sqrt{At}$ from 0 to 2 are in Fig. 18 a)).

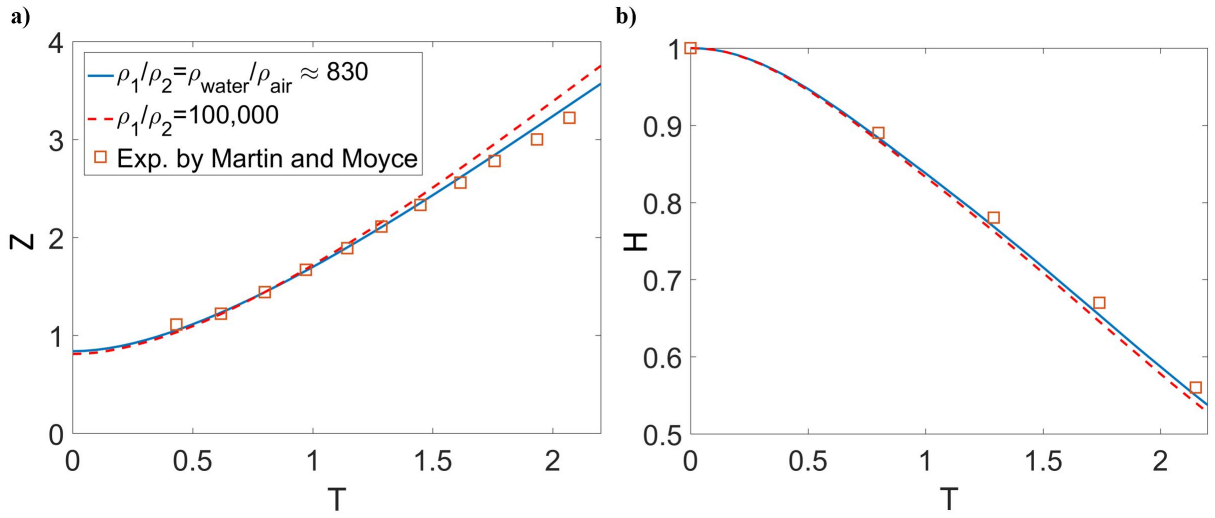

Fig. 20: Results of the dam break. a) Location of the front Z vs. T, and b) location of the height H vs. T.

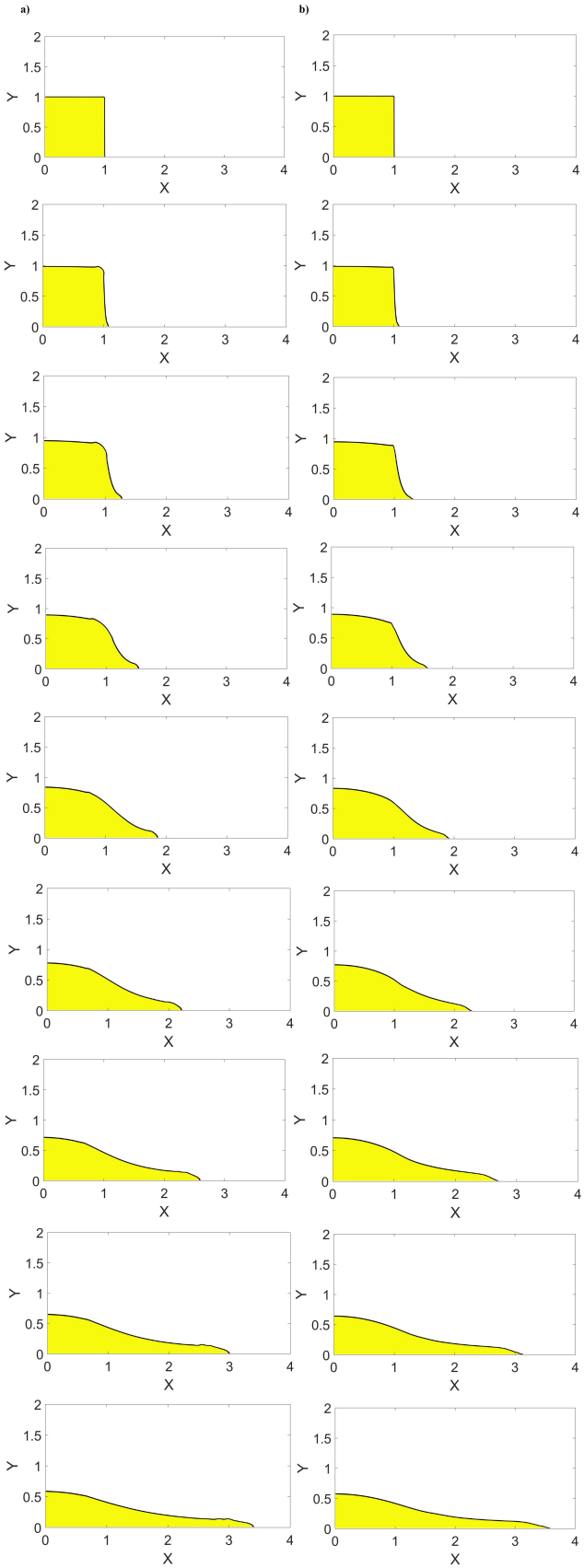

Fig. 21: Snapshots of the dam break with density ratio a) $\rho_1 = \rho_2 = \rho_{water}/\rho_{air} \approx 830$, and b) $\rho_1/\rho_1 = 100,000$. From top to bottom, $T = 0, 0.25, 0.5, 0.75, 1, 1.25, 1.5, 1.75, 2$.

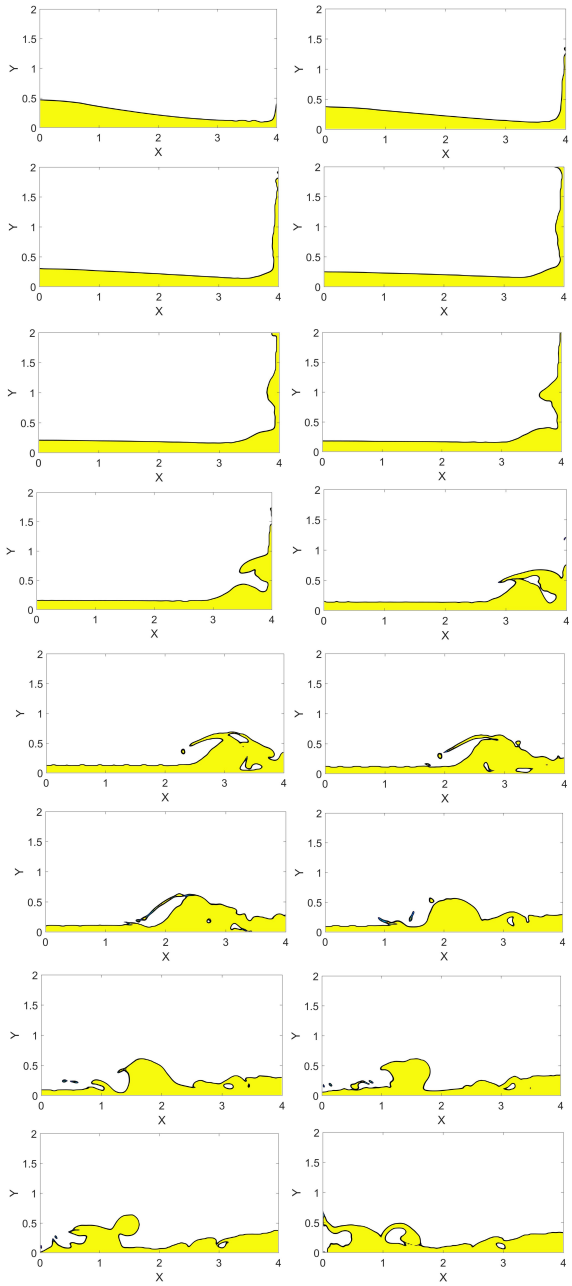

Fig. 22: Snapshots of the dam break with density ratio $\rho_1 = \rho_2 = \rho_{water}/\rho_{air} \approx 830$. From left to right, and top to bottom, T is from 2.5 to 10 with 0.5 increment (results of T from 0 to 2 are in Fig. 21 a)).

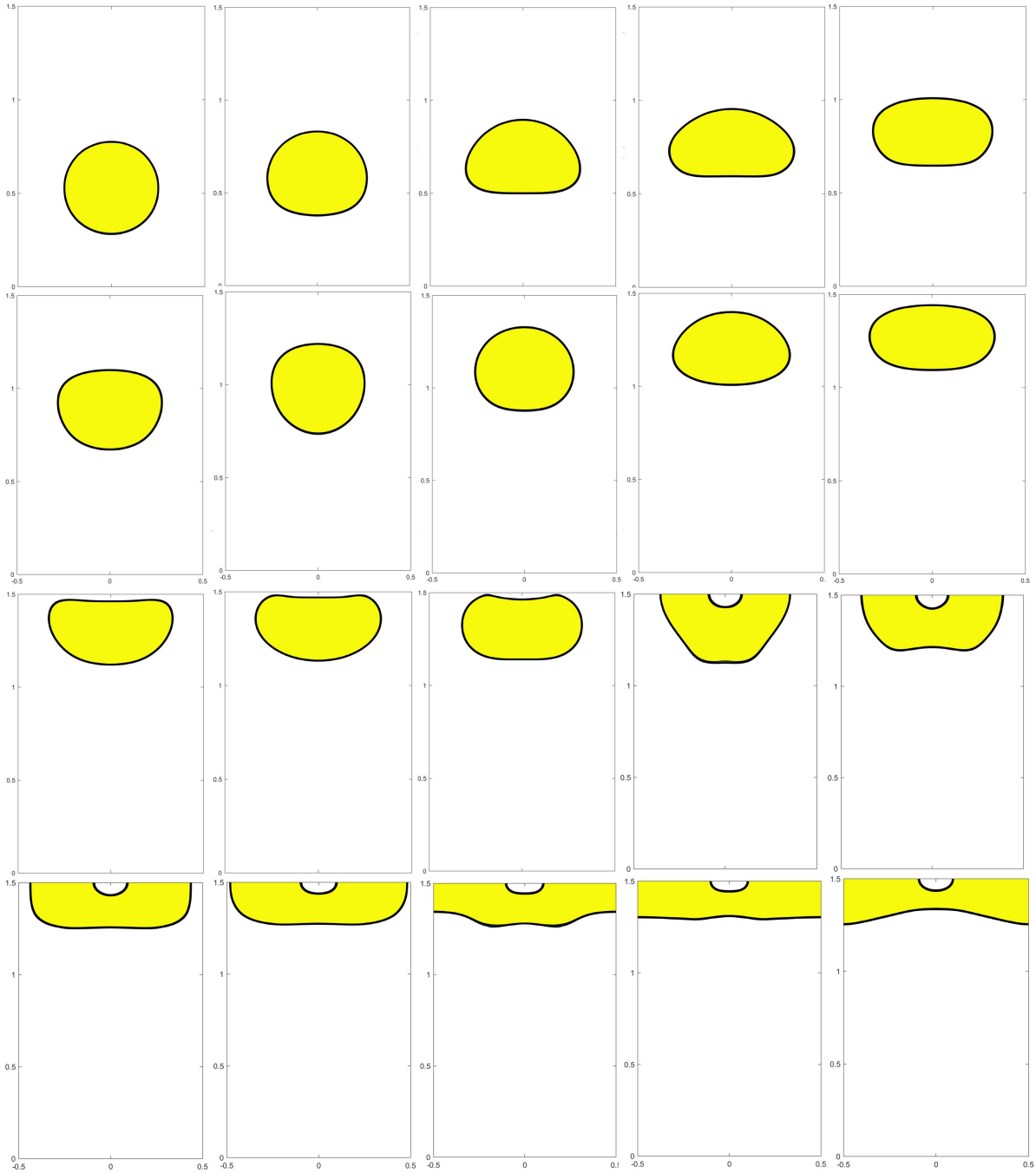

Fig. 23: Snapshots of the rising bubble in R90L90T90. From left to right, top to bottom, t changes from 0.1 to 2 with 0.1 increment.

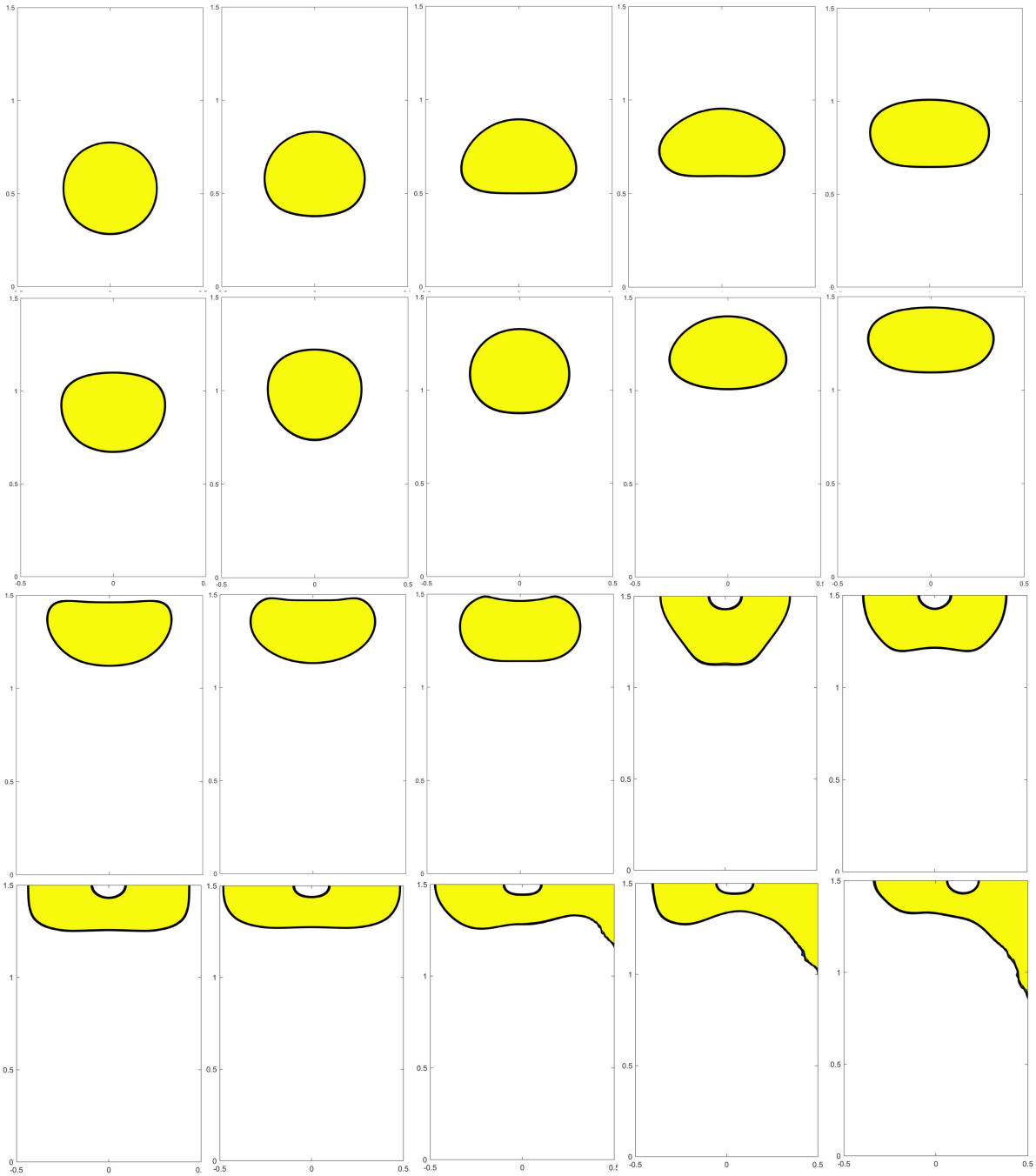

Fig. 24: Snapshots of the rising bubble in R30L150T90. From left to right, top to bottom, t changes from 0.1 to 2 with 0.1 increment.

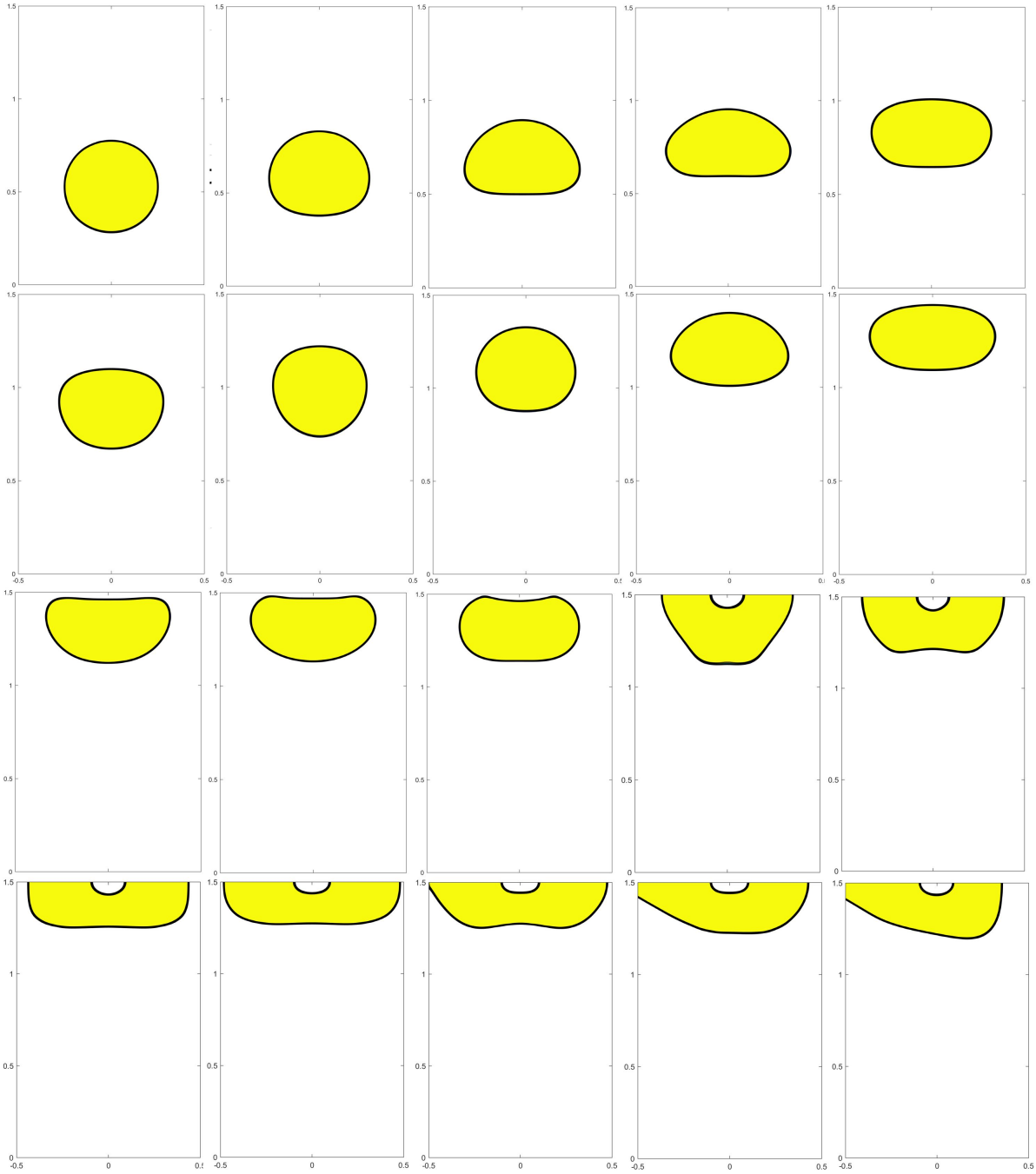

Fig. 25: Snapshots of the rising bubble in R150L120T90. From left to right, top to bottom, t changes from 0.1 to 2 with 0.1 increment.

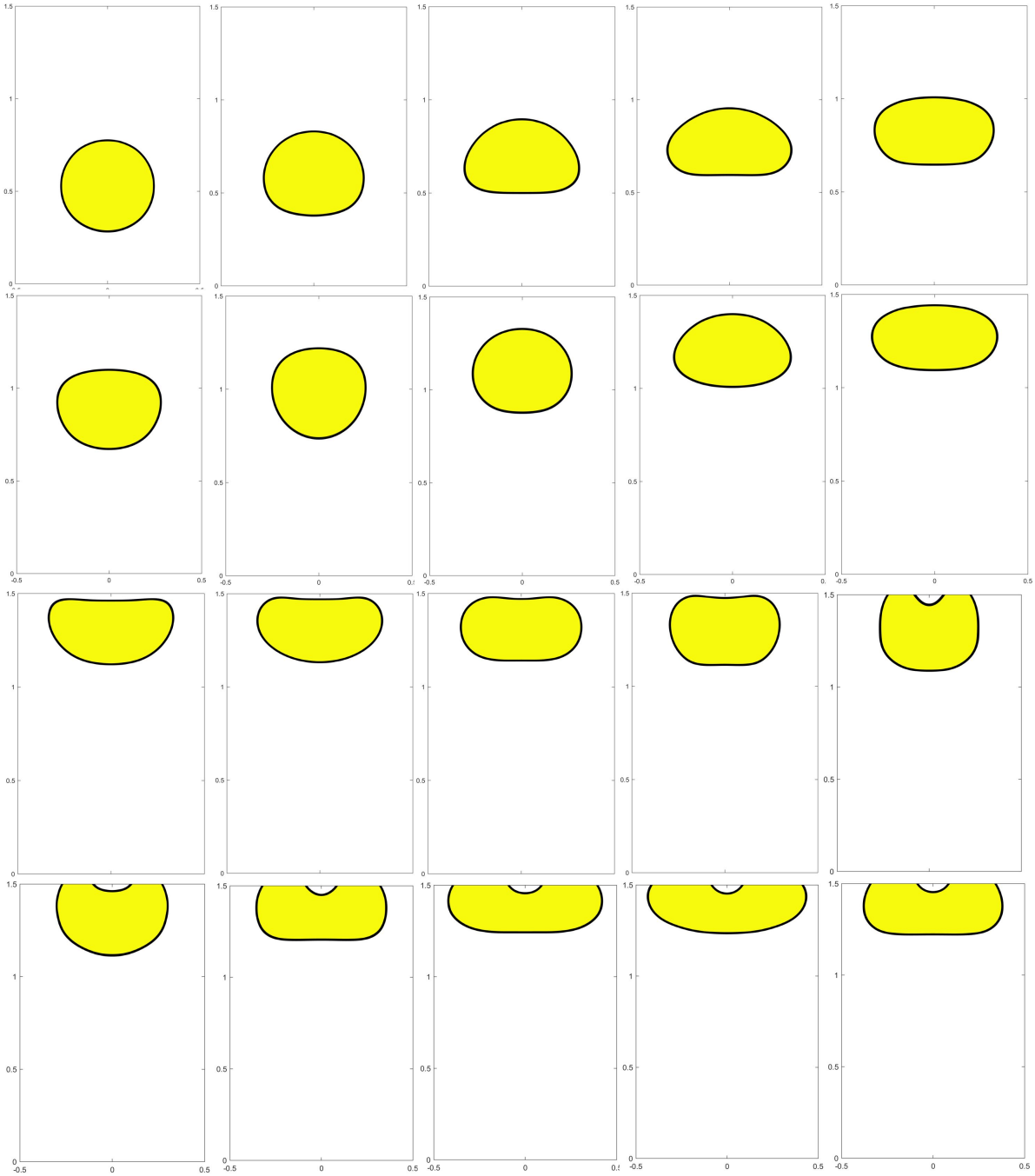

Fig. 26: Snapshots of the rising bubble in R30L60T120. From left to right, top to bottom, t changes from 0.1 to 2 with 0.1 increment.

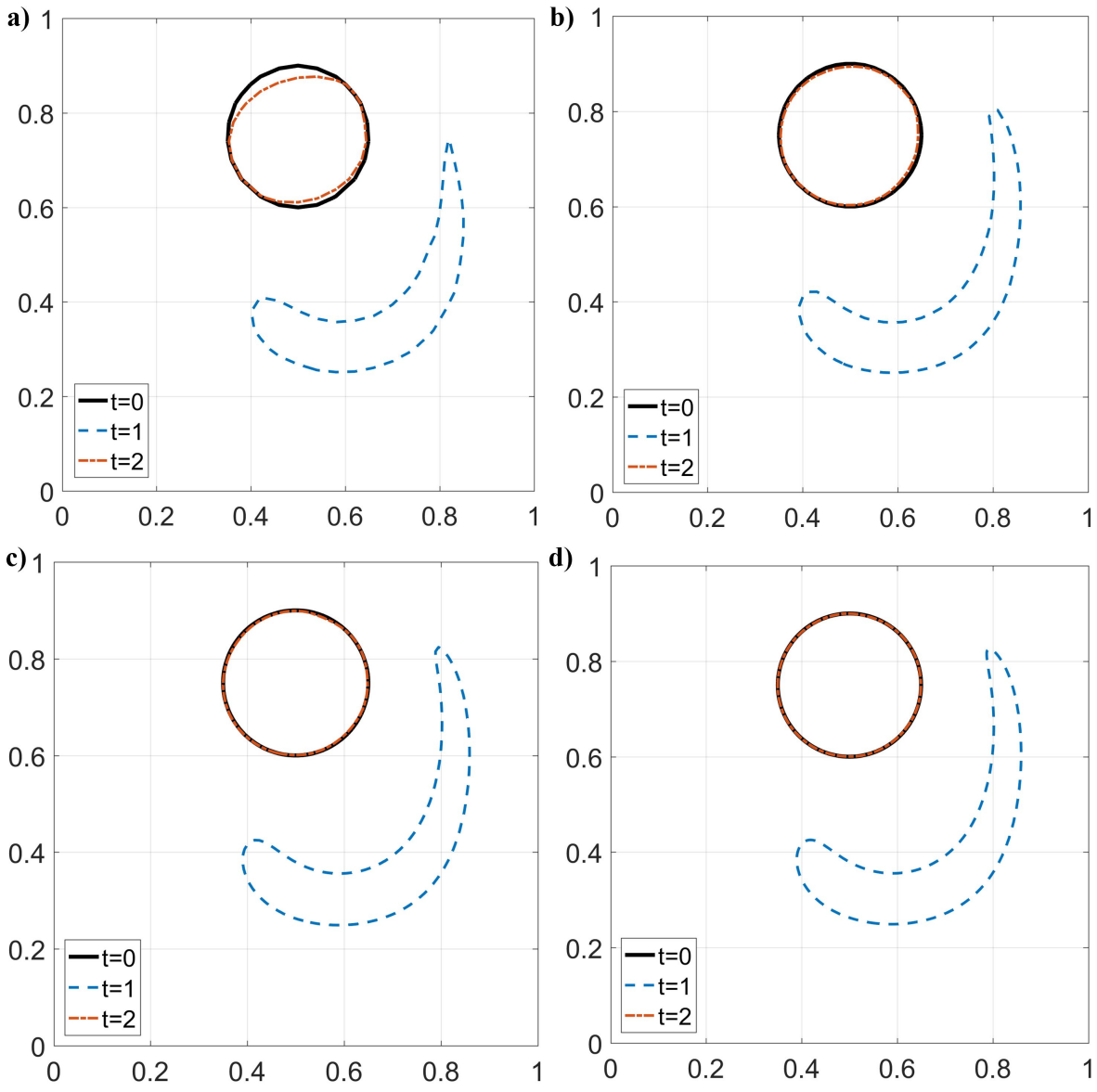

Fig. 27: Results of the reversed single vortex problem. The cell size h of each direction are **a)** 1/25, **b)** 1/50, **c)** 1/100, and **d)** 1/200. Black thick line: at $t = 0$; blue dashed line: at $t = \frac{T}{2}$; dash-dotted line: at $t = T$.

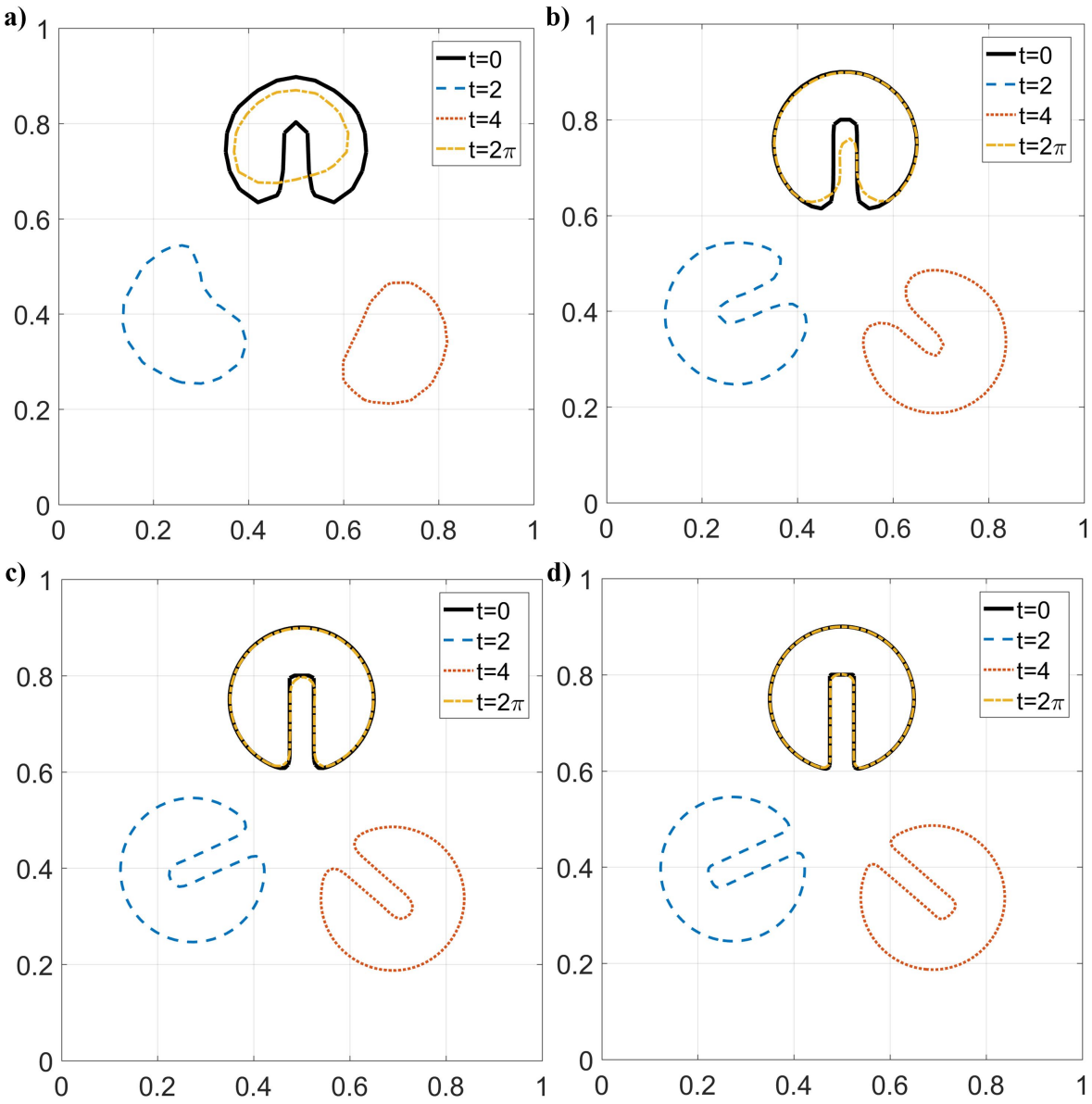

Fig. 28: Results of the Zalesak's disk problem. The cell size$h$ of each direction are **a)** 1/25, **b)** 1/50, **c)** 1/100, and **d)** 1/200. Black thick line: at $t = 0$; blue dashed line: at $t = 2$; red-dotted line: at $t = 4$; yellow dash-dotted line: at $t = 2\pi$.

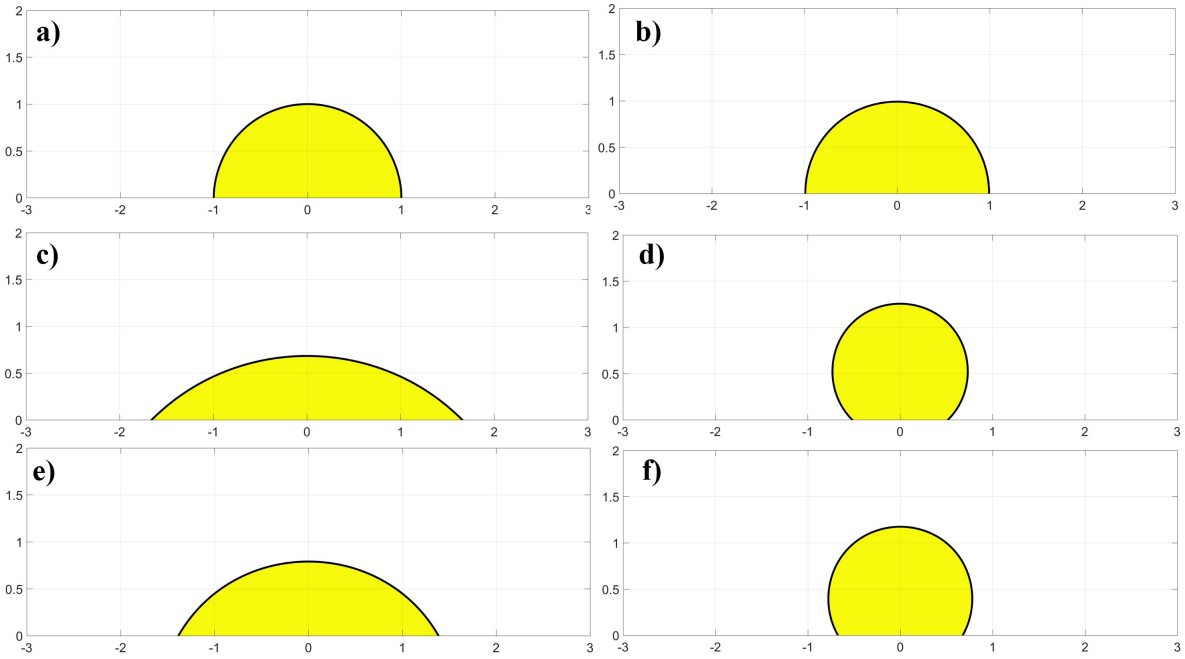

Fig. 29: Results of the equilibrium drop. **a)** Initial shape of the drop, **b)** $\theta_s = 90^0$, **c)** $\theta_s = 45^0$, **d)** $\theta_s = 135^0$, **e)** $\theta_s = 60^0$, and **f)** $\theta_s = 120^0$.

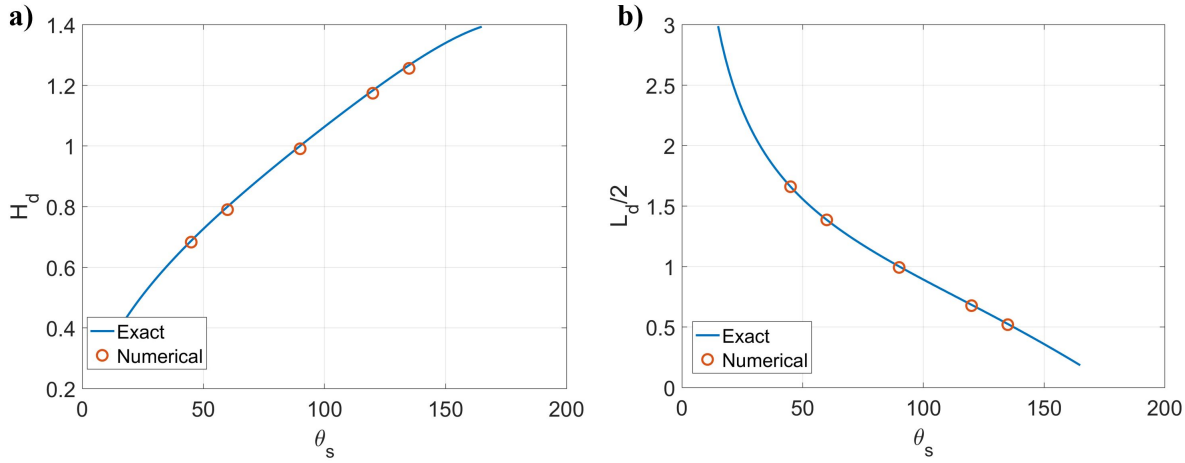

Fig. 30: Results of the height and length of the drop. **a)** Height of the drop, **b)** half length of the drop.